Università degli Studi Milano
Facoltà di Scienze Matematiche Fisiche e Naturali
Corso di laurea in Fisica

Dipartimento di Fisica, Università degli Studi di Milano
Département de physique, Université de Genève
CERN - European Organization for Nuclear Research

# Study of neutrino oscillations with a low energy conventional neutrino superbeam

Relatore : Prof. Francesco Ragusa
Correlatore : Prof. Alain Blondel

Tesi di Laurea di:
Mauro Donegà
Matr. n$^o$ 508510

Anno Accademico 1999/2000

*Dedication*

Measurement of neutrino fluxes produced by cosmic rays interactions and the deficit of solar neutrino compared with the Solar Standard Model suggest a major reconsideration of our understanding of the fundamental neutrino properties, pointing to neutrino oscillations as possible explanation and in any case to neutrinos masses. Many experiments have been performed and many other will investigate this possibility in the coming years. A particular kind of neutrino experiment use a proton accelerator to produce neutrinos, the most ambitious project in this field being the Neutrino Factory. In a Neutrino Factory a MW-scale proton accelerator is used to produce a pion beam. Muons from pion decays, collected with a magnetic horn are accelerated up to 50 GeV and finally stored in an accumulation ring where they decay, sending neutrinos to detectors at different distances.
The present accelerator based experiments generally produce neutrinos from the decay of pions and kaons generated from high energy protons with a power in the 40 kW range. These experiments can be divided into two classes: short baseline experiments where the detector is close to the production point and long baseline experiments where the detector is at hundreds of kilometers away from the production point. An intermediate step between the present accelerator based experiments and the Neutrino Factory, are the so called neutrino superbeams. These superbeams are conventional neutrino beams generated by pion decay but using a very intense MW-scale proton source. A new low energy linear accelerator in the MW-scale, the SPL (Superconducting Proton Linac), has been designed at CERN, and could be used for both superbeam and as first stage for the Neutrino Factory. A working group has been created at CERN to investigate the feasibility and the physics reach of this low energy neutrino superbeam.
The analysis of the potential of the possible SPL-based superbeam is performed in the present study. The experiment would aim at observe the appearance of $\nu_e$ in a initial $\nu_\mu$ beam and improve some of the existing measurements on the oscillation parameters. With the technology of present neutrino detectors, a high level of background rejection is possible, hence in appearance experiments the dominant background is given by the $\nu_e$ contamination of the initial beam. The leading part of the presented study is the optimization of the initial neutrino superbeam purity in the SPL based configuration.
The oscillation parameters and the experiments investigating on them will be considered in the first chapter, reporting the present values of the measured parameters.

Neutrino oscillations formalism is developed in the second chapter; formulas derived there will be used to calculate oscillations probabilities to estimate the number of oscillated neutrinos in the considered superbeam.
The description of the SPL-based neutrino superbeam is analyzed in the third chapter. Starting from a brief description of the accelerator the attention will concentrate on the pion production and focalization with a magnetic horn. The only tool to define the initial composition of the neutrino beam is the pion decay tunnel. The relation between $\nu_e$ contamination and decay tunnel parameters has been investigated.
Neutrino from pion decay and subsequent muon decay have been studied analytically and a FORTRAN program has been implemented to calculate neutrino fluxes. The detailed explanation of the decay analysis is the subject of the fourth chapter. The program used is reported in appendix. The dominant effort in this study is the optimization of the pion decay tunnel and it is performed with a systematic analysis of all the possible configurations.
The sensibility of the experiment using this neutrino superbeam has been investigated. In order to have significant signal, a 40 kton detector at 130 km has been chosen as a reasonable configuration. The detectors studied are a water Cerenkov Super Kamiokande-like and a liquid scintillator MiniBooNE-like. The analysis of the scintillator detector has been performed using the data on detector performance reported in the MiniBooNE proposal, while for the water Cerenkov it has been possible to take advantage of the Super Kamiokande collaboration and use the full detector simulation software. Results of the compared analysis are discussed in the fifth chapter.
The analysis on the oscillation parameters has been focalized on $\theta_{13}$. Likelihood method and exclusion plots as general tools used in neutrino oscillation studies are described in the sixth chapter. Results of the analysis performed with the studied superbeam are reported and compared, in the significant parameters range, with the present limits on $\theta_{13}$ given by CHOOZ. The present study has shown an improvement of almost an order of magnitude in sensitivity with respect to these published data.
This study has been possible thanks to the collaboration between the physics department of "Universtà degli studi di Milano" and the "Université de Genève" in the frame of the Erasmus project. I wish to thank: CERN that allowed me to collaborate with the PS-division; Dave Casper for Super Kamiokande simulations and the important explanations on detector physics; Mauro Mezzetto for the important discussion on MiniBooNE; Simone Gilardoni for MARS simulations of the neutrino factory horn and the

whole Neutrino Factory Oscillations Working Group.

# Contents

# Chapter 1

# Introduction

The first man who had the idea of neutrino existence was W. Pauli in 1930 studying the continuous spectrum of $\beta$ particles emitted by radioactive decay of nuclei. Energy conservation doesn't allow a continuous spectrum for a two body decay. Pauli attempted to solve this problem by imagining a neutral spin 1/2 particle which he called "neutron". He was to present this idea in a conference in Tübingen in December 1930 but, following a genuine "Erasmus-project spirit", he preferred a ball in Zurich and sent a letter to his colleagues at the conference ("Liebe Radioaktive Damen und Herren...") [1]. J. Chadwick would discover what we today call neutron in 1932 [2]. In 1934 E. Fermi took up Pauli's idea and proposed a quantitative theory of $\beta$ decay which could explain the continuous energy spectrum and predict the decay rate [3]. Fermi proposed that the emission of $\beta$ particles (electrons) was due to the decay of Chadwick's neutron to a proton, an electron, and Pauli's invisible particle which he called for the first time with the italian diminutive of "neutrino". The first evidence of neutrino existence was obtained in 1956 by F. Reines and C. Cowan at the nuclear reactor of Savannah River [4]. In 1958 R.P. Feynman and M. Gell Mann proposed a universal theory of the weak "V-A" interaction [5]. The neutrino was established to be left handed in 1958 by M. Goldhaber *et al.* [6]. In 1959 R.Davis and D. Harmer discovered that neutrino is different from anti neutrino [7]. The proposal of a muon neutrino by Pontecorvo in 1959 [8] stimulated the research of L.M. Lederman, M. Schwartz and J. Steinberger which led to the discovery of $\nu_\mu$ in 1962 at Brookhaven [9]. The $\nu_\tau$ was established from decays of the $\tau$ leptons discovered in 1975. In 1989 precise measurements of the $Z^0$ decay width provided evidence that there are only three light neutrinos [10]. Finally in

2000 the last missing neutrino was added at the list with the discovery of the $\tau$ neutrino at Fermilab with the DONUT experiment [11].
In June 1998 a very important event in neutrino physics occurred. The Super Kamiokande collaboration reported a strong evidence for neutrino oscillations in the atmospheric neutrino data [12]. Neutrino oscillations was a reality growing in the last twenty years in solar neutrino experiments. However it was the Super Kamiokande experiment that, for the first time, not only showed with high statistic the deficit of neutrino flux compared with the expectation, but also demostrated that this deficit depends on neutrino pathlenght and energy in the way it is expected to depend in the case of neutrino oscillations. Since neutrino mass is forced to zero in the Standard Model, the evidence for neutrino oscillations (and therefore neutrino mass) is often seen as evidence for physics beyond the Standard Model [13], although it is possible to add masses to neutrinos as Dirac spinors in a straightforward extension of the Standard Model which account for all abserved phenomena.

## 1.1 Solar neutrinos

As all visible stars, the Sun was formed from the gravitational collapse of a cloud of gas contisting mostly of hydrogen and helium. This collapse produced an increase of the core density and temperature resulting in the ignition of nuclear fusion reactions. A state of hydrostatic equilibrium was reached when the kinetic and radiation pressure balanced the gravitational forces preventing any further collapse. There are several nuclear fusion reactions occurring in the sun core. The Solar Standard Model (SSM) which has been developed and continuosly updated by J. Bahcall during the past 20 years [14] predicts the energy spectrum of solar neutrinos. The main assumptions of the SSM are:

- hydrostatic equilibrium;
- energy produced by fusion;
- thermal equilibrium
- energy transport inside the Sun is dominated by radiation

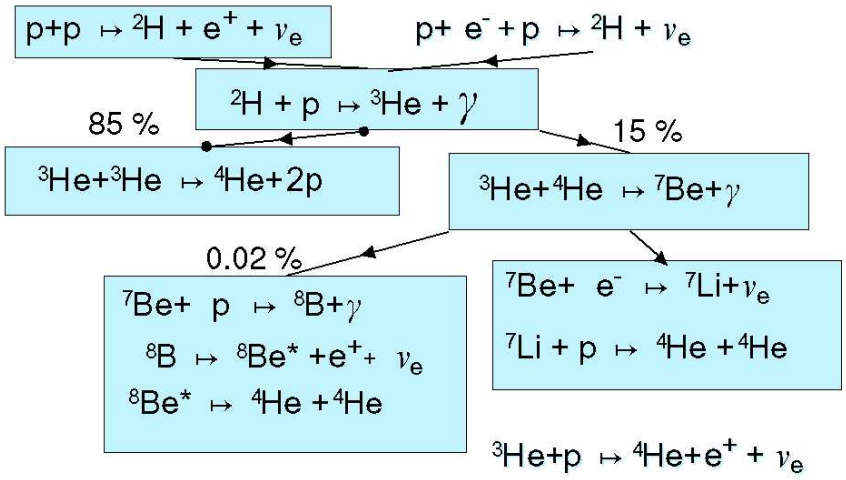


Figure 1.1: pp chain

The SSM calculations are performed by adjusting the initial parameters, by evolving them to the present day and comparing the predicted and measured properties of the Sun. The initial composition of the Sun is taken to be equal to the present day measurement of the surface abudances. If the predicted properties disagree with the measured ones, the calculations are repeated with different inital parameters until agreement is found. These calculations require the knowledge of absolute cross sections for nuclear reactions in a very low energy region where little information is directly available from laboratory experiment. There are two main nuclear reaction chains in the Sun core: the pp chain responsible of the 98.5% of the Sun luminosity and the CNO chain which involves heavier elements. In figure (1.1) the pp chain is shown. In these two chains there are eight reactions that produce neutrinos. Figure (1.2) shows the $\nu_e$ flux as a function of energy as predicted by the SSM for the different reactions. It must be pointed out that while solar neutrinos arrive on the Earth approximately 8 minutes after being produced, it takes $10^6$ years for energy produced in the same reactions to be transported from the sun core to its surface. Thus the luminosity which is measured today is associated with neutrinos which reached the Earth $10^6$ years ago. This, however, is not considered a problem for the SSM because is thought that the Sun has no appreciable change of properties over $10^8$ years.
In the following major experiments on solar neutrinos are briefly described.

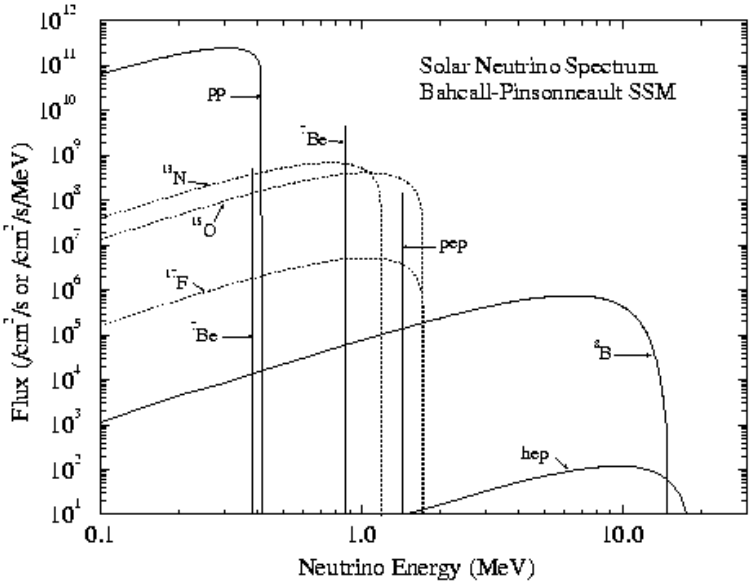


Figure 1.2: Solar neutrino spectrum

### 1.1.1 Homestake experiment

Solar neutrinos were successfully detected for the first time in an experiment performed by R. Davies *et al.* in the Homestake gold mine (U.S.A) [15]. The method consits in measuring the production of $^{37}$Ar from the capture reaction

$$\nu_e + ^{37}Cl \rightarrow e^- + ^{37}Ar$$

which occures in a tank filled with $C_2Cl_4$ (a cleaning fluid). The neutrino energy threshold for this reaction is 0.814 MeV, so this reaction is not sensitive to the $\nu_{pp}$ (see figure (1.2)). The tank is installed deep underground in order to reduce $^{37}$Ar production from cosmic rays. The extraction efficiency is measured by injecting a known amount of $^{37}$Ar in the tank. The $^{37}$Ar production is of the order of 0.5 atoms/day.
It is customary to express the solar neutrino capture rate in solar experiment in SNU (Solar Neutrino Units, 1 SNU corresponds to 1 capture/s from $10^{36}$ nuclei). The results of the homestake experiment averaged over more than 20 years of data taking is [16] $2.56 \pm 0.16 \pm 0.16$ SNU (the first error is statistical and the second one systematic) where the SSM predictions as calculated by

Bahcall *et al.* is [14] $7.7^{+1.2}_{-1.0} \pm 3.0$ SNU. Hence the total measured number disagrees with the predicted value.

### 1.1.2 Gallium experiment

Two experiments, GALLEX [17] installed in the LNGS (Laboratori Nazionali del Gran Sasso, Italy) and SAGE [18] installed in the Baksan underground laboratory (Russia) have measured the rate of the reaction

$$\nu_e + {}^{71}Ga \rightarrow {}^{71}Ge + e^-$$

This reaction has a neutrino threshold of 0.233 MeV and is sensitive to the $\nu_{pp}$ contribution (see figure (1.2)). Both experiments have measured the neutrino detection efficiecy, with the use of intense source of $^{51}$Cr. In the GALLEX experiment the $^{71}$Ge extraction efficiency has been measured directly by injection in the tank of known quantities of $^{71}$As that decays to $^{71}$Ge.
The solar neutrino flux measured by the GALLEX experiment is [19] $77.5 \pm 6.2^{+4.3}_{-4.7}$ SNU; the measurement of SAGE experiment is [20] $66.6^{+6.8+3.8}_{-7.1-4.0}$ SNU. The SSM predictions are [14] $123 \pm 5$ SNU. Again the measured number is much lower than the SSM prediction.

### 1.1.3 Super Kamiokande

Super Kamiokande is a real-time experiment which uses an underground detector installed in the Kamioka mine 350 km from Tokio [21]. The detector consist in a tank filled with 22000 ton of water and approximately 40% of the surface is covered with photomultipliers. The detector is used as an imaging Cerenkov counter. (This detector will be described in more detail in the fifth chapter). Solar neutrinos are detected by the scattering reaction

$$\nu + e^- \rightarrow \nu + e^-$$

The detection threshold is 5 MeV, hence sensitive only to $\nu$ from B or "hep", (see figure (1.2)). The detected electron from the previous scattering reaction has a very strong directional correlation with the incident neutrino. This property is used to demostrate the solar origin of the events. The Super Kamiokande experiment began data taking in 1996 and has published the following flux [14] $2.40 \pm 0.03 \pm 0.08\, 10^6\, cm^{-2} s^{-1}$. This value is the 47% of the SSM prediction [14] $5.15^{+0.98}_{-0.72}\, 10^6\, cm^{-2} s^{-1}$. Again the measured number is much lower than the SSM prediction.

### 1.1.4 Interpretation of the phenomenon

The global analysis of the solar neutrino data shows an apparent absence of $\nu_e$ from the Be line. This is a real puzzle because $\nu_e$ from $^8$B are observed by Super Kamiokande and, as it is possible to see in figure (1.1), $^8$B is formed from the fusion reaction

$$p +^7 Be \rightarrow \gamma +^8 B$$

which implies that $^7$Be must exist in the Sun. This in turn implies the occurence of the reaction

$$e^- +^7 Be \rightarrow^7 Li + \nu_e$$

which is responsible for $\nu_e$ from $^7$Be production. There are at least two possible explanations to this puzzle:

- The SSM in not correct, resulting in unreliable predictions of solar neutrino flux (however, the SSM correctly predicts the results of helioseismlogical observations [22] which depend on the temperature profile of the Sun)
- The $\nu_e$ produced in the core of the Sun are no longer $\nu_e$ when they reach the earth.

The second explanation, which is thought to be the correct one, implies neutrino masses and most probably neutrino oscillations. (For an introduction the the formal theory of the neutrino oscillation physics, see the next chapter.)
In the frame of the oscillations explanation there are two classes of solutions to this puzzle: vacuum oscillations solutions and matter enhanced solutions. The experimental results on solar neutrinos can be explained by vacuum oscillation parameters that strongly suppress $\nu_e$ from the Be line when these neutrinos reach the Earth at a distance $L = 1.5\,10^{11}$ m from the Sun. Solutions derived by the Super Kamiokande collaboration [14], are shown in figure (1.3). The $\Delta m^2$ value are in the range of $4\,10^{-11}$ - $5\,10^{-10}\,eV^2$ and the mixing angle is large ($\sin^2(2\theta) > 0.6$).

The other class of oscillations solution to the solar problem can be found in the framework of the theory of neutrino oscillations in matter. It was first pointed out by L. Wolfenstein [23] that neutrino oscillations in dense matter differ from oscillations in vacuum if $\nu_e$ are involved. In fact $\nu_e$ can

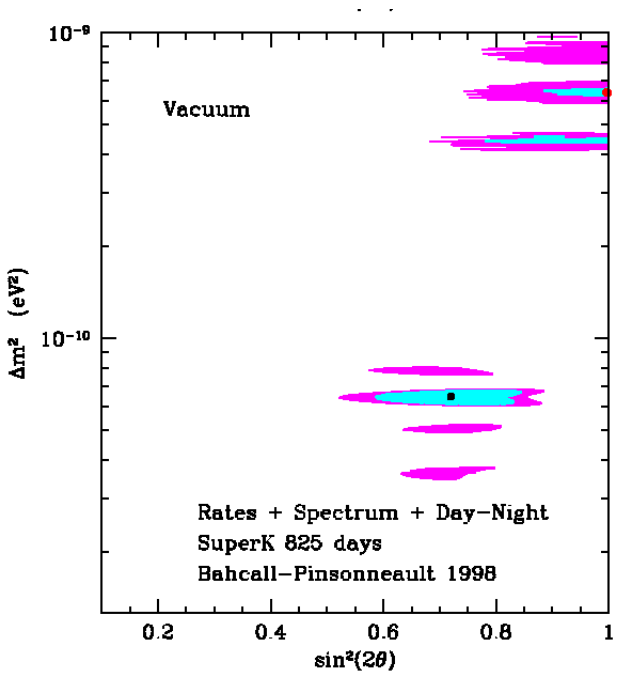


Figure 1.3: The Super Kamiokande two flavours fit for vacuum oscillation.[14]

interact in matter through the exchange of a W boson directly with an electron. This supplemental contribution makes the oscillation length and the neutrino mass eigenvalue depending on the density of the material which they are traversing. For neutrino propagating through the Sun, the density $\rho$ varies along the trajectory from a value higher than 100 $g/cm^3$ in the core to much less than 1 $g/cm^3$ in the outermost layers. Oscillation solutions in matter are the so called Mikheyev-Smirnov-Wolfenstein (MSK) solutions [24]. The results of the latest analysis of the solar neutrino event rates in terms of matter enhanced oscillations are shown in figure (1.4). There are three possible solutions: two with large mixing angles (LMA) and $\Delta m^2 \simeq 10^{-7}\, eV^2$ or $4\,10^{-5}\, eV^2$ and one with small mixing angle (SMA) $\sin^2(2\theta) \simeq 0.005$ and $\Delta m^2 \simeq 6\,10^{-6}\, eV^2$.
New experiments such as Borexino, SNO and KAMLAND, should add new information to help to solve the neutrino oscillation puzzle.

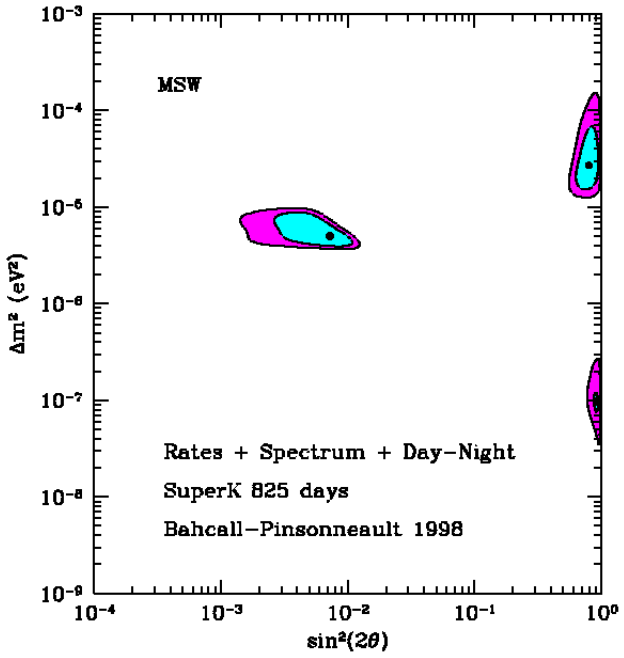


Figure 1.4: The Super Kamiokande two flavours fit to MSW conversion to an active neutrino.[14]

### 1.1.5 Borexino

Borexino is an experiment presently under construction at the LNGS (Laboratori Nazional del Gran Sasso, Italy) [25]. The detector consists of a spherical acrylic vessel of 8.5 m diameter filled with very high purity, low activity liquid scintillator and viewed by an array of 1650 photomultipliers located on its surface. The relative timing of the photomultipliers signals provides information on the event position within the detector volume. The entire detector is immersed in a cylindrical tank 16.5 m high with 16.5 m diameter filled with high purity water acting as a shield. The aim of the experiment is to detect $\nu - e^-$ elastic scattering with threshold as low as 0.25 MeV. The experiment would be sensitive to the $\nu_e$ from the Be line component of the solar flux which is expected to be strongly suppressed if neutrino oscillations are indeed the solution of the solar neutrino puzzle.

### 1.1.6 SNO

The Sudbury Neutrino Observatory (SNO) is a solar neutrino detector installed in the Creighton mine (Ontario, U.S.A.) [26]. SNO is presently in data taking. The detector consists of a spherical acrylic vessel containing 1000 ton of high purity heavy water ($D_2O$) surrounded by 7800 tons of ultrapure water for shielding purposes. Cerenkov light produced in heavy water is collected by 9546 photomultipliers. As for Super Kamiokande experiment neutrino are detected by the elastic scattering reaction $\nu + e^- \rightarrow \nu + e^-$ which have a threshold of 5 MeV. However in heavy water the charged current reaction $\nu_e + d \rightarrow p + p + e^-$ also occur with a threshold of 6.5 MeV. However the main feature of SNO is its capability to detect the reaction

$$\nu + d \rightarrow p + n + \nu$$

which has the same cross-section for all the three neutrino flavours and measures the total solar neutrino flux. Any significant difference from charged current reactions would provide, therefore, unambiguous proof of neutrino oscillations.

### 1.1.7 KAMLAND

The Kamioka Liquid scintillator Anti Neutrino Detector (KAMLAND) [27], is not a solar neutrino experiment. It is discussed here because it is sensitive

to oscillation parameters which could explain the solar neutrino problem. The detector is a trasparent sphere with a diameter of 13 m filled with scintillating isoparaffin oil. This sphere is itself contained in a larger, concentric sphere (18 m diameter) filled with isoparaffin oil. Scintillation light from the inner sphere is collected by 1300 photomultipliers located on the surface of the outer sphere. The entire system is immersed in high purity water and installed in the Kamioka mine at a depth of 2700 of water equivalent. KAMLAND aims at detecting the $\bar{\nu}_e$ produced by five nuclear reactors located at distances between 150 and 210 km from the detector and producing a total thermal power of 127 GW. Because of the large distance from the reactors and of the low $\bar{\nu}_e$ energy KAMLAND is sensitive to $\Delta m^2 > 7\,10^{-6} eV^2$ and $\sin^2(2\theta) > 0.1$ a region which includes the large mixing angle solutions.

## 1.2 Atmospheric neutrinos

Since the total thickness of the atmosphere is $\simeq 10^3\, g/cm^2$ the interaction of primary cosmic rays in the upper layers of the atmosphere results in the development of hadronic showers leading to a flux of neutrinos from charged pions and muon decay. These neutrinos have energies ranging from $\simeq 0.1$ GeV to several GeV. Their interaction rate is of the order of 100/y for a target mass of 1kton.
Since $\nu_\mu$ is produced from both $\pi^\pm$ and $\mu^\pm$ decay and a $\nu_e$ form $\mu^\pm$ decay only, one expects the ratio between the $\nu_\mu$ and $\nu_e$ fluxes on the earth to be of the order of two if both $\pi^\pm$ and $\mu^\pm$ decay in the atmosphere. This indeed is a very good approximation for neutrinos with energies lower than 3 GeV. At higer energy the fraction of $\mu^\pm$ decaying in the atmosphere and producing $\nu_e$ or $\bar{\nu}_e$ decreases.
Calculations of atmospheric neutrino fluxes are affected by sizeable uncertainties which result from uncertainties on the composition and energy spectrum of the primary cosmic rays and on secondary particle distribution. In addition, these calculations ignore for semplicity the lateral shower development and treat the problem in one dimension only. The final uncertainties affecting the $\nu_\mu\, \nu_e$ fluxes on Earth is estimated to be of the order of $\pm 30\%$. However, because of partial cancellations, the uncertainties on the predicted $\nu_\mu/\nu_e$ ratio is believed to be of the order of $\pm 5\%$.

| Experiment | R |
|---|---|
| Kamiokande | $0.60 \pm 0.06 \pm 0.05$ |
| Super Kamiokande | $0.65 \pm 0.02 \pm 0.05$ |
| IMB | $0.54 \pm 0.05 \pm 0.07$ |
| FREJUS | $0.99 \pm 0.13 \pm 0.08$ |
| NUSEX | $1.00 \pm 0.3$ |
| Soudan-2 | $0.68 \pm 0.11 \pm 0.06$ |

Table 1.1: Results on R. The first errors is statistical, the second is systematic.

### 1.2.1 Atmospheric neutrino experiments

Six underground experiments have measured the atmospheric neutrino fluxes by detecting quasi-elestic interactions:

$$\nu_\mu(\nu_e) + n \rightarrow \mu^-(e^-) + p$$

$$\bar{\nu}_\mu(\bar{\nu}_e) + p \rightarrow \mu^+(e^+) + n$$

Three experiments (Kamiokande [28], IMB-3 [29], Super Kamiokande [21]) detect Cerenkov light rings. The other three experiments, FREJUS [30], NUSEX [31], Soudan-2 [32] use calorimeters with high longitudinal and transverse segmentation. The comparison between the measured and the predicted $\nu_\mu/\nu_e$ ratio for the six experiment is shown in table (1.1) which list the value of the double ratio R defined as:

$$R = \frac{(\nu_\mu/\nu_e)measured}{(\nu_\mu/\nu_e)predicted}$$

With the exception of the values measured by FREJUS and NUSEX, all values of R are significantly lower than the expectation (R=1). The NUSEX result is affected by a large statistical error, while the FREJUS result is not confirmed by Soudan-2 which use the same detection technique. It can be concluded, therefore, that a small R value (of the order of 0.6) is now firmly established.

The flightpath of atmospheric neutrino from the production point to the detector, L, varies enormously with the zenith angle $\theta_Z$. For example, neutrinos impinging on the detector from above ($\cos\theta_Z = 1$) are produced $\simeq$

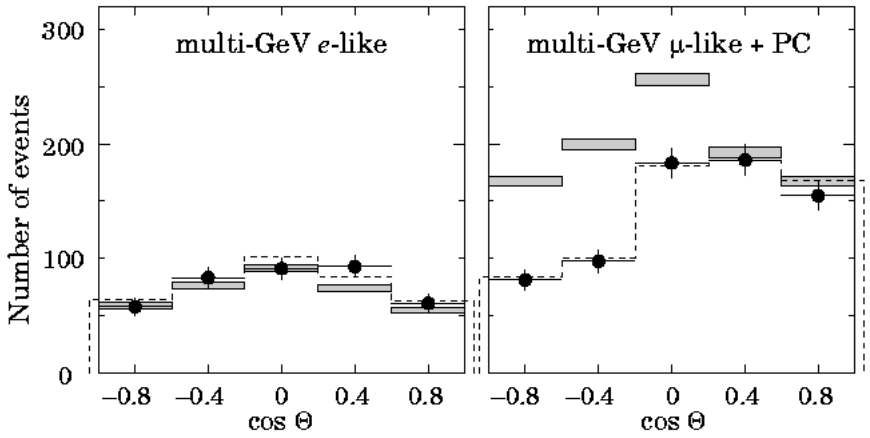


Figure 1.5: Zenith angle dependence of multi-GeV neutrino interactions from Super Kamiokande, [33]. The expectations for no oscillations is shown in the hatched region.

10 km above the detector while upward going neutrinos ($\cos\theta_Z = -1$) have traversed the Earth and so have travelled for $\simeq$ 13000 km before reaching the detector. Also the higher the neutrino energy, the better the outgoing charged lepton follows the incident neutrino direction. Hence the charged lepton zenith angle is a direct measurement of L. Because of the directionality of Cerenkov light, the water detector can be seen as disappearence experiment with variable neutrino energies and pathlength. Measurement of the zenith angle distributions are a sensitive way to search for neutrino oscillations. The Kamiokande experiment [33] published a dependece of R on $\theta_Z$ which disagrees from the expected shape. The Super Kamiokande $\theta_Z$ distributions [34] with a much larger event sample are shown in figure (1.5). It is clear that there are less muon events in the upward direction than the expected, while the number of downward going muon events is consistent with the expectation. For electrons, however, the distribution agree with the expectations. Figure (1.6) shows the up-down asymmetry defined as (U-D)/(U+D) where U (D) is the total number of events with $\cos\theta_Z < -0.2$ ($\cos\theta_Z > 0.2$), as a function of the charged lepton momentum [35]. While for electron events the asymmetry is consistent with zero, for muon events its absolute value increases with momentum and reaches a value around -0.4 above 1 GeV.

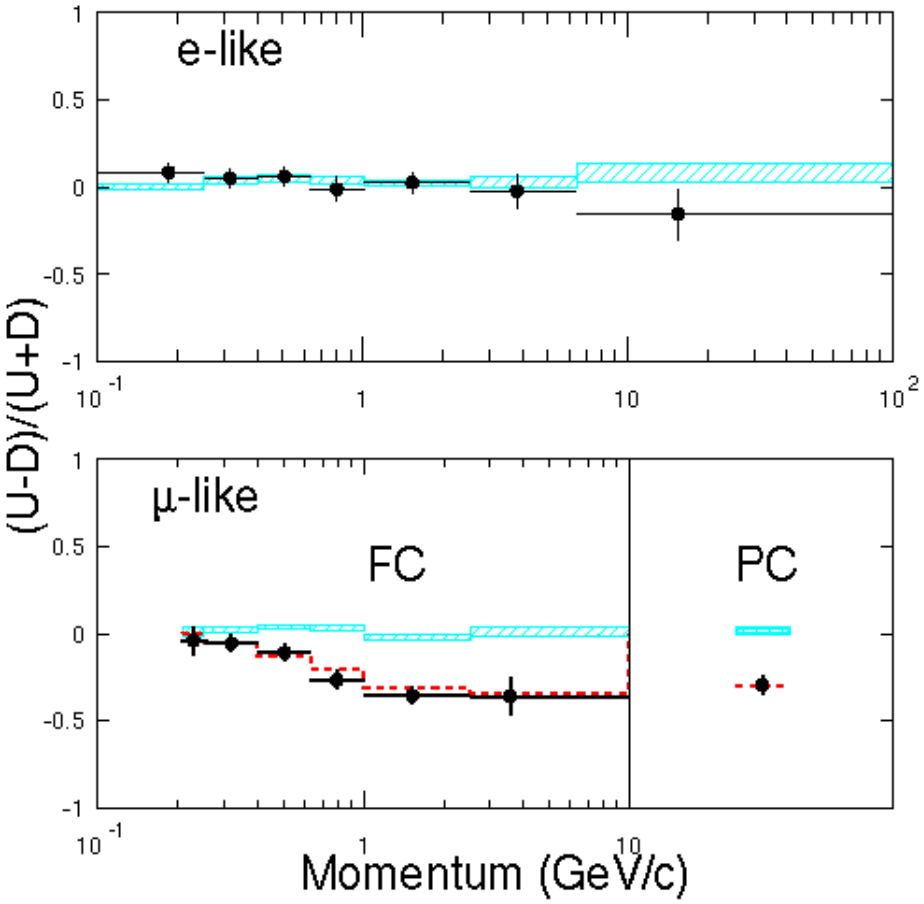


Figure 1.6: The (U-D)/(U+D) zenith angle asymmetry is plotted versus momentum for $e$-like and $\mu$-like events. The expectations for no oscillations is shown in the hatched region. The solid line shows the expectation for $\nu_\mu \rightarrow \nu_e$ oscillations [35].

### 1.2.2 Interpretation of the phenomenon

Figures (1.5), (1.6) clearly demonstrates the existence of a new phenomenon. Its most plausible interpretation is the occurrence of $\nu_\mu$ oscillations. Since the $\nu_\mu/\nu_e$ ratio at the production is equal to 2 or larger, $\nu_\mu \to \nu_e$ oscillations would induce a large up-down asymmetry for electrons as well, with more up-going than down-going electrons, in disagreement with the data. Hence the $\nu_\mu$ predominantly oscillates to $\nu_\tau$ or to a new type of "sterile" neutrino, which is a neutrino that doesn't interact in charged or neutral current. In figure (1.7) the oscillations parameters required to describe Super Kamiokande atmospheric neutrino results are shown.

Another phenomenon that confirm the hypothesis of $\nu_\mu \to \nu_\tau$ oscillations come from upward going muons. Charged current interactions of upward-going $\nu_\mu$'s in the rock produce upward-going muons which can either stop or traverse the detector. The study of the zenith angle distribution in the interval $-1 < \cos\theta_Z < 0$ has provided an additional evidence for $\nu_\mu \to \nu_x$ oscillations.

Upward-going $\mu$ have been studied by Super Kamiokande where good agreement is obtained under the assumption of $\nu_\mu \to \nu_\tau$ oscillations.

Another experiment that studied upward-going $\mu$ is the MACRO experiment at LNGS (Laboratori Nazionali del Gran Sasso, Italy) [36]. The MACRO detector is a system of horizontal streamer tube and scintillator counter planes interleaved with absorber plates. The muon direction is determined by the time-of-flight. MACRO has a very good resolution for muons near the vertical direction, but the efficiency decreases rapidly as $\cos\theta_Z$ approces zero. The final MACRO analysis confirms the $\nu_\mu \to \nu_\tau$ oscillation.

Recently, evidence has been shown by the Super Kamiokande collaboration of $\nu_\mu \to \nu_\tau$ oscillations, although this result is, for now, only at $2\sigma$ level [37].

## 1.3 Nuclear reactor experiments

Between experiments only CHOOZ [39] will be mentioned because its results on $\sin^2\theta$, the most costraining today, are directly comparable with the analysis done in this study.

The detector is installed in an underground site under 115 m of rock at a distance of 1114 and 998 m from two 4.25 GW nuclear reactors of the CHOOZ nuclear power plant in France. The detector consists of three concentric

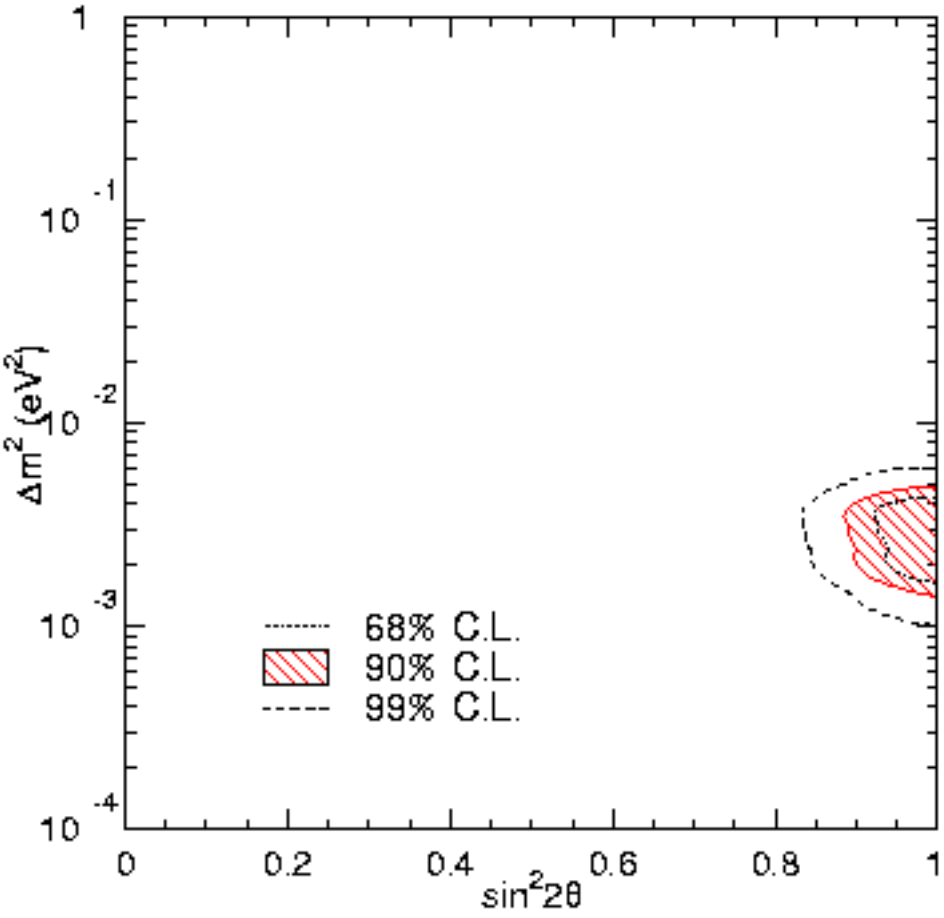


Figure 1.7: Two flavors fit to atmospheric data, at TAU 2000.[38]

vessels. The innermost one contains 5 ton of scintillator ($CH_2$) which acts as the $\bar{\nu}_e$ target. The intermediate vessel also filled with $CH_2$ is used for containment. The outermost vessel acts as a veto counter.
The $\bar{\nu}_e$ are detected by the $e^+$ signal from reaction

$$\bar{\nu}_e + p \rightarrow e^+ + n$$

followed by the delayed signal from neutron capture. The ratio between the measured and expected event rate is, in absence of neutrino oscillations, $0.98 \pm 0.04 \pm 0.04$. Figure (1.8) shows the region of $\bar{\nu}_e \rightarrow \nu_x$ excluded by the CHOOZ experiment at the 90% confidence level. This plot will be compared in the last chapter with the exclusion plot emerging from this study.
Other conceptually similar experiments are in data taking (Palo Verde [40], Arizona U.S.A.) or are planned (KAMLAND [27], Kamioka Japan).

The last kind of neutrino experiments are the accelerator based experiments that will be described in the next chapter.

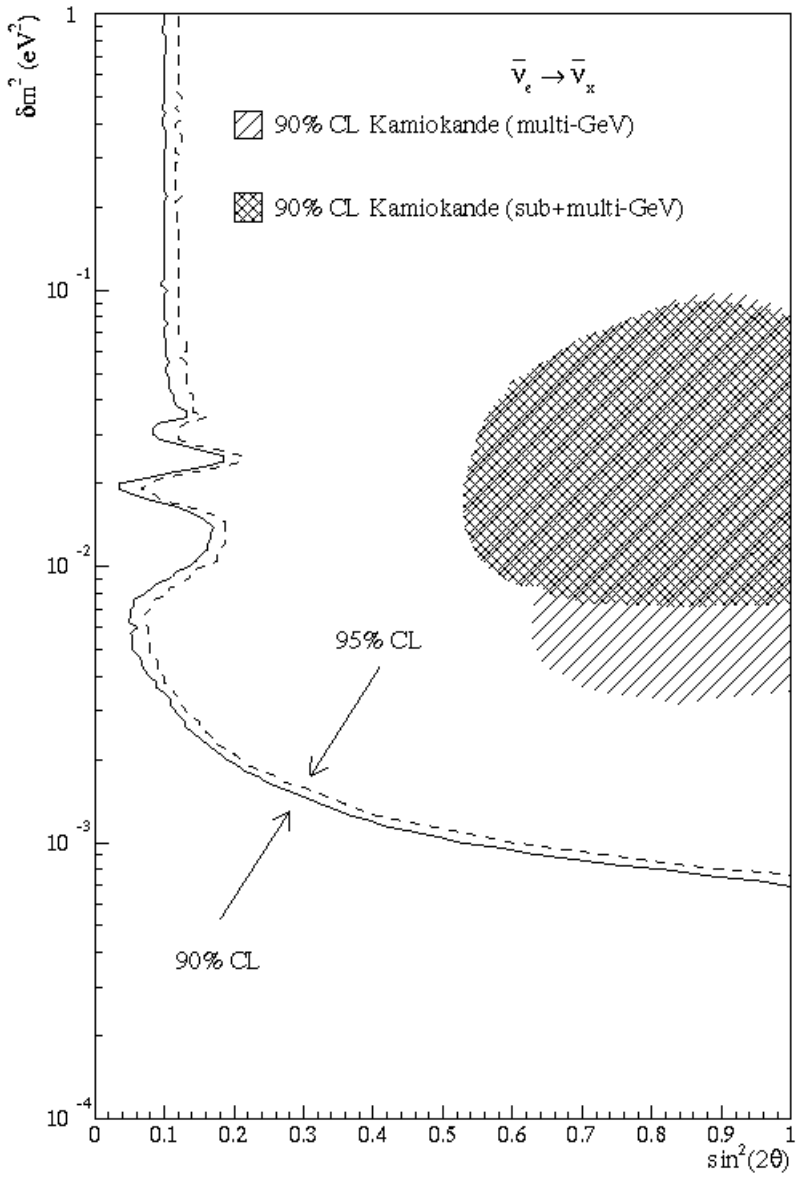


Figure 1.8: CHOOZ exclusion plot. [39]

# Chapter 2

# Neutrino oscillation physics

In the Standard Model leptons are described by three flavour doublets

$$\begin{pmatrix} e \\ \nu_e \end{pmatrix} \begin{pmatrix} \mu \\ \nu_\mu \end{pmatrix} \begin{pmatrix} \tau \\ \nu_\tau \end{pmatrix}$$

Today all these particle have been detected directly. The last being the $\nu_\tau$ with DONUT (in 2000). The definition of flavour eigenstate is experimental: flavour eigenstate is the weak eigenstate under which neutrinos are generated, for example in the following reactions:

$$\pi^+ \rightarrow e^+ + \nu_e$$
$$\pi^+ \rightarrow \mu^+ + \nu_\mu$$
$$\tau^- \rightarrow 2\pi^- + \pi^+ + \nu_\tau$$

or:

$$\nu_e + n \rightarrow p + e^-$$
$$\nu_\mu + n \rightarrow p + \mu^-$$
$$\nu_\tau + n \rightarrow p + \tau^-$$

Lepton number is defined to be the eigenvalue of the lepton number operator:

$$\mathcal{L}_i|\nu_j\rangle = \delta_{ij}|\nu_j\rangle, \ (i = e, \mu, \tau)$$

$$\mathcal{L}_i|\bar{\nu}_j\rangle = -\delta_{ij}|\bar{\nu}_j\rangle, \ (i = e, \mu, \tau)$$

Experiments show that $\mathcal{L}_i$ is a conserved number but, since it is not based on any known symmetry of the weak Lagrangian density, it is possible that is not a fundamental physical law. Neutrino oscillations would violate this principle, although the total lepton number $\mathcal{L} = \sum_i \mathcal{L}_i$, $(i = e, \mu, \tau)$ would still be conserved.
The presence of neutrino oscillations is strictly related to neutrino mass. Neutrino oscillations are only possible if at least one neutrino has non-zero rest mass. In the Standard Model neutrino mass is fixed at zero, hence if neutrino oscillations occur, new physics is necessary beyond the Standard Model.
If eigenstates $|\nu_i\rangle$ of the Hamiltonian of the weak interaction are not mass eigenstates, then a neutrino mixing occurs.
To understand the relation between mass and mixing, the simple case of two generation is considered. The most general mass term in the weak eigenstates basis is[1]

$$\mathcal{L}_m = \bar{\nu} M \nu \tag{2.1}$$

where

$$M = \begin{pmatrix} m_{\nu_e\nu_e} & m_{\nu_e\mu_\mu} \\ m_{\nu_e\nu_\mu} & m_{\nu_\mu\nu_\mu} \end{pmatrix} \tag{2.2}$$

The Lagrangian density can be written explicitly as:

$$\mathcal{L}_m = \bar{\nu}_e m_{\nu_e\nu_e} \nu_e + \bar{\nu}_\mu m_{\nu_e\nu_\mu} \nu_e + \bar{\nu}_e m_{\nu_e\nu_\mu} \nu_\mu + \bar{\nu}_\mu m_{\nu_\mu\nu_\mu} \nu_\mu \tag{2.3}$$

In general this Lagrangian density has non vanishing off-diagonal elements, but being a $\mathbb{R}$ symmetrical matrix it is possible to diagonalize it with a unitary transformation $U$:

$$\tilde{M} = U M U^\dagger \tag{2.4}$$

$$\tilde{M} = \begin{pmatrix} m_1 & 0 \\ 0 & m_2 \end{pmatrix}, U = \begin{pmatrix} \cos\theta & -\sin\theta \\ \sin\theta & \cos\theta \end{pmatrix} \tag{2.5}$$

Then it is possible to write:

$$\begin{pmatrix} \nu_e \\ \nu_\mu \end{pmatrix} = \begin{pmatrix} \cos\theta & \sin\theta \\ -\sin\theta & \cos\theta \end{pmatrix} \begin{pmatrix} \nu_1 \\ \nu_2 \end{pmatrix} \tag{2.6}$$

[1]Here and in the following will always be considered Dirac particle and no CP violation. Natural units will be used $\hbar = c = 1$.

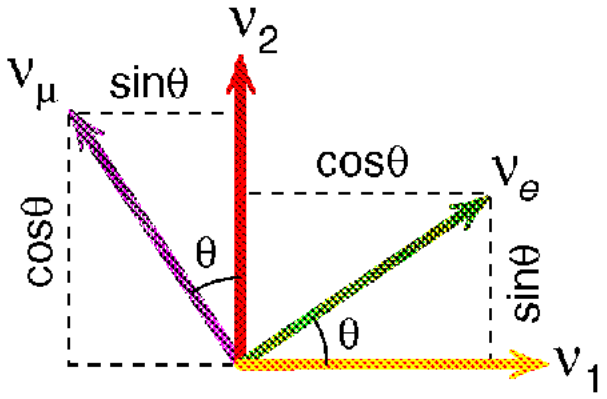


Figure 2.1: Two generation neutrino mixing.

The mass eigenvalues $m_1$, $m_2$, are:

$$m_{1,2} = \frac{1}{2}\left[m_{\nu_e\nu_e} + m_{\nu_\mu\nu_\mu} \pm \sqrt{(m_{\nu_e\nu_e} - m_{\nu_\mu\nu_\mu})^2 + 4m^2_{\nu_e\nu_\mu}}\right] \tag{2.7}$$

and the mixing angle is:

$$\tan 2\theta = \frac{2m_{\nu_e\nu_\mu}}{m_{\nu_\mu\nu_\mu} - m_{\nu_e\nu_e}} \tag{2.8}$$

It is possible to represent this mixing as a rotation in a bi-dimensional space with the two bases $(|\nu_1\rangle, |\nu_2\rangle)$ and $(|\nu_e\rangle, |\nu_\mu\rangle)$, figure (2.1)

## 2.1 Oscillation formalism

Neutrino oscillations can be described with the general formalism of quantum mechanics.[41]
As shown in the previuos section flavour eigenstates $|\nu_i\rangle$, $(i = e, \mu, \tau)$ are the mixing of several mass eigenstate $|\nu_\alpha\rangle$, $(\alpha = 1, 2, 3)$. If mass differences $m_\alpha - m_\beta$ are smaller than the experimental resolution, the correspondent $|\nu_\alpha\rangle$, $|\nu_\beta\rangle$ eigenstates are indistinguishable, thus flavour eigenstates are described with a coherent superposition of mass eigenstates:

$$|\nu_i\rangle = \sum_\alpha U_{i\alpha}|\nu_\alpha\rangle \tag{2.9}$$

U is a $3 \times 3$ unitary matrix that associates mass eigenstates basis with the flavour eigenstates. Considering no CP violation U is a $\mathbb{R}$ orthogonal matrix. When a neutrino is generated at $t = 0$ in a certain position $x$ it is, by definition, in a definite flavour eigenstate, and can be described as a superposition of different mass eigenstates:

$$|\nu_i\rangle = |\nu(\vec{x}, 0)\rangle = \sum_\alpha U_{i\alpha} |\nu_\alpha(\vec{x}, 0)\rangle = \sum_\alpha U_{i\alpha} e^{-i\vec{p}_\alpha \cdot \vec{x}} |\nu_\alpha\rangle \tag{2.10}$$

At a later time, applying the time-evolution operator to the previous expression:

$$|\nu(\vec{x}, t)\rangle = \sum_\alpha U_{i\alpha} e^{i\vec{p}_\alpha \cdot \vec{x}} e^{-iE_\alpha t} |\nu_\alpha\rangle \tag{2.11}$$

Neutrinos can always be considered ultrarelativistic particles, hence it is possible to use the approximation $m_\alpha \ll p_\alpha$,

$$E_\alpha = \sqrt{m_\alpha^2 + p_\alpha^2} \simeq p_\alpha + \frac{m_\alpha^2}{2p_\alpha} \tag{2.12}$$

then (2.11) can be written as:

$$|\nu(\vec{x}, t)\rangle = \sum_\alpha U_{i\alpha} e^{-i\frac{m_\alpha^2}{2p_\alpha} t} |\nu_\alpha\rangle \tag{2.13}$$

It is possible to go from the mass eigenstates basis to weak eigenstates:

$$|\nu_\alpha\rangle = \sum_k U_{k\alpha} |\nu_k\rangle \tag{2.14}$$

and the (2.13) becomes:

$$|\nu(\vec{x}, t)\rangle = \sum_k \left[ \sum_\alpha U_{k\alpha} U_{i\alpha} e^{-i\frac{m_\alpha^2}{2p_\alpha} t} \right] |\nu_k\rangle \tag{2.15}$$

It is possible to note that a flavour eigenstate at time t=0 in the position x, becomes a superposition of all flavours.
To calculate the transition probability $\nu_i \to \nu_l$ $(i \neq l)$ it is necessary to calculate the probability amplitude :

$$A_{i \to l}(x) = \langle \nu_l | \nu(\vec{x}, t) \rangle = \sum_k \sum_\alpha U_{k\alpha} U_{i\alpha} e^{-i\frac{m_\alpha^2}{2p_\alpha} t} \langle \nu_l | \nu_k \rangle =$$

$$= \sum_{\alpha} U_{l\alpha} U_{i\alpha} e^{-i \frac{m_\alpha^2}{2p_\alpha} t} \tag{2.16}$$

The probability that a neutrino, created in a weak eigenstate $|\nu_i\rangle$ is, at time t, in the state $|\nu_l\rangle$ is given by the square of the absolute value of the amplitude:

$$P_{i\to l}(t) = |A_{i\to l}(t)|^2 \tag{2.17}$$

$$P_{i\to l}(t) = \sum_{\alpha}\sum_{\beta} U_{l\alpha} U_{i\alpha} U_{l\beta} U_{i\beta} e^{-i\left(\frac{m_\alpha^2}{2p_\alpha} - \frac{m_\beta^2}{2p_\beta}\right) t} \tag{2.18}$$

By the assumption $m_\alpha \ll p_\alpha$ and $m_\beta \ll p_\beta$, then $p_\alpha = p_\beta = p$ and (2.18) becomes:

$$P_{i\to l}(t) = \sum_{\alpha}\sum_{\beta} U_{l\alpha} U_{i\alpha} U_{l\beta} U_{i\beta} e^{-i\left(\frac{\Delta m_{\alpha\beta}^2}{2p}\right) t} \tag{2.19}$$

Since $v \simeq c$ then $t \simeq x$ and (2.19) can be written as

$$P_{i\to l}(x) = \sum_{\alpha}\sum_{\beta} U_{l\alpha} U_{i\alpha} U_{l\beta} U_{i\beta} e^{-i\left(\frac{\Delta m_{\alpha\beta}^2}{2p}\right) x} \tag{2.20}$$

This probability varies periodically with distance (time) from the source. The periodicity is characterized by the oscillation length:

$$L_{\alpha\beta} = \frac{4\pi p}{\Delta m_{\alpha\beta}^2} = \frac{4\pi E}{\Delta m_{\alpha\beta}^2} \tag{2.21}$$

It is important to observe that if all masses are identical, or if all mass vanish, no oscillation would occur ($L_{\alpha\beta} \to \infty$)

## 2.2 Two family oscillations

To discuss general features about oscillations probability it is easier to consider the simple case of two neutrino flavours. To fix the notation flavour eigenstates will be $|\nu_e\rangle, |\nu_\mu\rangle$ while mass eigenstates will be $|\nu_1\rangle, |\nu_2\rangle$
The mixing matrix is a $2 \times 2$ orthogonal matrix identical to (2.5); then, in the mass basis the states $|\nu_e\rangle$ and $|\nu_\mu\rangle$ can be written explicitly:

$$|\nu_e\rangle = \cos\theta |\nu_1\rangle + \sin\theta |\nu_2\rangle \tag{2.22}$$

$$|\nu_\mu\rangle = -\sin|\nu_1\rangle + \cos\theta|\nu_2\rangle \tag{2.23}$$

The expression (2.20) can be written with the cartesian notation of the imaginary exponential as:

$$P_{\nu_\mu\to\nu_e}(t) = \sin^2(2\theta)\sin^2(\frac{\Delta m^2 x}{4E}) \tag{2.24}$$

The oscillation formula is composed by two terms: the first one depending on the mixing angle $\theta$ fixes the amplitude, while the second, depending on $\Delta m^2 = (m_2^2 - m_1^2)$, x, E, is the oscillatory term.
The oscillation length is :

$$L = \frac{4\pi E}{\Delta m^2} \tag{2.25}$$

Fixing $\theta = \frac{\pi}{4}$ (maximum mixing) when a $\nu_\mu$ is at the points $x = L(n + 1/2)$ it fully oscillated into a $\nu_e$.
There is an important observation regarding the dimensions of the neutrino source and detector. These two lengths must be compared with the oscillation length L. If L is too small compared with the length of the decay tunnel at the production or again too small with respect to the detector linear size, the oscillation probability will be averaged on the oscillatory term depending on x,

$$\langle P_{\nu_\mu\to\nu_e}(x)\rangle_L = \frac{1}{2}\sin^2(2\theta)$$

and the only possible measurement would be on the mixing angle.

## 2.3 Three family oscillations

In the case of three neutrino flavours, the mixing matrix U is a $3 \times 3$ orthogonal matrix.

$$\begin{pmatrix} \nu_e \\ \nu_\mu \\ \nu_\tau \end{pmatrix} = \begin{pmatrix} U_{e1} & U_{e2} & U_{e3} \\ U_{\mu 1} & U_{\mu 2} & U_{\mu 3} \\ U_{\tau 1} & U_{\tau 2} & U_{\tau 3} \end{pmatrix} \begin{pmatrix} \nu_1 \\ \nu_2 \\ \nu_3 \end{pmatrix} \tag{2.26}$$

As in the two dimensional case neutrino mixing could be seen as a rotation in a two dimensional space, here it is possible to look at mixing as a rotation in a three dimensional space, with the usual definition of Euler angles $\theta_{12}$, $\theta_{23}$, $\theta_{13}$ as shown in figure (2.2).
U can be written as:

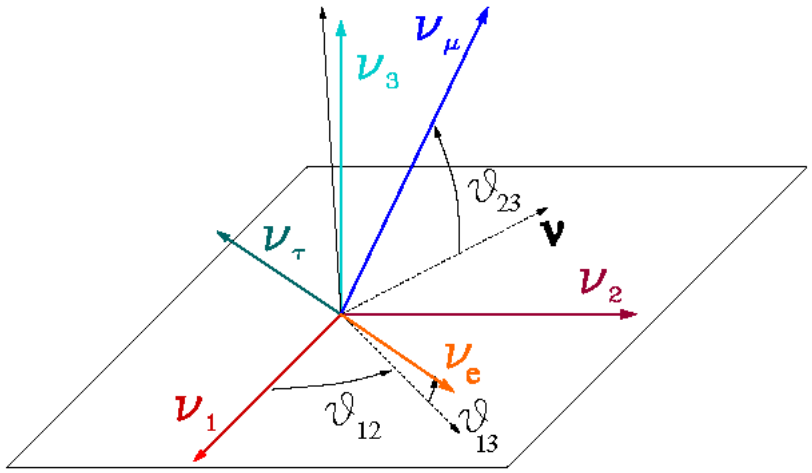


Figure 2.2: Three generation neutrino mixing as a rotation parametrized with Euler angles.

$$U = \begin{pmatrix} c_{12}c_{13} & s_{12}c_{13} & s_{13} \\ -s_{12}c_{23} - c_{12}s_{23}s_{13} & c_{12}c_{23} - s_{12}s_{23}s_{13} & s_{23}c_{13} \\ s_{12}s_{23} - c_{12}c_{23}s_{13} & -c_{12}s_{23} - s_{12}c_{23}s_{13} & c_{23}c_{13} \end{pmatrix} \tag{2.27}$$

where $c_{ij} = \cos\theta_{ij}$ and $s_{ij} = \sin\theta_{ij}$.
Equation (2.20) can be written explicitly in a trigonometrical form as:

$$\begin{aligned} P_{\nu_i \to \nu_l}(x) = \quad & -4U_{i2}U_{i3}U_{l2}U_{l3}\sin^2\Delta_{32} \\ & -4U_{i1}U_{i3}U_{l1}U_{l3}\sin^2\Delta_{31} \\ & -4U_{i1}U_{i2}U_{l1}U_{l2}\sin^2\Delta_{21} \end{aligned} \tag{2.28}$$

where

$$\Delta_{ij} = \frac{1.27\delta m^2_{ij}\, x}{E}$$

and $\delta m^2_{ij} = (m^2_i - m^2_j)$, having expressed length in km mass in $eV^2$ and energy in GeV.
In the case of interest for this study the oscillations considered are $\nu_\mu \to \nu_e$. Using the parameters suggested by the LMA (Large Mixing Angle) solution (see chapter 1) the previous formula can be approximated to:

$$P_{\nu_\nu \to \nu_e}(x) = sin^2(2\theta_{13})\sin^2(\theta_{23})\sin^2\left(\frac{1.27\delta m^2_{23}\, x}{E}\right) \tag{2.29}$$

considering $\delta m^2_{12} = 5\,10^{-5} eV^2$ negligible with respect to $\delta m^2_{23} \simeq \delta m^2_{13} = 3.2\,10^{-3} eV^2$ and considering the fact that the matrix is unitary.
There are anyway some limitations in the use of this simplified formula. As explained in the previous chapter there isn't an univocal set of values fitting all the experimental data. In this study the so called LMA (large mixing angle) solution has been chosen:

$$\begin{array}{rl} \sin^2(2\theta_{12}) = & 0.8 \\ \sin^2(\theta_{23}) = & 0.5 \\ \sin^2(2\theta_{13}) = & 0.01 \end{array} \tag{2.30}$$

and the following mass difference values:

$$\begin{array}{rl} \delta m^2_{12} = & 5\,10^{-5} eV^2 \\ \delta m^2_{23} = & 3.2\,10^{-3} eV^2 \\ \delta m^2_{13} = & 3.25\,10^{-3} eV^2 \end{array} \tag{2.31}$$

Considering the LMA solution it is not possible to neglect $\delta m^2_{12}$. The three terms in (2.28) have different weights and even if $\delta m^2_{12}$ is two order of magnitude lower than $\delta m^2_{23}$ the approximation is not adeguate. This is shown clearly in the difference between the two figures (2.3),(2.4).

One last observation is necessary about the oscillation probability as function of the distance x. The simplified formula is a squared sinus with amplitude $\sin^2(2\theta_{13})\sin^2(\theta_{23})$ and oscillation period $L = \pi E/1.27\delta m^2$, figure (2.5). The complete formula is the superposition of three squared sinus hence its shape is as shown in figures (2.6),(2.7), with different resolutions. In our analysis anyway, as will be explained in chapter 4, only the first peak will be used.

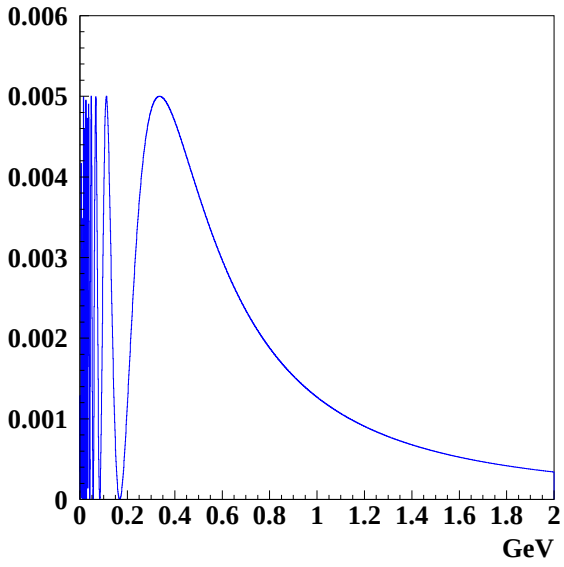


Figure 2.3: Oscillation probability for a fixed L=130 km calculated with the approximated formula

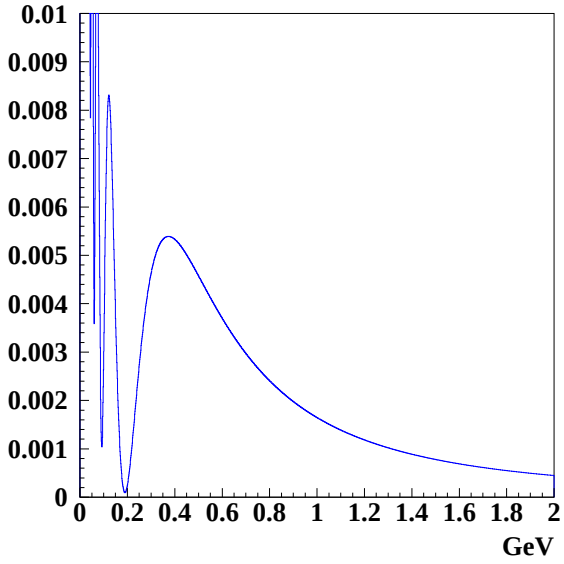


Figure 2.4: Oscillation probability for a fixed L=130 km calculated with the complete formula

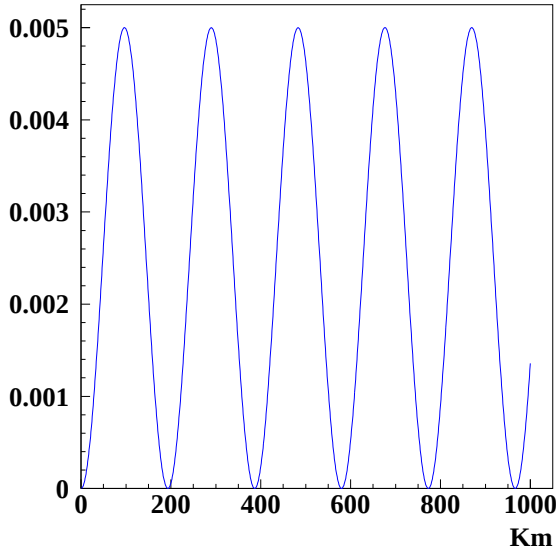


Figure 2.5: Oscillation probability for E=0.250 GeV as a function of the distance calculated with the approximate formula.

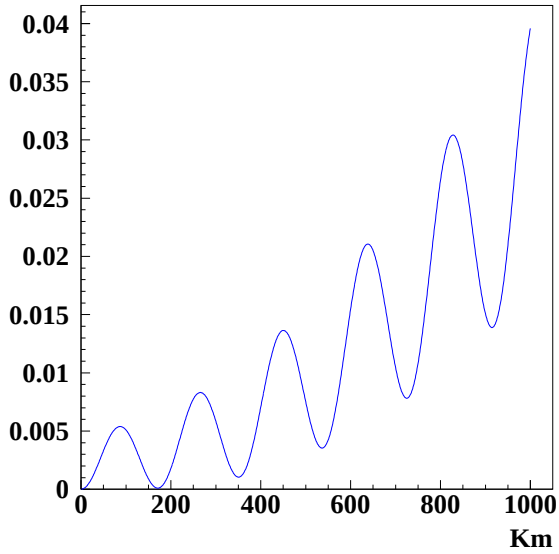


Figure 2.6: Oscillation probability for E=0.250 GeV as a function of the distance calculated with the complete formula.

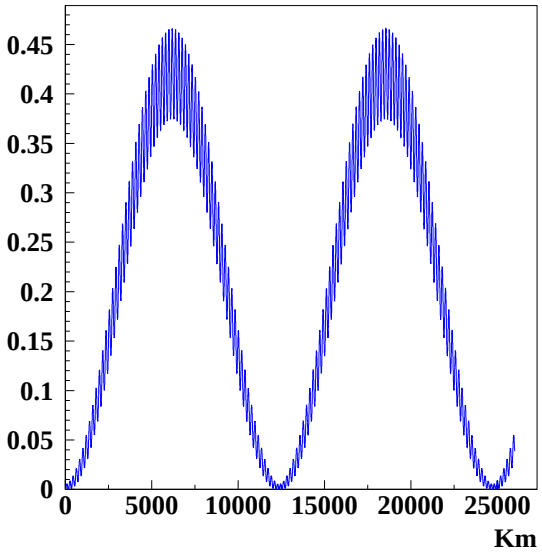


Figure 2.7: Oscillation probability for E=0.250 GeV as a function of the distance calculated with the complete formula.

# Chapter 3

# Superbeam

Neutrino oscillations studies generally concern the observation of neutrinos coming from the Sun or from interaction of primary cosmic rays with the atmosphere. The general problem related with these experiments is the impossibility to know the real initial neutrino flux. Neutrino experiments which avoid this problem are the accelerator based experiments.
The general way to produce neutrino beam is to make a proton beam impinging on a target. Depending on the energy of the protons, pions and kaons and other particles are produced. They are collected with a focusing system and finally they decay in a decay tunnel. Neutrino beams from accelerators can have energies from few MeV up to several GeV.
Neutrino beams can be divided according to their energy spread into two classes: narrow band and wide band neutrino beams. Wide band are generally produced with a horn-focused pion-kaon beam (magnetic horn will be discussed later) while narrow beams come from momentum selected pions and kaons.
There are two main kind of experimental set up for accelerator based neutrino experiments: short baseline and long baseline. For short baseline usually is intended few meters between the neutrino production point and the detector, while in a long baseline configuration there can be several km from target to detector.
In the following some short baseline and long baseline neutrino beam are briefly described. None of these experiment has data directly comparable with the results of the present study.
LSND (Liquid Scintillator Neutrino Detector) [42] and the KARMEN (KArlsruhe Rutherford Medium Energy Neutrino) [43] experiments use neutrinos

produced in a proton beam dump. LSND is at LANSCE (Los Alamos Laboratory Neutron Science CEnter) and KARMEN at the ISIS neutron spallation source, Rutherford Appleton Laboratory. For both the proton beam energy is of 800 MeV. In these experiment neutrinos are produced by the decay of pions and muons, and have an energy of the order of tens of MeV. These experiments search for neutrino oscillations $\nu_\mu \rightarrow \nu_e$ and $\bar{\nu}_\mu \rightarrow \bar{\nu}_e$. LSND uses a 167 ton mineral oil detector and gives evidence for an excess of $\bar{\nu}_e$ events. In KARMEN neutrinos are detected in a 56 ton scintillation calorimeter situated at a distance of approximately 18 m from the source and is still in data taking.

Future research on $\nu_\mu \rightarrow \nu_e$ oscillations are planned at Fermilab with MiniBooNE (Booster Neutrino Experiment) [44] which is the first phase of the high sensitivity experiment BooNE. Neutrinos are produced using the 8 GeV high intensity proton beam from the Fermilab Booster synchrotron. The beam consists mainly in $\nu_\mu$ from $\pi^+$ decay with a broad energy from 0.3 to 2 GeV. The MiniBooNE detector (which will be briefly described in the fifth chapter), will be installed at 500 m from the neutrino source.

Two experiments searching for $\nu_\mu \rightarrow \nu_\tau$ oscillations CHORUS (CERN Hybrid Oscillation Research apparatUS) [45] and NOMAD (Neutrino Oscillation MAgnetic Detector) [46] have recently completed their data taking at CERN. Both used the wide band neutrino beam from the CERN 450 GeV SPS (Super Proton Synchrotron). The method adopted by both experiments consists in detecting $\tau^-$ production with high sensitivity. The two experiments are installed one behind the other at a distance of $\simeq$820 m from the proton target. CHORUS uses an emulsion detector which provide the high resolution of $\simeq 1\mu$m well matched to the averaged $\tau^-$ decay length of 1 mm. While NOMAD is designed to observe $\tau^-$ production using kinematical criteria, which requires the precise measurement of secondary particles momenta.

The other class of neutrino experiments are long baseline accelerator experiments which have the aim to verify atmospheric neutrino results ($\nu_\mu \rightarrow \nu_\tau$ oscillations).

The K2K [47] project uses neutrinos at a mean energy of 1.4 GeV from the decay of pions and kaons produced by the KEK 12 GeV proton synchrotron. Two detectors located at different distances are used. The near one to study precisely neutrino beam spectra and cross sections, and the Super Kamiokande detector at 250 km to verify the oscillation hypothesis. Neutrino energy is below the $\tau$ production threshold, hence it is not possible to search for $\tau$ appearance. K2K is presently in data taking

The NuMI [48] project uses neutrinos from the decay of pions and kaons produced by the Fermilab Main Injector (MI), a 120 GeV proton synchrotron. The expected number of proton on target is 3.6 $10^{20}$/y. The detector of this experiment will be located in the Soudan mine at a distance of 730 km from the proton target.
The MINOS [48] experiment (Main Injector Neutrino Oscillations Search) will use two detectors, a near one at Fermilab and another one to be built at the Soudan site. Both detectors are iron-scintillator sandwich calorimeter with a magnetic field in the iron plates. The comparison between the fluxes measured by the two will be sensitive to neutrino oscillations.
The CNGS project consists in a neutrino beam from the CERN 450 GeV SPS to the LNGS (Laboratori Nazionali del Gran Sasso, Italy) at a distance of 732 km. The detailed description of the beam design can be found in [49]. A possible detector for this experiment can be ICARUS (Imaging Cosmic And Rare Underground Signal) [50]. This is a new type of detector based on a liquid Argon time projection chamber, which allows three-dimensional reconstruction of events with spatial resolution of the order of mm.
A new ambitious program in accelerator based neutrino experiment is the Neutrino Factory [51], where neutrinos are produced with a muon storage ring. A very schematic layout of the Neutrino Factory complex is shown in figure (3.1). The first object of the complex is a proton beam of 4 MW onto a high-Z target. The actual configuration in study at CERN uses the SPL (Superconducting Proton Linac, which will be briefly described in the next section) that accelerates protons up to a kinetic energy of 2.2 GeV. Due to the low energy of protons, kaon production is strongly suppressed. The target is placed in a magnetic horn (see figure (3.3)) which collects and focuses pions in the centre of a solenoid. After a drift space where pions decay, the decay muons are "cooled", i.e. the muons volume in the six dimensional phase space is reduced. Since muons are unstable (lifetime of 2.2$\mu s$) all further actions on them must be highly efficient so as to accelerate them as quickly as possible up to their final energy of 50 GeV, profiting to a maximum from Lorentz time dilation. Finally muons enter the storage ring. The storage ring has two straight sections, each pointing to detectors at different distances. The nearer one should be located at the LNGS (Laboratori Nazionali del Gran Sasso, Italy) at 732 km and a second one should be located farther away at approximately 2500 3000 km. The proposed sites for the far detector are "Santa Cruz de la Palma" (Spain) [52] or "Longyearbyen" at Svalbard islands (Norway) [53].

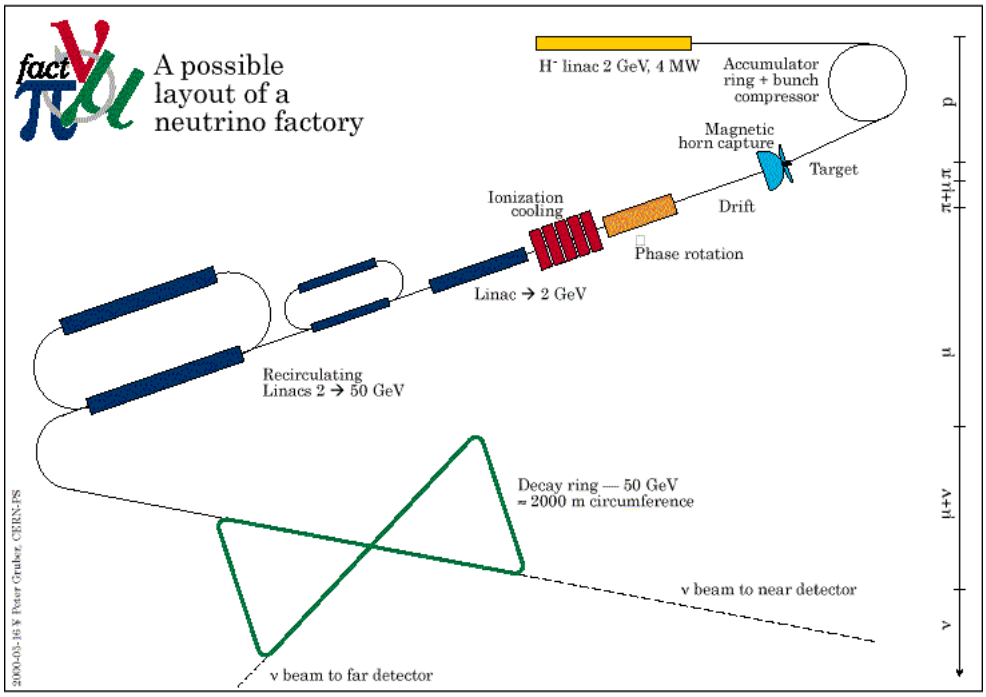


Figure 3.1: Neutrino Factory layout.

An intermediate step between conventional neutrino beams and the Neutrino Factory is possible with the new era of MW-scale proton accelerators. A conventional neutrino superbeam is a neutrino beam coming from the decay of $\pi^{\pm}$, but using a very intense MW-scale proton source. The present study will analyze a possible superbeam configuration at CERN.

## 3.1 Considered configuration

The considered superbeam configuration is the option that became possible at CERN with the SPL. The target and focusing system used in this study are the preliminary set up for the Neutrino Factory components. The decay tunnel can be seen as the only superbeam dedicated component of the whole project (obviously excluding detectors).

| | |
|---|---|
| Mean beam power | 4MW |
| Kinetic energy | 2.2 GeV |
| Repetition rate | 75Hz |
| Pulse duration | 2.2 ms |
| Number of protons per pulse (per second) | $1.5\ 10^{14}(1.1\ 10^{16})$ |
| Mean current during a pulse | 11 mA |
| Overall lenght | 799 m |
| Bunch frequency (minimum time between bunches) | 352.2 MHz (2.84 ns) |

Table 3.1: Basic SPL characteristics

## 3.2 SPL

The Neutrino Factory collaboration estimates in $10^{21}$ the number of muons per year necessary to reach the published physics purpose [51]. To do this a high intensity proton accelerator is necessary.
To cope with these requirements CERN has moved to the new era of the MW-scale accelerators with the SPL (Superconductiong Proton Linac) [55]. The basic parameters of the SPL are reported in table (3.1). The design of the accelerator is based upon the re-use of the LEP RF equipment available with LEP dismantling. Out of the 800 m of Linac length, more than 500 m are equipped with LEP-2 cryostats, while the low energy part, up to 390 MeV($\simeq$ 280 m), is of a completely new design.
The performance of the SPL have been studied basically for the Neutrino Factory project. However, if these requirements will change after the HARP experimental results (see next section), or for new physics goals, it would still be possible to modify some of the above cited parameters. In particular the possiblity to run SPL at higher power has been studied.

## 3.3 Target

Pions are produced with the interactions of the SPL proton beam with a target. The target used in this study is the one developed for the Neutrino Factory. The target to use to produce pions with a proton beam of 4 MW must satisfy some important characteristics:

- have the largest possible pion production rate per proton

- stand at the mechanical shock of the impinging proton beam

- stand at the thermal shock of the impinging proton beam

The first point is the most important from the physics point of view. In fact the number of final neutrinos in the detector is directly related to the number of pions produced. The pion production is related to the A (atomic number) of the target. The larger A the more pions are produced. However, the interaction between the 2.2 GeV proton beam and the target is particularly difficult to estimate. In fact not enough precise cross sections are available for these energies. The HARP [67] experiment is about to take data to measure these values. The target studies are performed with Monte Carlo simulations. The computer code used for these simulations are usually FLUKA or MARS. Unfortunatly in this energy range the compared results of the two are very different (40%). The code used for this target simulations is MARS [54]. However it is necessary to remember that the final pion flux obtained is affected by large uncertainties $\simeq 50\%$.
Thermal response of the target is very important in a study of pion production with a proton beam of 4 MW. When the beam impinges on the target it creates a shock wave that tends to blow it away. Using a solid target would require to replace it very often because of the stress it has to substain. The presently favoured solution for the Neutrino Factory is the use of a liquid target. Mercury has been chosen because it has a large A and because its handling technology is advanced. The mercury target is a cylinder of 26 cm length and 0.75 cm radius. These dimensions are chosen to be $\simeq 2\,\lambda_I$ (interactions lengths) and large enough to cover the dimensions of the impinging proton beam (which is $\sigma_x = \sigma_y = 0.3$ cm). The mercury jet is injected in the focusing system where it is hit by the proton beam. The choice of a liquid target solve the problem of thermal and mechanical resistance because the liquid jet is continuously replaced. However it raises other interesting problems, such as the collection of the mercury after interaction with the proton beam.
A general problem of target handling is the activation of the material after the interactions with protons. All the mercury used in this experiment will be filtered, treated and the residues stocked as radioactive material.

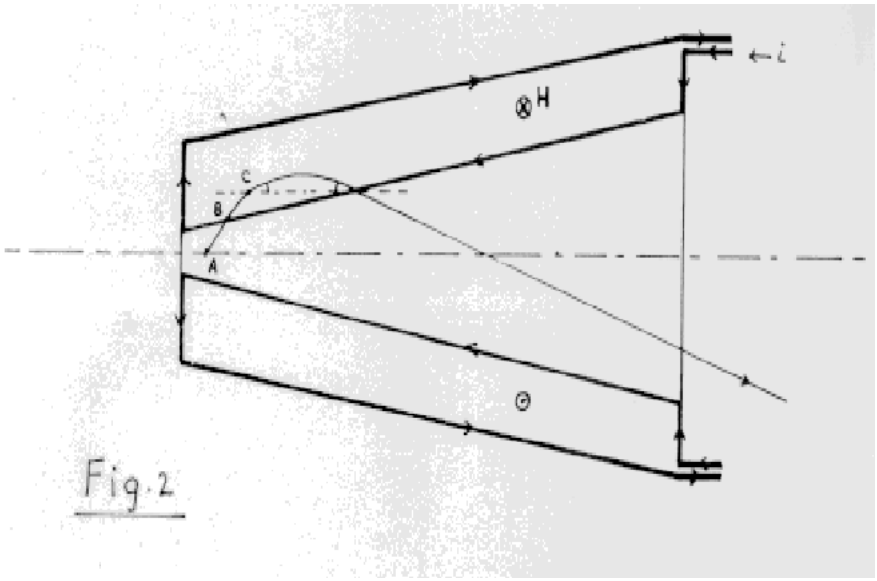


Figure 3.2: Magnetic horn in the original drawing of S. Van der Meer.

## 3.4 Focusing system: magnetic horn

Since there is no way to deviate neutrinos and directly focus them, it is necessary to act upon the parent particles. The pion focusing system must be considered as directly responsible of the final neutrino focusing. As will be explained in the next chapter the low energy of the pions is the fundamental reason of the non-perfect focusing of neutrinos. In fact neutrinos emitted from a pion at rest are isotropically distributed over the whole solid angle. The higher the momentum of the pions the higher is the focusing of neutrino due to Lorentz boost.
A magnetic horn is the solution proposed for this study and it is presently under analysis by the Neutrino Factory working group. The magnetic horn was invented by S. Van der Meer in 1961. This system is composed by two coaxial conductors an inner one and an outer one. The current flows in the conductors along the axis direction (see figure (3.2)) and creates a toroidal magnetic field between the conductors. The target is usually placed at the beginning of the horn or just inside it, where no magnetic field is present. When a particle is produced goes through the first layer of the horn conductor; inside the horn it feels a magnetic field transverse to its momentum. As can be seen in figure (3.2) the effect of this field is to bend the trajectory of

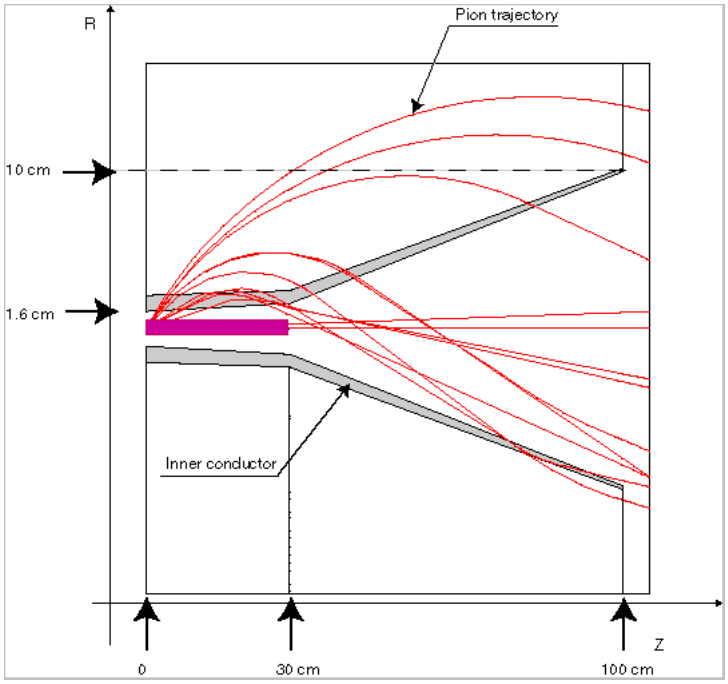


Figure 3.3: Neutrino Factory horn. (purple) The target and (red lines) pion trajectories.[56]

the particle towards a focus. For a fixed current polarity the focused particles can be only of one sign. When the magnetic field is focusing a charge is clearly defocusing the other. For this reason magnetic horns are said to be charge selectives.
The particular shape of the horn used in this study is the one conceived for the Neutrino Factory and can be seen in figure (3.3) [56]. The thickness of the horn is 16 mm around the target and 1.8 mm at the end.
In figure (3.4) the initial total and transverse pion momentum is shown, while in figure (3.5) is shown the effect of the horn on the transverse momentum. In figure (3.6) the pion space distribution is shown.

This horn is called point to point because particles created in one focus of the horn are focused in the other one. In a Neutrino Factory it is necessary to put as many pions as possible into a solenoid where they will decay emitting the desidered muons. For the superbeam needs it would be better to use a point to parallel horn, i.e. particles produced in the focus of the horn are focused along parallel trajectories toward the decay tunnel.

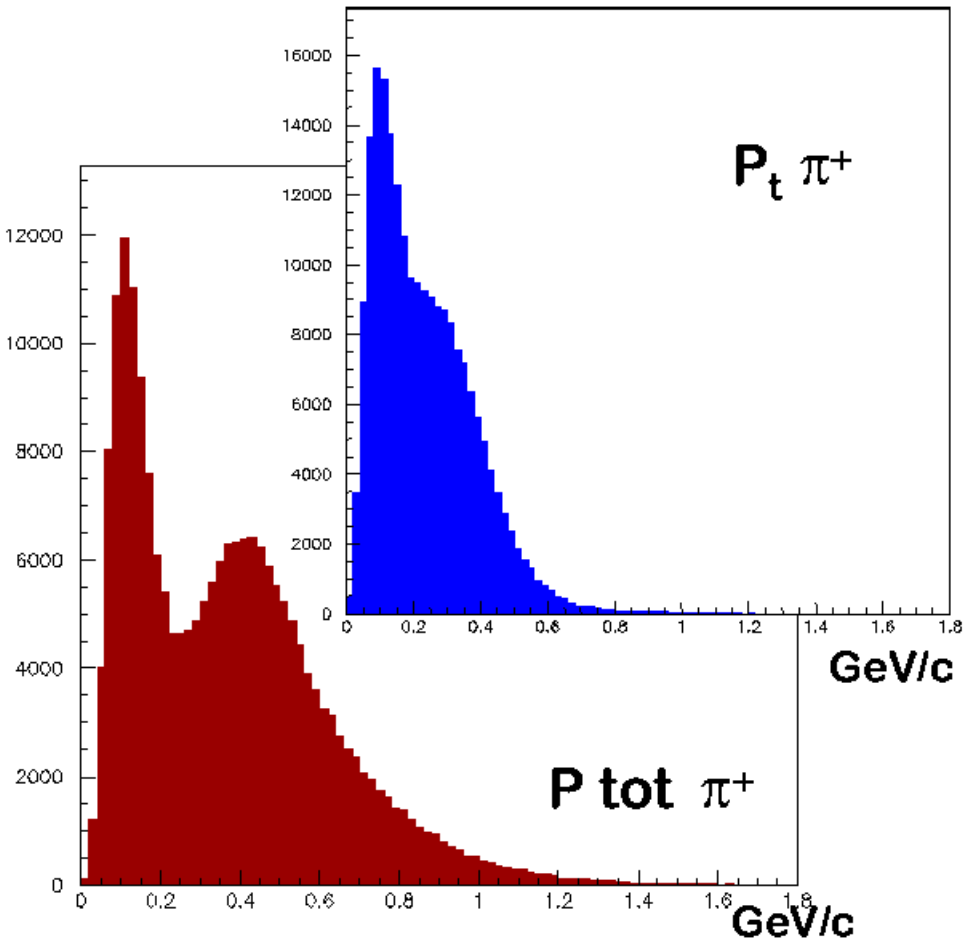


Figure 3.4: Pion total and transverse momentum before the horn.

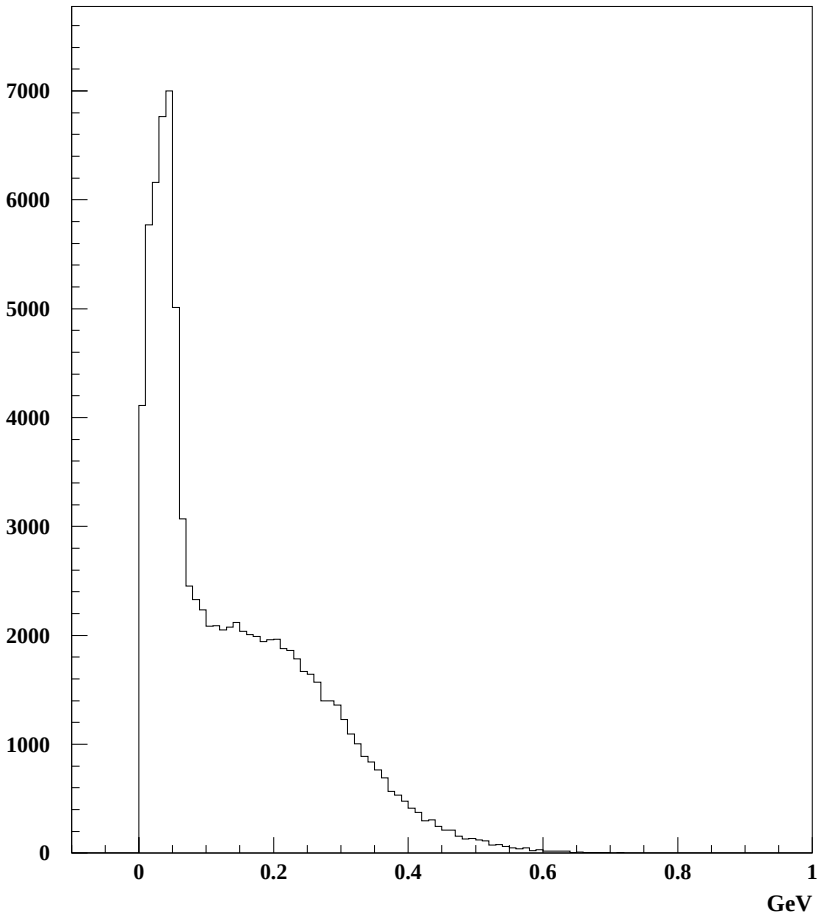


Figure 3.5: Effect of the horn on the transverse momentum.

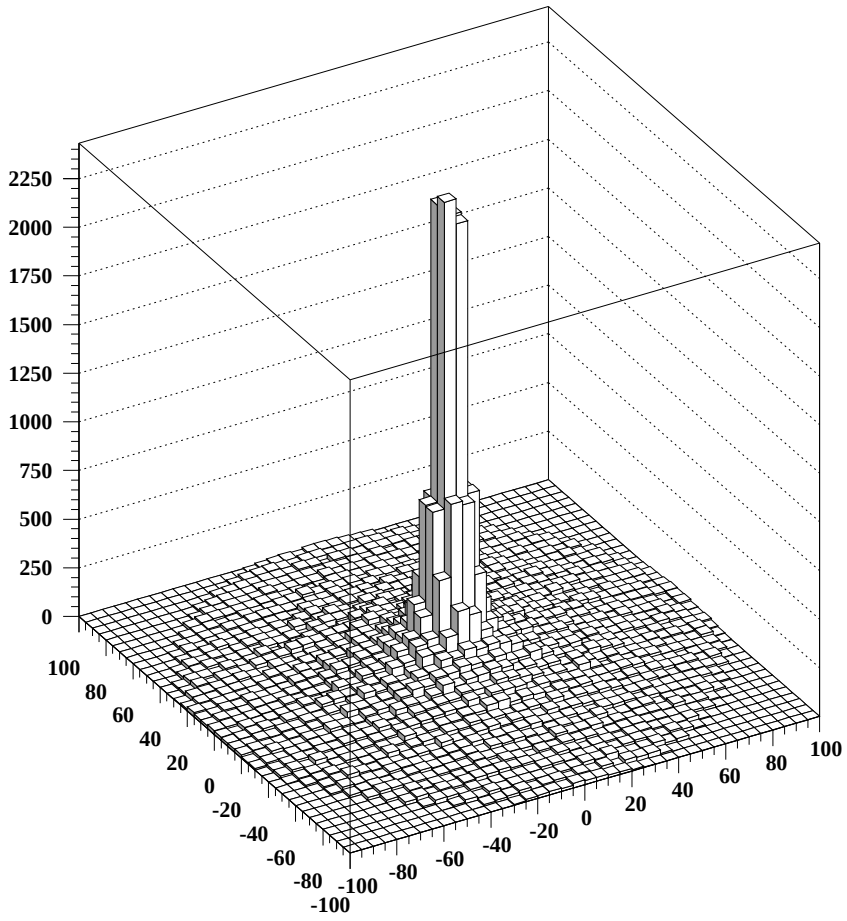


Figure 3.6: Pion space distribution.

This configuration is presently under study. The proposed geometry of this focusing system could be composed by two horns: a first focusing horn and a second defocusing one called reflector. This device acts as as the optical system of converging and diverging lenses.
The magnetic horn is the choice for the focusing system also for its radiation resistance. In fact in the interactions of protons with the target a lot of secondary particles are produced, in particular neutrons. The mean life of a horn in this severe radiation environment is of few weeks. In this perpective the low cost of this system becomes relevant. The AC current flowing in the horn is about 300 kA with a frequency of 50 Hz. The resistance of the horn to this mechanical stress is presently under study.

## 3.5 Decay tunnel

The kind of experiment that will be performed with this neutrino beam is commonly called an appearance experiment. That means it is necessary to observe the appearance of $\nu_e$ in a $\nu_\mu$ beam. The physics studies performed with this neutrino beam are heavily influenced by its purity. In the ideal case of pure $\nu_\mu$ beam even a single electronic neutrino interaction would be the clear sign of oscillations. In the real case the beam is contaminated by the $\nu_e$ coming from the decay muons. The low energy of the SPL suppresses almost entirely kaon production.
The only way to act on the purity of the beam is to work on the geometry of the decay tunnel. Considering, for symmetry reasons a cylindrical decay tunnel, the only two characteristics that can be modified are its length and radius. Pion and muons in the decay tunnel have basically two different characteristics: different mean lives, and different trajectory angles.
Pion and muon mean lives are
$\tau_\pi = 2.6\,10^{-8} s$;
$\tau_\mu = 2.2\,10^{-6} s$;
or in the more convenient length units:
$c\tau_\pi = 7.8\,m$;
$c\tau_\mu = 658.7\,m$.
The length of the decay tunnel must be a compromise between the maximum number of pions decay in flight and the lowest number of muons decay in flight. It is important to observe that the energy spectrum of neutrinos from pions and muons decay is dependent on the length of the decay tunnel. In

fact with a short decay tunnel only particles with very low energy would decay, and the emitted neutrinos would be at low energy as well; while for long decay tunnel also pions with higher energy would decay, causing the peak of the neutrino distribution to move towards higher energy. The same argument is valid for muons.
In this study it has been assumed that pions and muons are immediatly captured by the tunnel walls or its end plates and no further decay is assumed. This is a good approximation for neutrino fluxes considerations, in fact the emitted neutrinos from muon and pion capture are at very low energy and almost isotropically distributed, hence their probability to reach the detector is negligible.
Pions after the magnetic horn have relatively low transverse momentum, hence they can flight for some meters before hitting the tunnel walls or the end plates. Muons emitted from pions, on the contrary, are emitted isotropically in the center of mass of the pion, and feel only the weak focusing effect due to the Lorentz boost. Hence muons have big angles with respect to the tunnel decay axis; their flight is short and their probability to decay in flight is small. The outer radius of the magnetic horn is 1 m hence it is useless to consider larger decay tunnels, but a shorter radius would probably increase the number of captured muons. The study on the decay tunnel radius confirm this hypothesis, but unfortunatly, the pions space distribution (see figure 3.6) shows that reducing the radius of the decay tunnel their number in the decay tunnel also decreases dramatically, reducing the final intensity of the $\nu_\mu$ flux. The global analysis to optimize the decay tunnel dimensions have been performed systematically and will be shown in the next chapter.

# Chapter 4

# Neutrino flux calculations

Neutrino flux calculations for both pion and subsequent muon decays has been performed analytically instead of producing a Monte Carlo simulation. The small solid angle covered by the detector (area of 100 $m^2$ located at about 100 km from the target) reduces considerably the flux of neutrinos in it, hence to produce enough statistics it would be necessary to consider a large number of protons on target in the simulations.
The strategy chosen to compute neutrino fluxes is to consider each pion and muon individually, propagate it through the horn and the decay tunnel and then calculate the probability that neutrinos coming from it have to reach the detector. This probability is the composition of the probability distribution for the specific decay kinematics and the probability that the particle decay along its flight.
Neutrinos considered in this study are those coming from pion and muon decays. Pions are produced at the target and focused by the magnetic horn, muons are produced in the successive pion decay. With the considered Superbeam configuration the energy of the focused pion is in the range of a few hundreds of MeV. A lot of other neutrino producing phenomena appear in the interactions of pions and muons of the beam with the material of the apparatus. Pions interaction with decay tunnel walls give rise to pions of few tens of MeV and subsequent neutrinos; muons captured by the decay tunnel walls decay producing neutrinos. Other sources of neutrinos are the decays of other particles (e.g. neutrons) produced by the interaction of the proton beam with the target and from the proton beam dump. All these neutrinos are expected to have very low energy and to be produced quasi isotropically; their probability to enter the solid angle of the detector is reduced; they have

been neglected for this conceptual study.

## 4.1 Kinematics

Neutrino distribution per unit area is needed to compute fluxes. The decay processes studied are the two body pion decay and the three body muon decay. Neutrino masses (known to be less than few eV/c$^2$) are neglected throughout.

### 4.1.1 Two body decay

The $\pi^{\pm}$ decay is considered here:

$$\pi^{\pm} \rightarrow \mu^{\pm}\nu_{\mu}(\bar{\nu}_{\mu})$$

In the centre of mass frame, neglecting neutrino mass:

$$\begin{pmatrix} M \\ \vec{0} \end{pmatrix}_{\pi} = \begin{pmatrix} E^*_{\mu} \\ \vec{P}^* \end{pmatrix}_{\mu} + \begin{pmatrix} |\vec{P}^*| \\ -\vec{P}^* \end{pmatrix}_{\nu}$$

Applying the energy conservation law:

$$\begin{aligned} M &= E^*_{\mu} + |\vec{P}^*| \\ E^{*2}_{\mu} &= |\vec{P}^*|^2 + m^2_{\mu} \\ E^{*2}_{\mu} &= \left(M - |\vec{P}^*|\right)^2 = M^2 + |\vec{P}^*|^2 - 2M|\vec{P}^*| \end{aligned}$$

Hence,

$$|\vec{P}^*| = \frac{M^2 - m^2_{\mu}}{2M} \tag{4.1}$$

$$E^*_{\mu} = \frac{M^2 + m^2_{\mu}}{2M} \tag{4.2}$$

Introducing pion and muon masses

$$\begin{aligned} m_{\pi} &= 0.140\,(GeV) \\ m_{\mu} &= 0.106\,(GeV) \end{aligned}$$

muon energy and momentum are:

$$\begin{aligned} |\vec{P}^*| &= 0.030\,(GeV) \\ E^*_\mu &= 0.110\,(GeV) \end{aligned}$$

and neutrino energy and momentum are:

$$E^*_\nu \simeq |\vec{P}^*| = 0.030\,(GeV)$$

Pion decays isotropically in its centre of mass. That means the probability distribution $d\mathcal{P}/d\Omega$ to find a neutrino in a certain solid angle is constant.

$$\frac{d\mathcal{P}}{d\Omega} = \frac{d\mathcal{P}}{d\cos\theta^* d\varphi} = \frac{1}{4\pi} \tag{4.3}$$

In the laboratory frame the pion is moving with a velocity $\vec{\beta_\pi}$, so a Lorentz transformation has to be applied to the probability distribution. The effect of this transformation is to squeeze the trajectory angle $\theta^*$ of the emitted neutrino, along the pion direction of flight, producing a focusing effect.
Let K and K' be two coordinate systems moving with constant velocity $v$ with respect to each other. Let the direction of the axes of K and K' be parallel and such that the z and z' axes coincide and are parallel to the relative velocity, see figure (4.1) .
The Lorentz transformation of a four vector from K' to K [58] can be written as:

$$\vec{P} = \gamma\left(\vec{P'} + \vec{\beta}E'\right) \tag{4.4}$$

$$E = \gamma\left(E' + \vec{\beta}\cdot\vec{P'}\right) \tag{4.5}$$

where
$\beta = v/c$
$\gamma = \frac{1}{\sqrt{1-\beta^2}}$.
For simplicity let observe the modification of the emitted neutrino angle going from the pion rest frame to the laboratory frame, in two dimensions, with the pion momentum along the z-axis of the pion. Let $\theta^*$ and $P^*_\nu$ be the angle and the momentum of the emitted neutrino in the centre of mass of the pion and $\beta, \gamma$ the relativistic factors of the pion. $P^*_\nu$ can be decomposed in longitudinal and transverse component with respect to the pion frame.

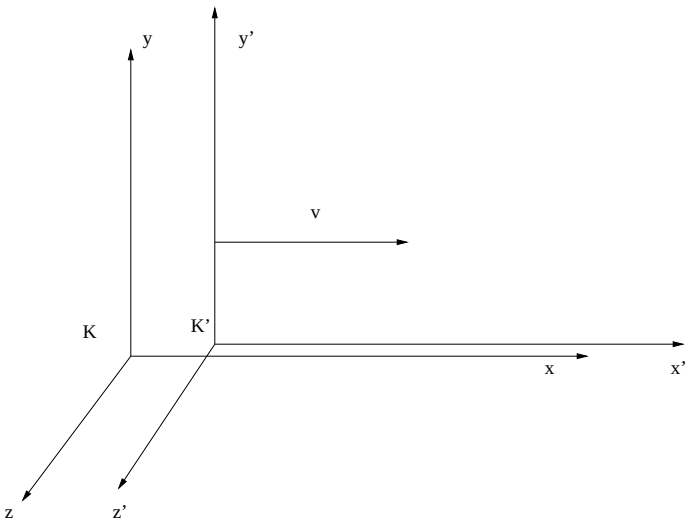


Figure 4.1: K K' frames.

$$P^*_{\nu T} = P^*_\nu \sin\theta^*$$

$$P^*_{\nu L} = P^*_\nu \cos\theta^*$$

The transverse component remains unchanged after the Lorentz transformation while the longitudinal one is dilated (see figure 4.2).

$$P_{\nu L} = \gamma \left(P^*_{\nu L} + \beta E^*_\nu\right)$$

$$P_{\nu T} = P^*_{\nu T}$$

$$E_\nu = \gamma \left(E^*_\nu + \beta P^*_{\nu L}\right)$$

Neglecting neutrino mass $E^*_\nu = P^*_\nu$, $E_\nu = P_\nu$

$$P_{\nu L} = \gamma P^*_\nu \left(\cos\theta^* + \beta\right)$$

$$P_{\nu L} = \vec{P_\nu} \cdot \vec{e_z} = E_\nu \cos\theta = \cos\theta \left(\gamma P^*_\nu \left(1 + \beta\cos\theta^*\right)\right).$$

Hence the transformation formula from pion rest frame to the laboratory frame of the neutrino angle is:

$$\cos\theta = \frac{\beta + \cos\theta^*}{1 + \beta\cos\theta^*}, \tag{4.6}$$

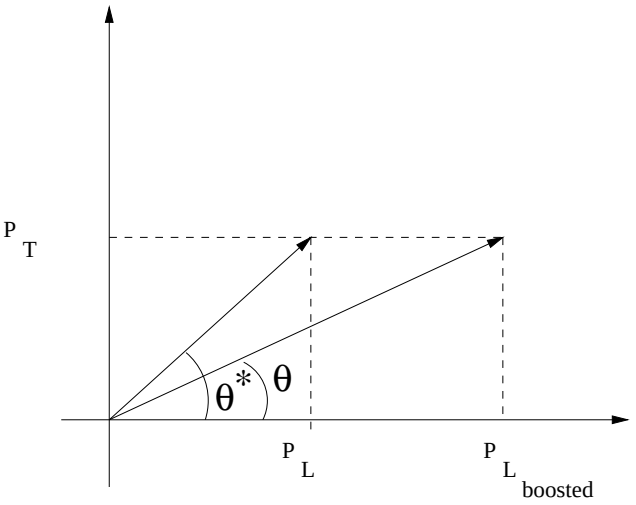


Figure 4.2: Lorentz boost

and the inverse one:

$$\cos\theta^* = \frac{\beta - \cos\theta}{\beta\cos\theta - 1}. \tag{4.7}$$

The probability that a neutrino, with angle $\theta^*$ in the pion rest frame, reach the detector can be calculated using (4.7) and integrating (4.3).

Consider now the situation illustrated in figure (4.3) where the pion is produced at an angle $\theta$ with respect to the $\hat{e}_z$ axis.
It is assumed that the proton beam and the decay tunnel are in line with the detector and the target, hence the cylindrical symmetry of the problem can be used. With the right choice of the coordinates system, the 3 dimensional problem is reduced to a simpler 2 dimensional one. The choice of the axes for the laboratory frame $(\hat{e}_x, \hat{e}_y, \hat{e}_z)$ and the pion frame $(\hat{u}_x, \hat{u}_y, \hat{u}_z)$ is such that:

- the decay tunnel - detector axis correspond to the the z axis of the laboratory frame $(\hat{e}_z)$;
- the z axis of the pion rest frame $(\hat{u}_z)$ is along its momentum $\hat{u}_z = \vec{P}_\pi/|\vec{P}_\pi|$;

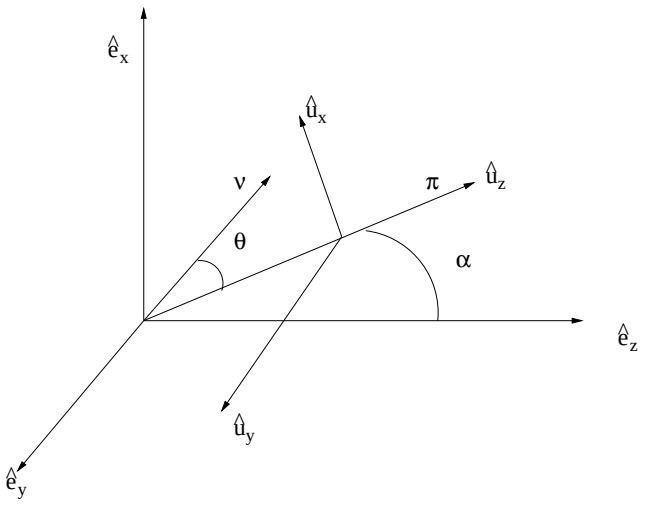


Figure 4.3: Pion $(\hat{u}_x, \hat{u}_y, \hat{u}_z)$ and laboratory $(\hat{e}_x, \hat{e}_y, \hat{e}_z)$ frames

- the y axis of the pion rest frame $(\hat{u}_y)$ coincides with the y axis of the laboratory frame $(\hat{e}_y)$ if $\hat{u}_y = \hat{e}_y = \hat{e}_z \times \hat{u}_z$;

- the x axis of the laboratory frame is $\hat{e}_x = \hat{e}_y \times \hat{e}_z$;

- the x axis of the pion rest frame is $\hat{u}_x = \hat{u}_y \times \hat{u}_z$;

The angles $\theta^*$ in the centre of mass of the pion are measured with respect to the pion $\hat{u}_z$ axis and the angles $\theta$ in the laboratory frame are measured with respect to the $\hat{e}_z$ axis.
The angle $\varphi$, due to the choice of the $\hat{u}_y, \hat{e}_y$ axes, coincides in the two frames.
The tunnel decay lengths and radii are always considered negligible with respect to the target detector distance. Decay tunnels of 5 m to 50 m length and 0.25 m to 1 m radius have been considered while the distance to the detector is about 100 km. Hence the decay tunnel is considered point-like and, concerning the solid angle seen by the particles, there is no difference between pion production position and muon decay position.
From figure (4.3) it is clear that, to reach the detector (far away along the $\hat{e}_z$), the neutrino has to be emitted along the $\hat{e}_z$ axis, i.e. $\theta$ must be equal to $\alpha$ and $\varphi = \pi$.
To calculate the number of neutrinos reaching the detector, the probability

density (4.3) in the laboratory frame is required.

$$\frac{d\mathcal{P}}{d\Omega} = \frac{d\mathcal{P}}{d\Omega^*}\frac{d\Omega^*}{d\Omega} = \frac{1}{4\pi}\frac{d\Omega^*}{d\Omega}$$

To change the solid angle element from the pion frame to the laboratory frame, the Jacobian of the transformation has to be calculated.

$$d\cos\theta^* d\varphi^* = \frac{\partial(\cos\theta^*, \varphi^*)}{\partial(\cos\theta, \varphi)} d\cos\theta d\varphi$$

$$\frac{\partial(\cos\theta^*, \varphi^*)}{\partial(\cos\theta, \varphi)} = \begin{vmatrix} \frac{\partial\cos\theta^*}{\partial\cos\theta} & \frac{\partial\varphi^*}{\partial\cos\theta} \\ \frac{\partial\cos\theta^*}{\partial\varphi} & \frac{\partial\varphi^*}{\partial\varphi} \end{vmatrix} = \frac{\partial\cos\theta^*}{\partial\cos\theta}$$

because off-diagonal terms are zero and $\varphi = \varphi^*$.
Using (4.7):

$$\frac{d\cos\theta^*}{d\cos\alpha} = \left(\frac{1}{-\sin\alpha}\right)\frac{d}{d\alpha}\left[\frac{\beta - \cos\alpha}{\beta\cos\alpha - 1}\right] = \frac{1-\beta^2}{(\beta\cos\alpha - 1)^2}$$

(as explained above the angle $\theta$ has to be equal to $\alpha$), hence the density probability with the solid angle expressed in the laboratory frame is

$$\frac{d\mathcal{P}}{d\Omega} = \frac{1}{4\pi}\frac{d\cos\theta^*}{d\cos\alpha} = \frac{1}{4\pi}\frac{1-\beta^2}{(\beta\cos\alpha - 1)^2}$$

Finally the probability density per unit area:

$$\frac{d\mathcal{P}}{ds} = \frac{1}{4\pi L^2}\frac{1-\beta^2}{(\beta\cos\alpha - 1)^2} \tag{4.8}$$

Due to the smallness of the solid angle covered by the detector, the probability density is considered constant on the detector area and so it is possible to obtain the integrated probability simply multiplying it times the detector area A:

$$\mathcal{P} = \mathcal{P}(\alpha, \beta) = \frac{1}{4\pi}\frac{A}{L^2}\frac{1-\beta^2}{(\beta\cos\alpha - 1)^2} \tag{4.9}$$

### 4.1.2 Three body decay

The considered three body decay is

$$\mu^{\pm} \rightarrow e^{\pm}\nu_e(\bar{\nu}_e)\,\bar{\nu}_\mu(\nu_\mu)$$

In the two body decay the energy and momentum of the produced particle have fixed values. In the three body decay the energy and momentum assume a continuous distribution. The probability distribution to find a neutrino in a certain solid angle with a certain fraction $x$ of the centre of mass energy is [59]

$$\frac{d\mathcal{P}}{dx d\Omega^*} = \frac{1}{4\pi}\left[f_0(x) \mp \Pi_\mu f_1(x)\cos\theta^*\right]$$

where:

- $d\Omega^*$ is the solid angle in the muon rest frame;
- $x = 2E^*_\nu/m_\mu$ is the fraction of the centre of mass energy taken by the neutrino;
- $E^*_\nu$ is the neutrino energy in the muon rest frame;
- $\Pi_\mu$ is the muon polarization in the muon rest frame along the muon direction;
- $\theta^*$ is the angle between the neutrino momentum vector and the muon direction (in the muon rest frame);
- $m_\mu$ is the muon mass;

The functions $f_0(x), f_1(x)$ are given in table (4.1)
The energy spectra of the emitted particles are shown in figure (4.4)

| | $f_0(x)$ | $f_1(x)$ |
|---|---|---|
| $\nu_\mu, e$ | $2x^2(3-2x)$ | $2x^2(1-2x)$ |
| $\nu_e$ | $12x^2(1-x)$ | $12x^2(1-x)$ |

Table 4.1: Flux functions in the muon rest frame

In the muon rest frame frame it is easy to express this distribution as a

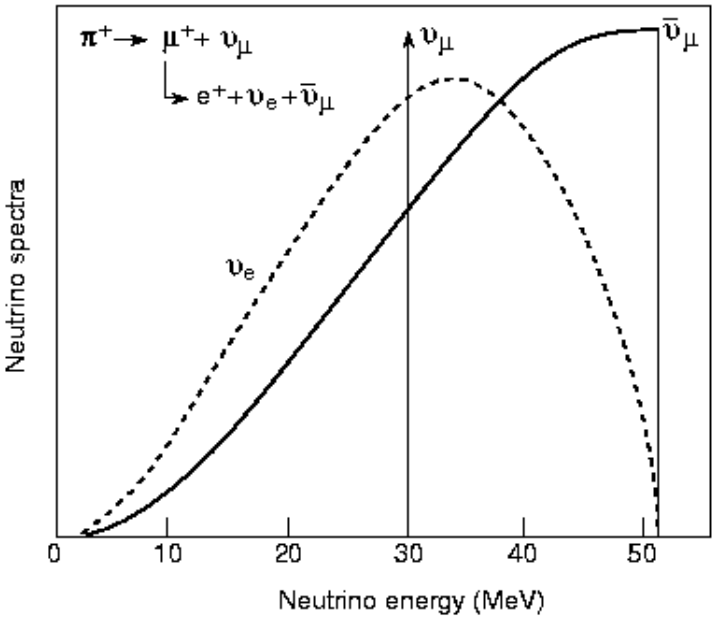


Figure 4.4: Neutrino energy spectra from $\pi^+$ and $\mu^+$ decay in the rest frames

function of the neutrino energy.

$$x = \frac{2E_\nu^*}{m_\mu} \qquad dx = \frac{2dE_\nu^*}{m_\mu}$$

$$\frac{d\mathcal{P}}{dE_\nu^* d\Omega^*} = \frac{1}{4\pi}\frac{2}{m_\mu}\left[f_0(E_\nu^*) \mp \Pi_\mu f_1(E_\nu^*)\cos\theta^*\right]$$

To calculate neutrino fluxes, the probability distribution in the laboratory frame is needed. In this case two Lorentz transformations are necessary to go from the muon rest frame to the laboratory frame. Neutrinos coming from muon are boosted along the muon trajectory but muon itself is boosted along the pion trajectory in laboratory frame.
This procedure can be simplified if the neutrino boosted along the muon trajectory in the laboratory frame is considered directly. To do this the muon in the pion rest frame is first considered. As seen in the previous section it has a fixed energy and momentum. To transform energy and momentum of the muon to the laboratory frame it is necessary to boost it along the pion

trajectory considering the angle $\theta^*$ at which it is emitted from the pion. The muon energy and momentum in the laboratory frame depends on that angle. Considering the pion trajectory as the longitudinal axis:

$$P^*_{\mu T} = P^*_\mu \sin\theta^*_\mu$$

$$P^*_{\mu L} = P^*_\mu \cos\theta^*_\mu$$

The transverse component remain unchanged after the Lorentz transformation while the longitudinal one is dilated, applying (4.4):

$$P_{\mu L} = \gamma_\pi \left(P^*_{\mu L} + \beta_\pi E^*_\mu\right)$$

$$P_{\mu T} = P^*_{\mu T}$$

Finally for the energy in the laboratory frame is possible to use (4.5):

$$E_\mu = \gamma_\pi \left(E^*_\mu + \beta_\pi P^*_{\mu L}\right)$$

Once the muon momentum and energy in the laboratory frame is known it is possible to consider neutrinos coming from its decay. The solid angle covered by the detector viewed from the muon rest frame has to be transformed in the solid angle viewed from the target in the laboratory frame. Thanks to the point-like approximation of the decay tunnel it is possible to consider the muon exactly in the origin of the laboratory frame. The two coordinates systems, $(\hat{e}_x, \hat{e}_y, \hat{e}_z)$ for the laboratory and $(\hat{v}_x, \hat{v}_y, \hat{v}_z)$ for the muon, are identical to those considered in the previous section for the pions:

- the decay tunnel - detector axis correspond to the the z axis of the laboratory frame $(\hat{e}_z)$;
- the z axis of the muon frame $(\hat{v}_z)$ is along the its momentum $\hat{v}_z = \vec{P}_\mu/|\vec{P}_\mu|$;
- the y axis of the muon frame $(\hat{v}_y)$ coincides with the y axis of the laboratory frame $(\hat{e}_y)$ if $\hat{v}_y = \hat{e}_y = \hat{e}_z \times \hat{v}_z$ it is considered;
- the x axis of the laboratory frame is $\hat{e}_x = \hat{e}_y \times \hat{e}_z$;
- the x axis of the muon frame is $\hat{v}_x = \hat{v}_y \times \hat{v}_z$;

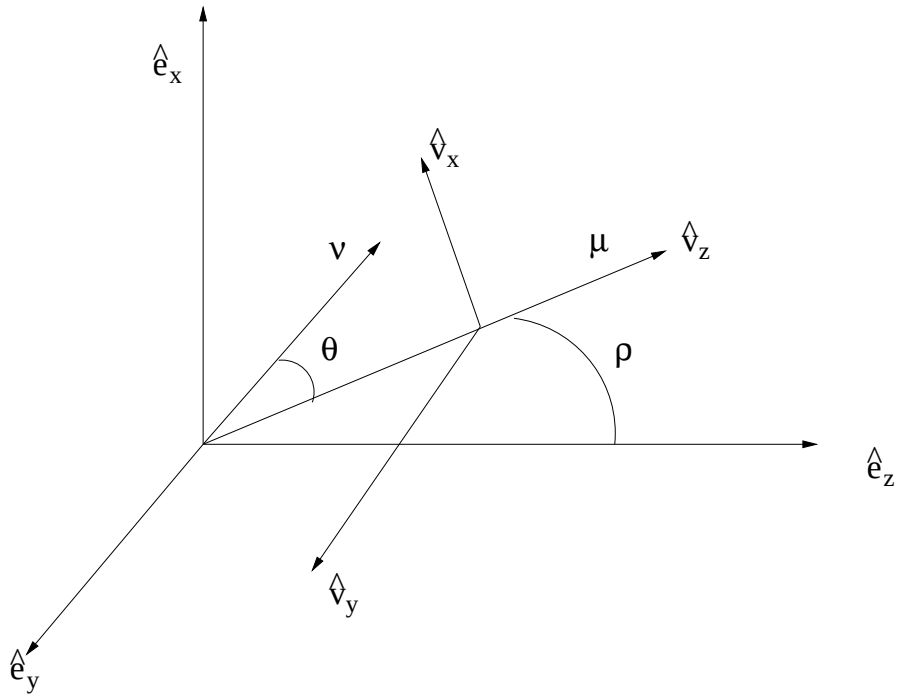


Figure 4.5: Muon $(\hat{v}_x, \hat{v}_y, \hat{v}_z)$ and laboratory $(\hat{e}_x, \hat{e}_y, \hat{e}_z)$ frames

The angles $\theta^*$ in the centre of mass of the muon are measured with respect to the muon $\hat{v}_z$ axis and the angles $\theta$ in the laboratory frame are measured with respect to the $\hat{e}_z$ axis.
The angle $\varphi$, due to the choice of the $\hat{v}_y, \hat{e}_y$ axes, coincides in the two frames.
To boost neutrinos in the laboratory frame it is possible to follow exactly the same argument used for neutrinos from pion decay.
The momentum of the neutrino in the laboratory frame is

$$P_{\nu T} = P^*_{\nu T} = P^*_\nu \sin\theta^*$$

$$P^*_{\nu L} = P^*_\nu \cos\theta^*$$

$$P_{\nu L} = \gamma_\mu \left(P^*_{\nu L} + \beta_\mu E^*_\nu\right)$$

$$P_{\nu T} = P^*_{\nu T}$$

while the energy is

$$E_\nu = \gamma_\mu \left(E^*_\nu + \beta_\mu P^*_{\nu L}\right) \tag{4.10}$$

The same relation is found for the angle transformation from the muon centre of mass to the laboratory:

$$\cos\theta = \frac{\beta_\mu + \cos\theta^*}{1 + \beta_\mu \cos\theta^*}, \tag{4.11}$$

and the inverse one:

$$\cos\theta^* = \frac{\beta_\mu - \cos\theta}{\beta_\mu \cos\theta - 1}. \tag{4.12}$$

To write the probability distribution in the laboratory frame it is necessary to write the solid angle element and the energy of the neutrino in that frame.

$$\frac{d\mathcal{P}}{dE_\nu d\Omega} = \frac{d\mathcal{P}}{dE_\nu^* d\Omega^*}\frac{dE_\nu^* d\Omega^*}{dE_\nu d\Omega}$$

For the solid angle the argument used is the same as in the pion decay:

$$d\cos\theta^* d\varphi^* = \frac{\partial(\cos\theta^*, \varphi^*)}{\partial(\cos\theta, \varphi)} d\cos\theta d\varphi$$

$$\frac{\partial(\cos\theta^*, \varphi^*)}{\partial(\cos\theta, \varphi)} = \frac{\partial\cos\theta^*}{\partial\cos\theta}$$

$$\frac{\partial\cos\theta^*}{\partial\cos\theta} = \frac{1-\beta_\mu^2}{(\beta_\mu\cos\theta - 1)^2} = \frac{1-\beta_\mu^2}{(\beta_\mu\cos\rho - 1)^2}$$

As shown in figure (4.5), neutrinos must have a trajectory angle $\theta$ in the laboratory frame equal to the angle $\rho$ of the muon in the same frame, to reach the detector.
The energy of the neutrino is simply written from (4.10) as

$$E_\nu = \gamma_\mu E_\nu^* (1 + \beta_\mu \cos\theta^*)$$

$$E_\nu^* = \frac{E_\nu}{\gamma_\mu (1 + \beta_\mu \cos\theta^*)}$$

hence,

$$dE_\nu^* = \frac{dE_\nu}{\gamma_\mu (1 + \beta_\mu \cos\theta^*)}$$

The probability distribution in the laboratory frame is finally:

$$\frac{d\mathcal{P}}{dE_\nu d\Omega} = \frac{1}{4\pi}\frac{2}{m_\mu}\frac{1}{\gamma_\mu (1 + \beta_\mu\cos\theta^*)}\frac{1-\beta_\mu^2}{(\beta_\mu\cos\rho - 1)^2}\left[f_0(E_\nu) \mp \Pi_\mu f_1(E_\nu)\cos\theta^*\right] \tag{4.13}$$

The above expression gives the probability distribution as a function of the neutrino energy in the laboratory frame, the decay angle $\theta^*$ of the $\nu_e(\bar{\nu}_\mu)$ in the muon rest frame and the polarization of the $\mu$ in the same frame.
Use this formula to perform fluxes calculation is not straightforward. From the pion production simulations it is possible to obtain $\beta_\pi$ in the laboratory frame. In the two body decay the emitted neutrino is characterized only by one significant angle $\theta^*$. Thus, the only way for this neutrino to reach the detector is to have an angle $\theta$ in the laboratory frame equal to the angle $\alpha$ between the pion direction of flight and the $\hat{e}_z$ axis as shown in figure (4.3). Using the formula (4.9) it is straightforward to calculate the probability that neutrinos have to reach the detector and to count it like a weight. In the three body decay the neutrino is characterized by four significant variables: the angles $(\theta^*_\mu, \varphi^*_\mu)$ of the muon direction in the pion rest frame and the angles $(\theta^*, \varphi^*)$ of the neutrino direction in the muon rest frame.
Only a well defined pair of directions $(\theta^*_\mu, \varphi^*_\mu)$, $(\theta^*, \varphi^*)$, allows the neutrino to reach the detector. As will be explained in the next section, a computer program has to be implemented to find all the possible pairs and, using (4.13), calculate and sum the probabilities. This is equivalent but more precise than a sampling integration.
Muons are spin 1/2 particles and this affect the final spectrum of emitted neutrinos, hence one has to discuss the polarization $\Pi_\mu$ of the muon produced in pion decay.
Muon polarization is usually described in terms of helicity which is defined

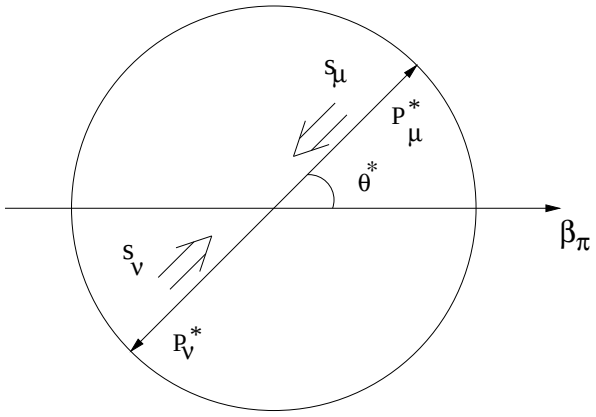


Figure 4.6: Pion decay in its rest frame

to be the projection of the spin vector $\vec{s}$ in the muon rest frame along its

momentum direction $\vec{p}/|\vec{p}|$.

$$h = \frac{\vec{p} \cdot \vec{s}}{|\vec{p}|}$$

In the pion rest frame (figure (4.6)) muon and neutrino are emitted with collinear momenta, equal in magnitude but opposite in direction. The neutrino (antineutrino) helicity has a fixed value of -1 (+1) (neutrino masses are neglected) and the conservation of the angular momentum implies that the positive (negative) muon is completely polarized longitudinally in the pion rest frame with helicity -1 (+1). A Lorentz transformation in the direction of the muon velocity does not change the component of its spin in this direction and so the muon is also completely polarized in its rest frame. However, in the transformation of the muon into the laboratory frame, an angle develops between the transformed muon momentum and its spin in the rest frame. As a result the magnitude of the polarization in the laboratory frame is generally less than 1.

To define the transverse and longitudinal polarization, one uses the normal definition relative to the muon laboratory direction in the laboratory, as viewed in the muon rest frame [60].

For simplicity assume a pion flying along $\hat{e}_z$. In the muon frame the pion

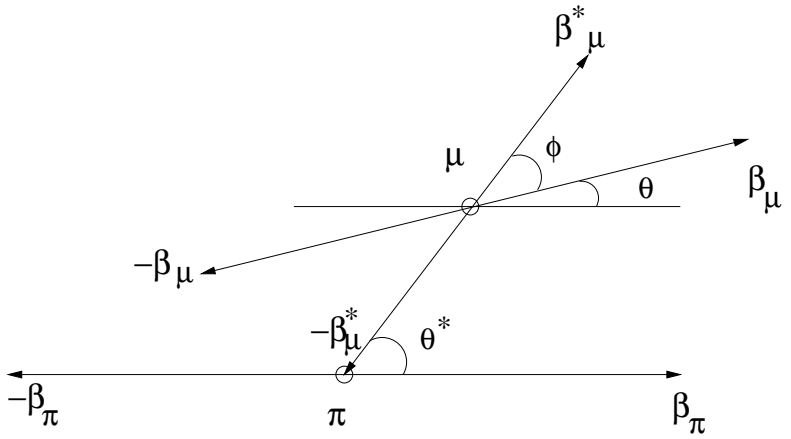


Figure 4.7: Pion and muon decay seen from the muon.

rest frame moves with a velocity $-p^*_\mu/E^*_\mu = -\beta^*_\mu$ (see figure (4.7)). In the pion rest frame the laboratory appears to move to the left with velocity $-\beta_\pi$, while on transforming to the muon rest frame this direction is rotated towards the pion - muon relative velocity and becomes $-\beta_\mu$.

In any Lorentz transformation the transverse component of the velocity four-vector $\gamma(1,\beta)$ is conserved [58], and for this particular case

$$\gamma_\pi \beta_\pi \sin\theta^* = \gamma_\mu \beta_\mu \sin\phi$$

The transverse polarization is then defined as

$$\Pi_\mu^T = \sin\phi = \frac{\gamma_\pi \beta_\pi}{\gamma_\mu \beta_\mu} \sin\theta^*$$

The longitudinal polarization is needed in the probability distribution. The modulus of this angle is simply

$$\Pi_\mu^L = \cos\phi = \sqrt{1 - \Pi_\mu^{T2}}$$

The sign of this angle can be calculated observing that it changes when $\sin\phi = 1$. Imposing $\sin\phi = 1$ it is possible to calculate the correspondent limit condition $\cos\theta^*$:

$$\cos\theta^* = -\frac{P_\mu^*}{\beta_\pi E_\mu^*}$$

Figure (4.8) shows the variation of the averaged muon helicity in the laboratory frame as a function of the pion momentum.
Now all the ingredients are ready for the integration.
The probability can be written per unit area:

$$\frac{d\mathcal{P}}{dE_\nu ds} = \frac{d\mathcal{P}}{dE_\nu L^2 d\Omega}$$

As in the previous section the solid angle covered by the detector is very small and so the distribution can be considered constant on it. The integration can be simply performed multiplying the probability density times the detector area:

$$\frac{d\mathcal{P}}{dE_\nu} = \frac{1}{4\pi}\frac{A}{L^2}\frac{2}{m_\mu}\frac{1}{\gamma_\mu\left(1+\beta_\mu\cos\theta^*\right)}\frac{1-\beta_\mu^2}{\left(\beta_\mu\cos\rho - 1\right)^2}\left[f_0(E_\nu) \mp \Pi_\mu f_1(E_\nu)\cos\theta^*\right] \tag{4.14}$$

The last integration is in $dE_\nu$

$$\mathcal{P}(\beta_\mu,\rho) = \int_0^{E_\mu} d\mathcal{P}(\beta_\mu,\rho,E_\nu)dE_\nu \tag{4.15}$$

and is calculated numerically.

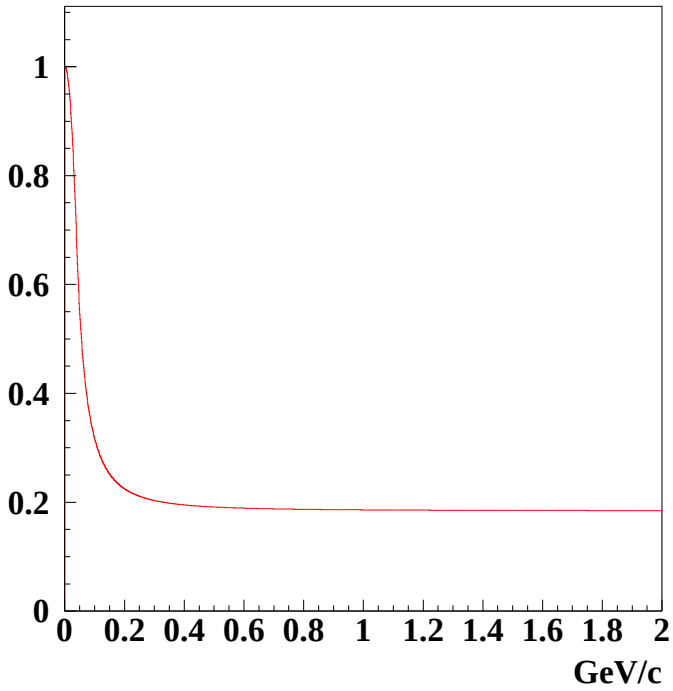


Figure 4.8: Magnitude of the averaged muon helicity in the laboratory frame as a function of pion momentum.

## 4.2 Flux computation

To calculate neutrino fluxes a Fortran77 program shown in Appendix A has been produced. In this section a brief explanation of the technique used is given.
Numbers handled in this calculations ranges from $10^{-22}$ to $10^{20}$. The Fortran77 real type [61] can manage values in the range from around $10^{-38}$ to just over $10^{38}$, so this data type can fit this necessity. The problem is the precision allowed by the computer where the program run. Usually, for a real data type, a word of 32 bits is allocated. This gives precision over 7 decimal digits. In the calculation of the integral probability it is necessary to sum several numbers around $10^{-20}$. Due to the limited precision of the machine, numbers that differ from each other after the seventh decimal digit (frequent case with these probability density), are considered equal, and

summed several times, give rise to unpleasant nonsense. Many checks have been performed on the inaccuracy introduced by the number representation and finally the suitable data type has been found to be the double precision. Neutrino energy range is from 0 up to 2 GeV. The resolution chosen for neutrino energy is 20 MeV/bin. That means the range is divided into 100 bins. The program receive as input MARS files of the target-horn simulation (the typical size of this file is tens of Mbyte). In this file are contained data of the particles surviving after the horn.
The format of this file is:

Event, particle id, x, y, z, px, py, pz, et ,ctoff, w

where:

| | |
|---|---|
| Event | event number in the simulation |
| particle id | 3=$\pi^+$ 4=$\pi^-$ 7=$\mu^+$ 8=$\mu^-$ |
| x, y, z | coordinate in cm |
| px, py, pz | momentum in GeV/c |
| et | total energy in GeV |
| ctoff | c×(time of flight) in cm |
| w | statistical weight |

For the pion decay all the values used in the probability formula (4.9) can be calculated with data read from the input file; once the value of the probability to emit a neutrino that reach the detector has been calculated, it is necessary to multiply it times the probability that the pion has to decay along the path between the end of the horn and the absorption point in the tunnel walls.
A similar procedure has been followed for muons, produced in pion decay. In the program these have been generated scanning the whole solid angle in bins of $\cos\theta^*$ and $\varphi^*$. Then for each of them the integral (4.15) has been calculated.
These probabilities are summed and stored in an array (as a weight) in the right energy bin. In this way six arrays are created: $\nu_\mu$, $\bar{\nu}_\mu$ from pions, $\nu_e$, $\bar{\nu}_\mu$, $\bar{\nu}_e$, $\nu_\mu$ from muons.
To transform these probabilities in the number of neutrinos reaching the detector it is necessary to multiply it times the right normalization. This factor contains the information that input files are created considering $10^6$ protons on target. For simplicity, neutrino fluxes are calculated for one year of SPL

run (1 year=$10^7$s) . The normalization factor is then:

$$\frac{number\,of\,neutrinos\,(bin_i)}{year} = weight\,(bin_i)\frac{1}{10^6\,(protons)}10^{16}\frac{protons}{s}10^7\frac{s}{year}$$

The output of this program consists of a file containing neutrino spectra with the format:

ie, E, nmp, anmp, ne, am, ae, nm

where:

| | |
|---|---|
| ie | energy bin number |
| E | energy upper limit of the bin |
| nmp | number of $\nu_\mu$ coming from $\pi^+$ decay in the bin$_{ie}$ |
| anmp | number of $\bar{\nu}_\mu$ coming from $\pi^-$ decay in the bin$_{ie}$ |
| ne | number of $\nu_e$ coming from $\mu^+$ decay in the bin$_{ie}$ |
| am | number of $\bar{\nu}_\mu$ coming from $\mu^+$ decay in the bin$_{ie}$ |
| ae | number of $\bar{\nu}_e$ coming from $\mu^-$ decay in the bin$_{ie}$ |
| nm | number of $\nu_\mu$ coming from $\mu^-$ decay in the bin$_{ie}$ |

## 4.3 Decay tunnel optimization

As seen in the previous chapter the geometry of the decay tunnel is the only way to act upon the superbeam purity. The problem is to find the right compromise between high purity and enough signal into the detector. In fact high purity is achieved with severe cuts in the pion beam, which means a reduction for both signal and background.
The best decay tunnel configuration has been systematically studied for the two polarities of the horn, i.e. focusing $\pi^+$ and focusing $\pi^-$. Fluxes for different lengths and radii have been computed.

## 4.4 Neutrino flux

The influence of the decay tunnel geometry on the fluxes purity has been analyzed in the third chapter. In this section all the generated fluxes for the two current polarities of the horn has been collected. Decay tunnel lengths from 5 meters to 50 meters have been chosen. It is possible to observe that after 30 40 meters fluxes don't increase anymore reaching a sort of saturation. This means that almost all pions (muons) have decayed. The decay tunnel length also acts on the peak position of the superbeam distribution;

the shorter the decay tunnel the lower the energy of the spectrum peak, because only low energy particles had enough time to decay. Radii have been considered from 25 cm to 100 cm, where the largest radius corresponds to the magnetic horn outer radius.
To generate these fluxes a detector of 1 kton at 130 km has been considered. The value of 1 kton for the mass has been chosen because it is easy to rescale to other detectors. The distance, as will be explained in the next chapter, is equal to the distance from the decay tunnel located at CERN and the detector site considered at LSM (Modane).
Tables (4.2), (4.3) summarize the ratios between the integrated $\nu_e$ and $\nu_\mu$ fluxes with the magnetic horn focusing $\pi^+$ and the ratios between the integrated $\bar{\nu}_e$ and $\bar{\nu}_\mu$ fluxes with the magnetic horn focusing $\pi^-$
The final geometry of the decay tunnel requires to strike into compromise between the minimal contamination of the superbeam (which would require the smallest decay tunnel) and the maximal flux into the detector (which on the other hand requires the biggest decay tunnel).
A decay length of 20 m and 1 m radius has been found, for both polarities of the magnetic horn to be the right compromise.
For completeness, figures (4.9)-(4.14) show the superbeam energy distribution for the various configuration studied with a magnetic horn focusing $\pi^+$ and (4.15)-(4.20) with a magnetic horn focusing $\pi^-$.

| Lenght/Radius | 25 (cm) | 50 (cm) | 75 (cm) | 100 (cm) |
|---|---|---|---|---|
| 5(m) | 0.86 | 1.12 | 1.27 | 1.38 |
| 10(m) | 1.26 | 1.76 | 2.07 | 2.28 |
| 20(m) | 1.65 | 2.53 | 3.12 | 3.56 |
| 30(m) | 1.8 | 2.98 | 3.80 | 4.44 |
| 40(m) | 1.91 | 3.27 | 4.27 | 5.07 |
| 50(m) | 1.96 | 3.45 | 4.6 | 5.54 |

Table 4.2: Integrated fluxes $\nu_e/\nu_\mu$, focusing $\pi^+$, in fraction per 1000.

| Lenght/Radius | 25 (cm) | 50 (cm) | 75 (cm) | 100 (cm) |
|---|---|---|---|---|
| 5(m) | 0.91 | 1.24 | 1.45 | 1.60 |
| 10(m) | 1.30 | 1.90 | 2.27 | 2.54 |
| 20(m) | 1.67 | 2.65 | 3.32 | 3.82 |
| 30(m) | 1.82 | 3.08 | 3.98 | 4.69 |
| 40(m) | 1.90 | 3.34 | 4.43 | 5.3 |
| 50(m) | 1.95 | 3.51 | 4.74 | 5.75 |

Table 4.3: Integrated fluxes $\bar{\nu}_e/\bar{\nu}_\mu$, focusing $\pi^+$, in fraction per 1000.

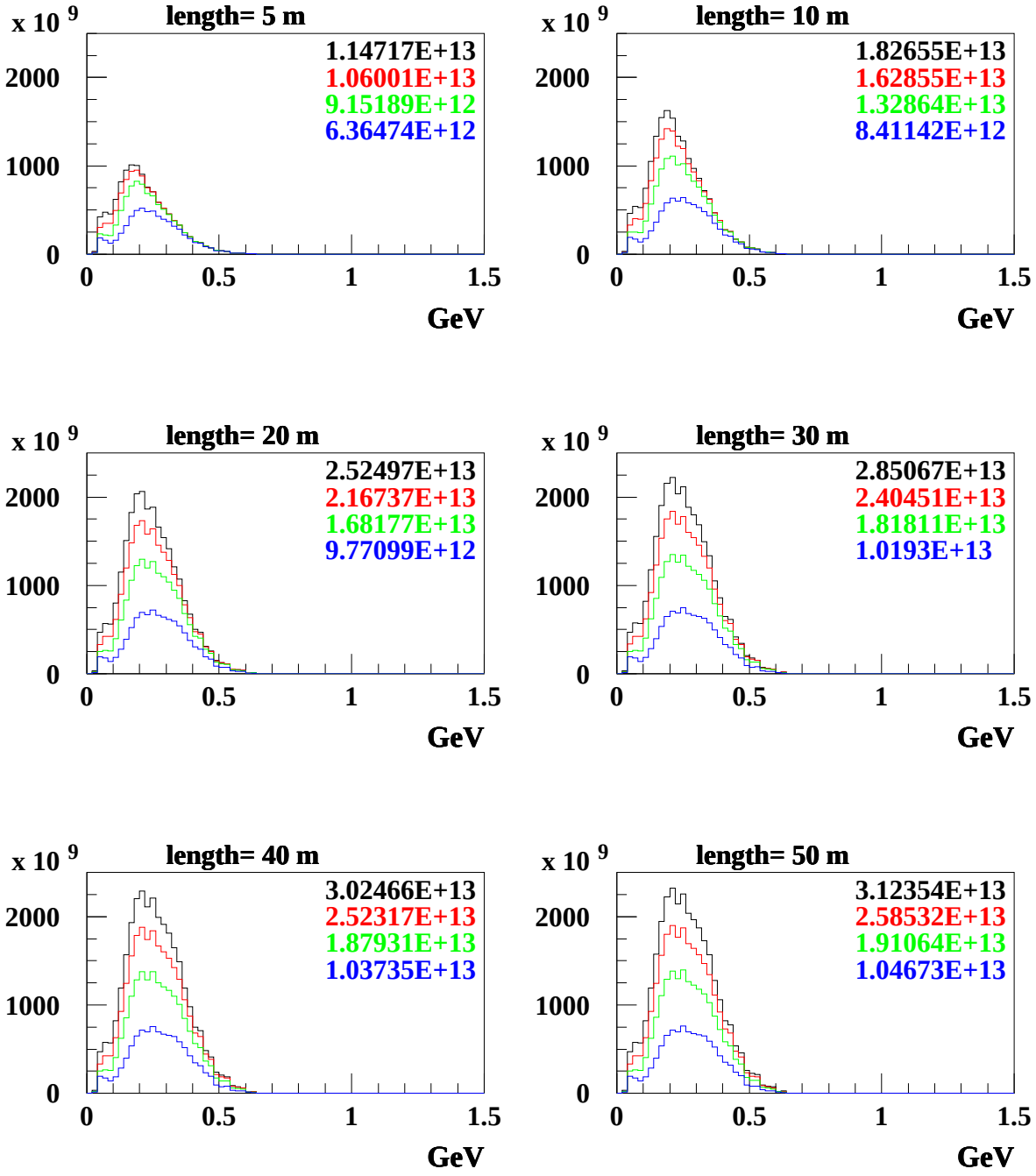


Figure 4.9: $\nu_\mu$ fluxes from $\pi^+ \to \mu^+\nu_\mu$, focusing $\pi^+$. Numbers are integrated fluxes. In black radius = 100 cm, in red radius = 75 cm, in green radius = 50 cm, in blue radius = 25 cm

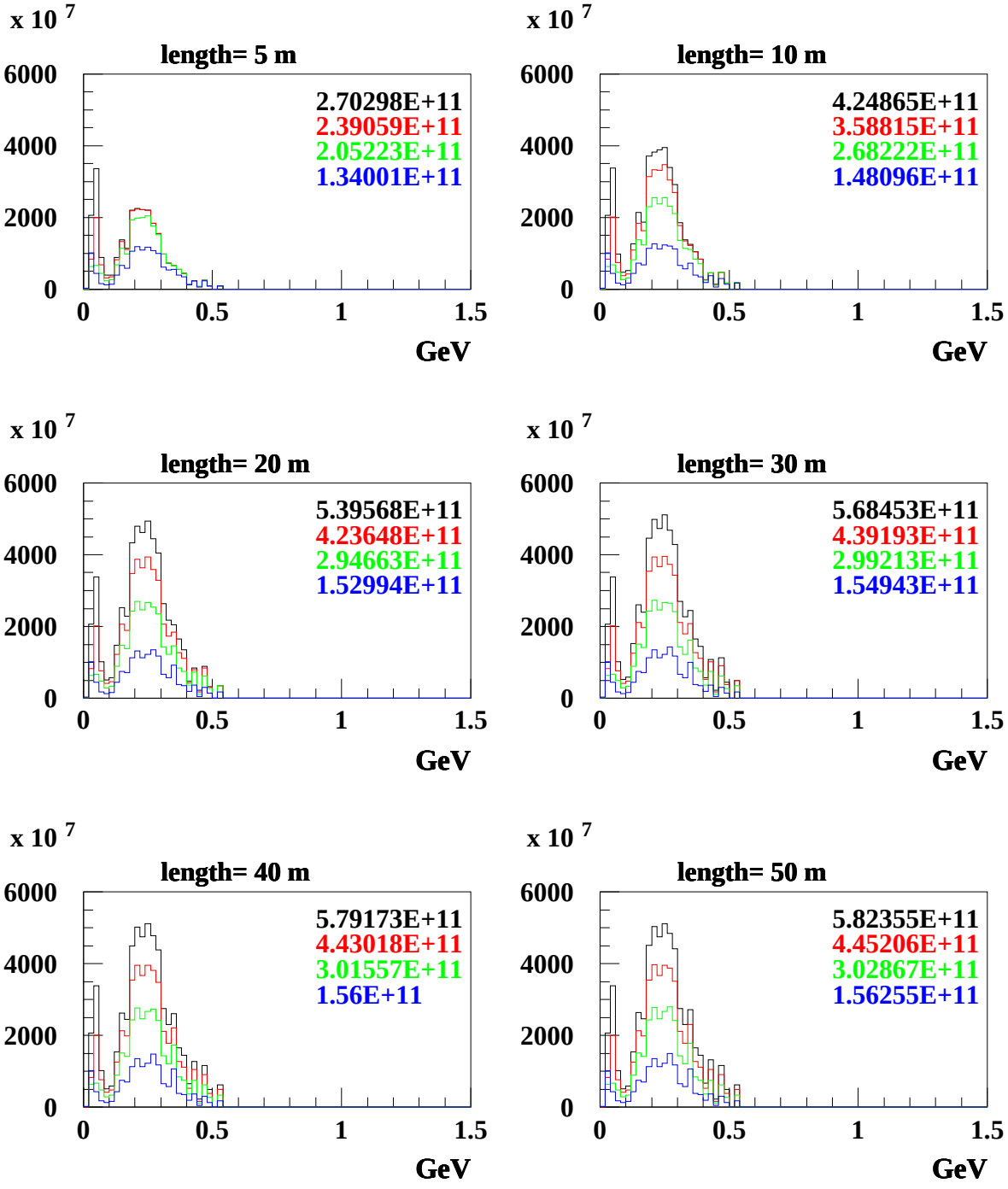


Figure 4.10: $\bar{\nu}_\mu$ fluxes from $\pi^- \rightarrow \mu^- \bar{\nu}_\mu$, focusing $\pi^+$. Numbers are integrated fluxes. In black radius = 100 cm, in red radius = 75 cm, in green radius = 50 cm, in blue radius = 25 cm

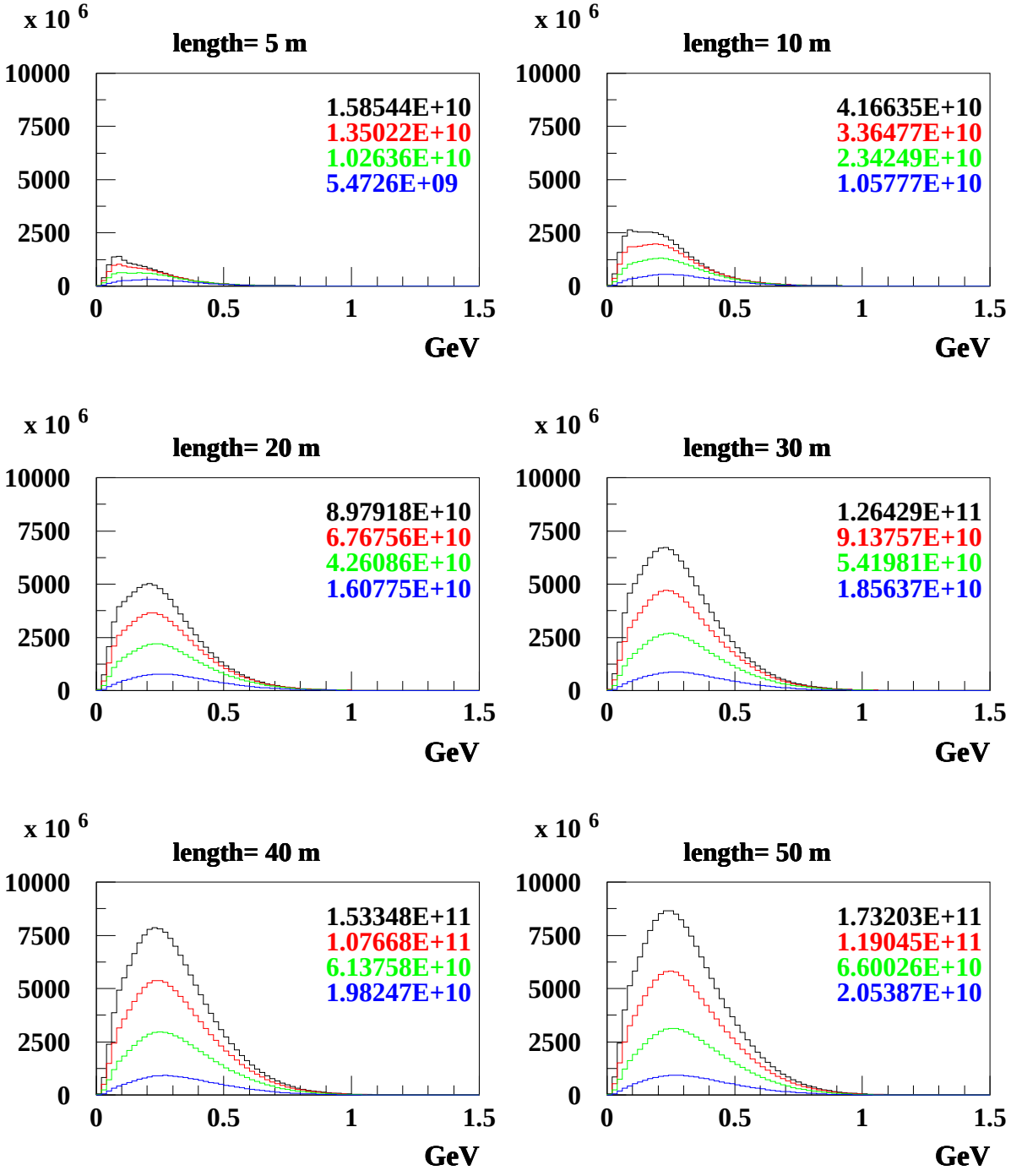


Figure 4.11: $\nu_e$ fluxes from $\mu^+ \to e^+\nu_e\bar{\nu}_\mu$, focusing $\pi^+$. Numbers are integrated fluxes. In black radius = 100 cm, in red radius = 75 cm, in green radius = 50 cm, in blue radius = 25 cm

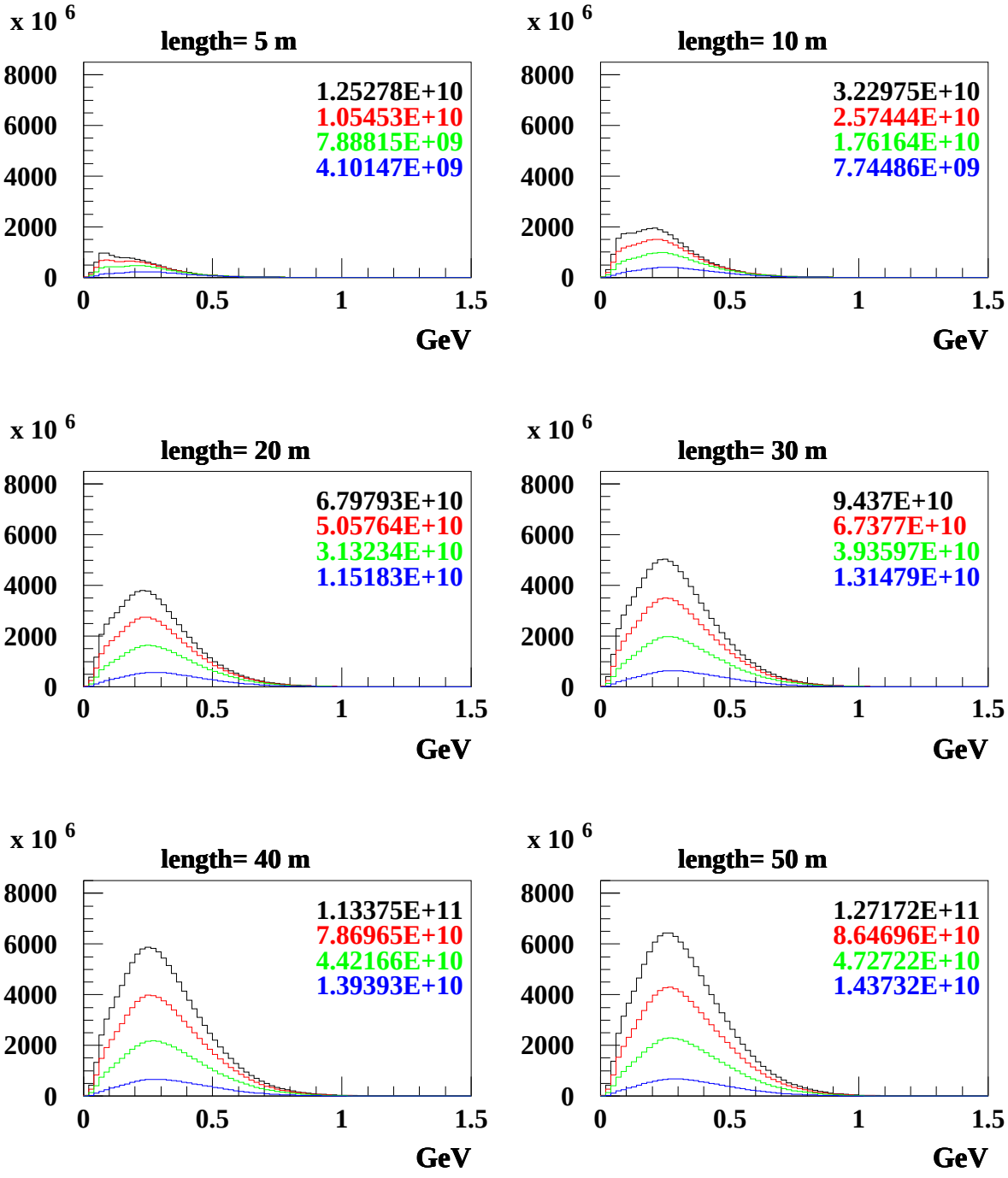


Figure 4.12: $\bar{\nu}_\mu$ fluxes from $\mu^+ \rightarrow e^+\nu_e\bar{\nu}_\mu$, focusing $\pi^+$. Numbers are integrated fluxes. In black radius = 100 cm, in red radius = 75 cm, in green radius = 50 cm, in blue radius = 25 cm

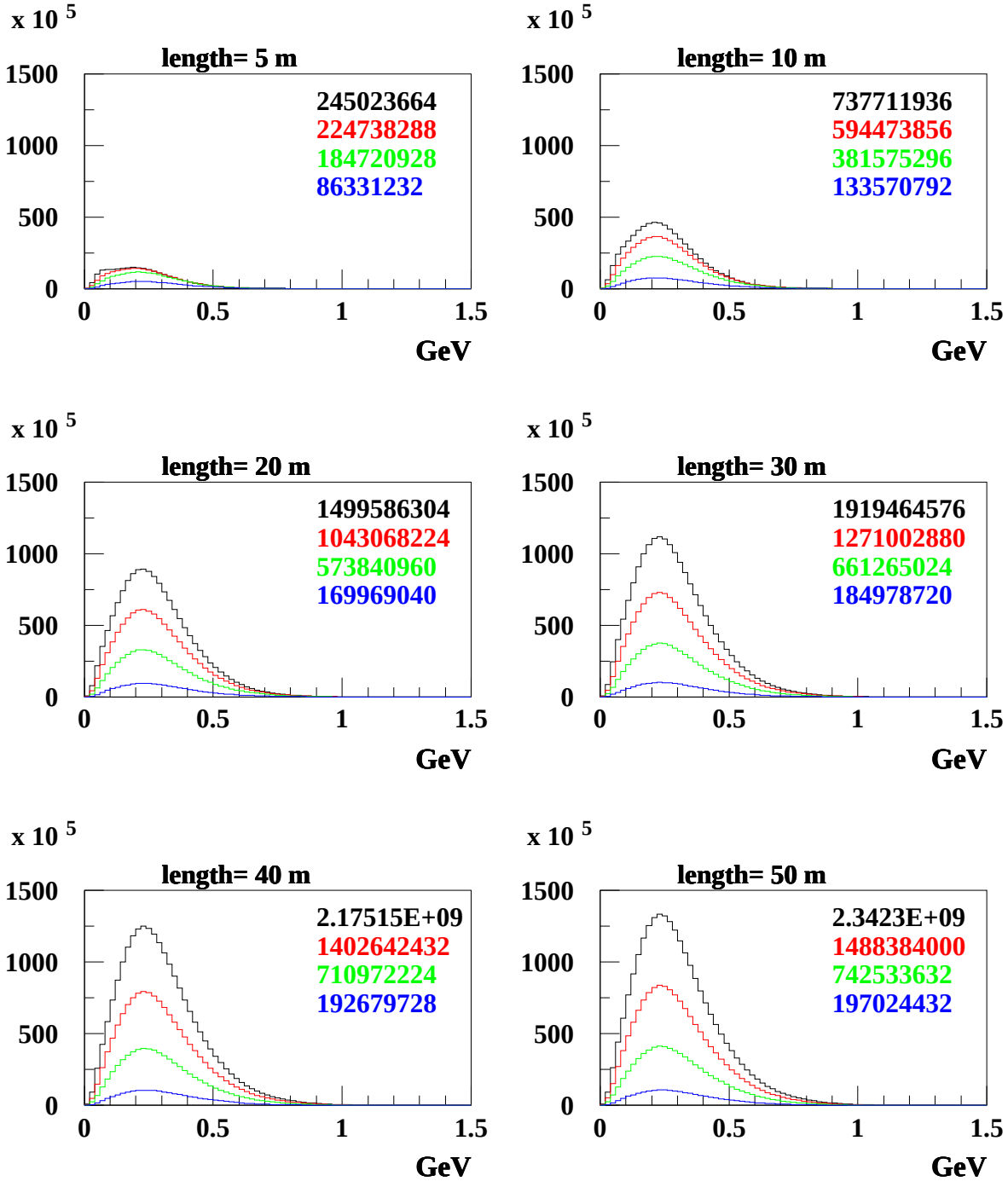


Figure 4.13: $\bar{\nu}_e$ fluxes from $\mu^- \rightarrow e^- \bar{\nu}_e \nu_\mu$, focusing $\pi^+$. Numbers are integrated fluxes. In black radius = 100 cm, in red radius = 75 cm, in green radius = 50 cm, in blue radius = 25 cm

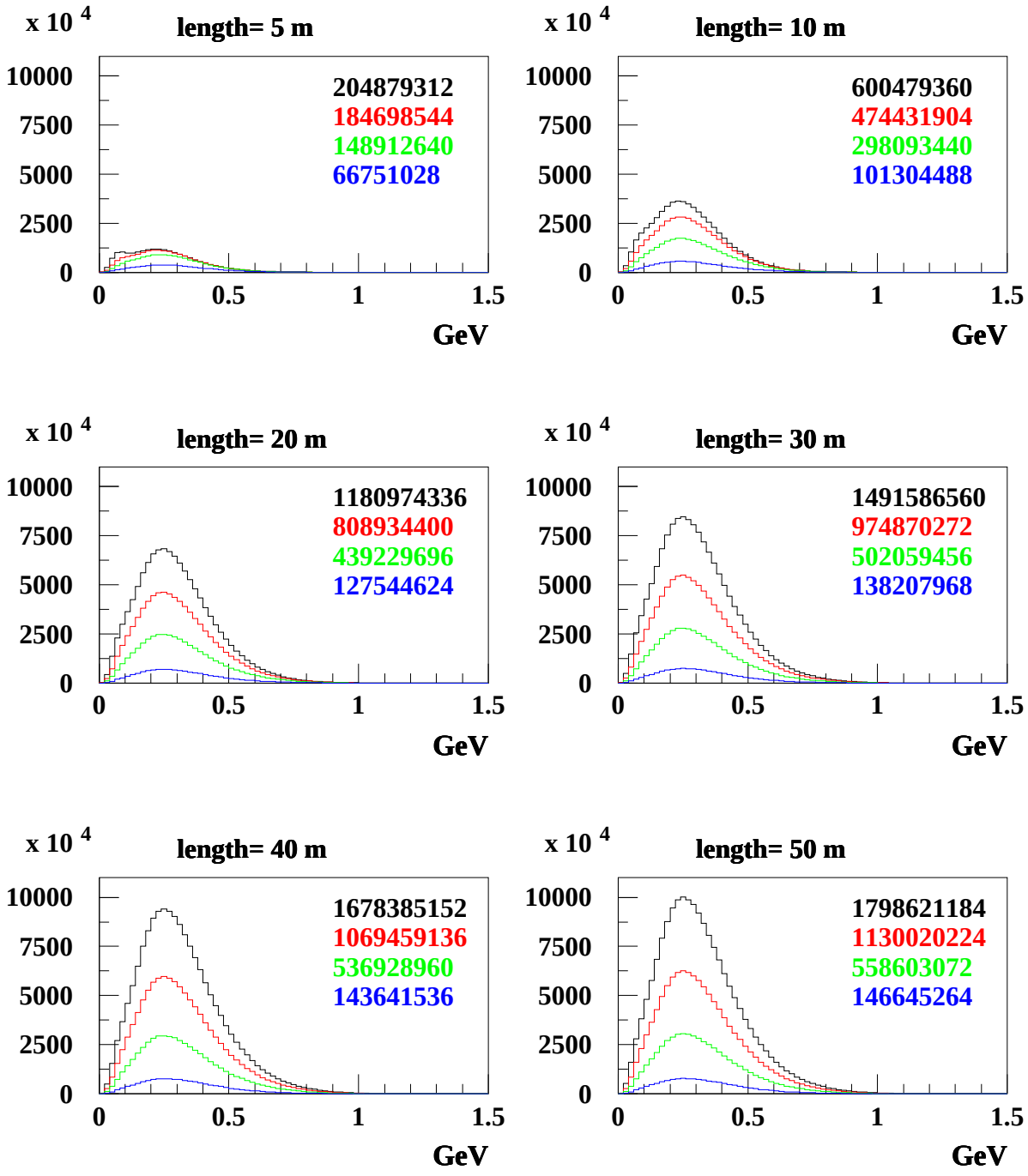


Figure 4.14: $\nu_\mu$ fluxes from $\mu^- \rightarrow e^- \bar{\nu}_e \nu_\mu$, focusing $\pi^+$. Numbers are integrated fluxes. In black radius = 100 cm, in red radius = 75 cm, in green radius = 50 cm, in blue radius = 25 cm

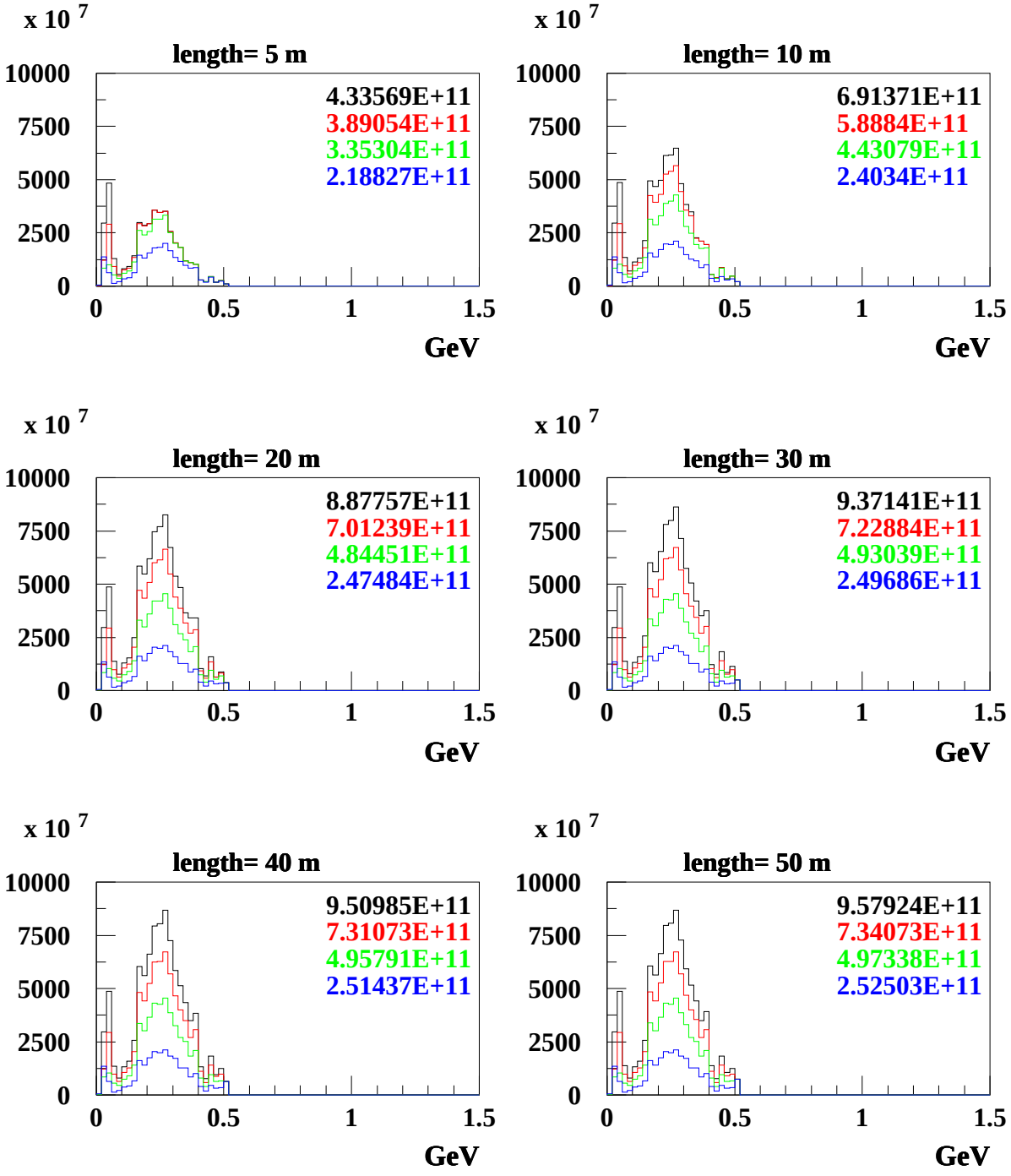


Figure 4.15: $\nu_\mu$ fluxes from $\pi^+ \to \mu^+\nu_\mu$, focusing $\pi^-$. Numbers are integrated fluxes. In black radius = 100 cm, in red radius = 75 cm, in green radius = 50 cm, in blue radius = 25 cm

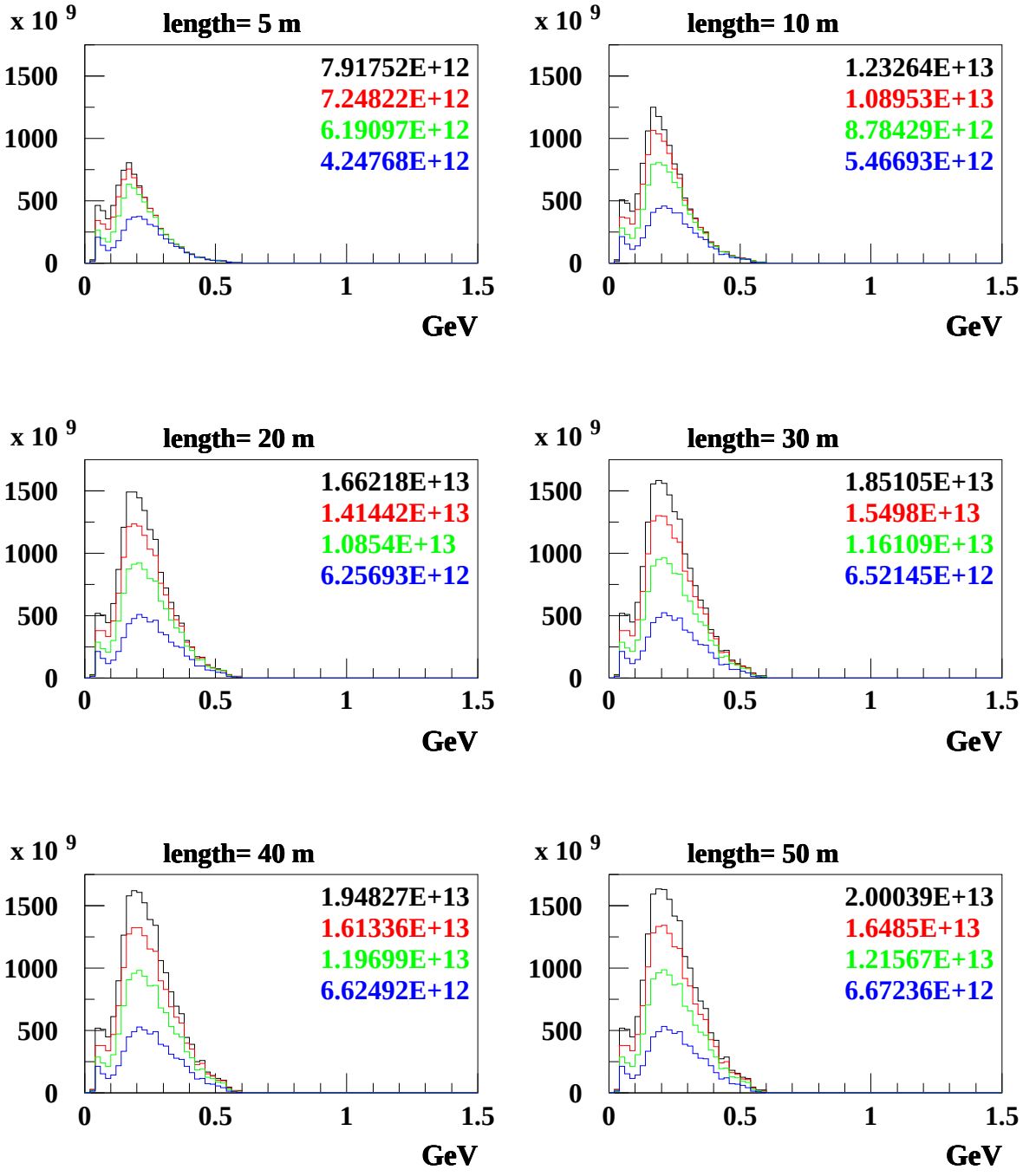


Figure 4.16: $\bar{\nu}_\mu$ fluxes from $\pi^- \rightarrow \mu^- \bar{\nu}_\mu$, focusing $\pi^-$. Numbers are integrated fluxes. In black radius = 100 cm, in red radius = 75 cm, in green radius = 50 cm, in blue radius = 25 cm

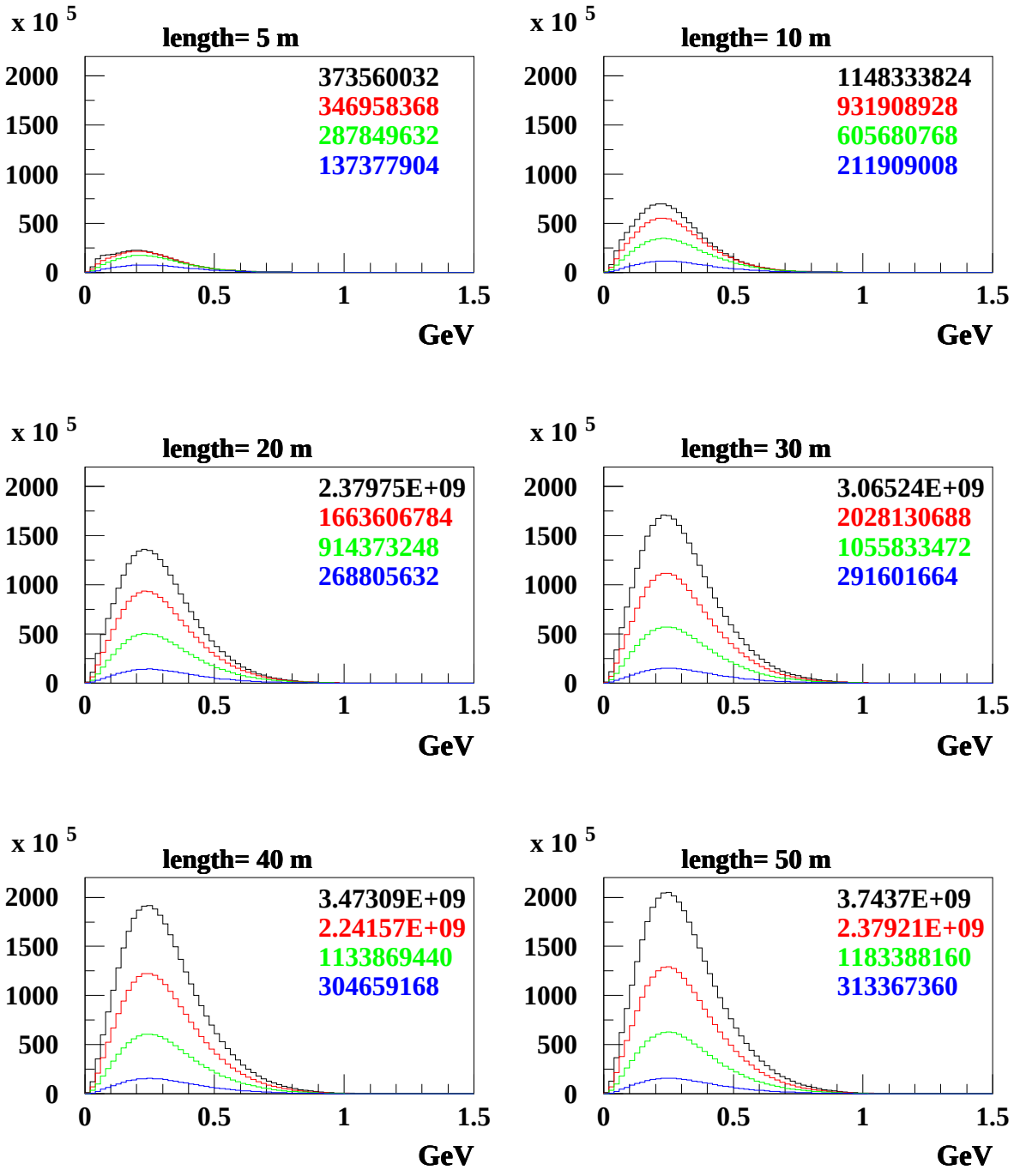


Figure 4.17: $\nu_e$ fluxes from $\mu^+ \to e^+\nu_e\bar{\nu}_\mu$, focusing $\pi^-$. Numbers are integrated fluxes. In black radius = 100 cm, in red radius = 75 cm, in green radius = 50 cm, in blue radius = 25 cm

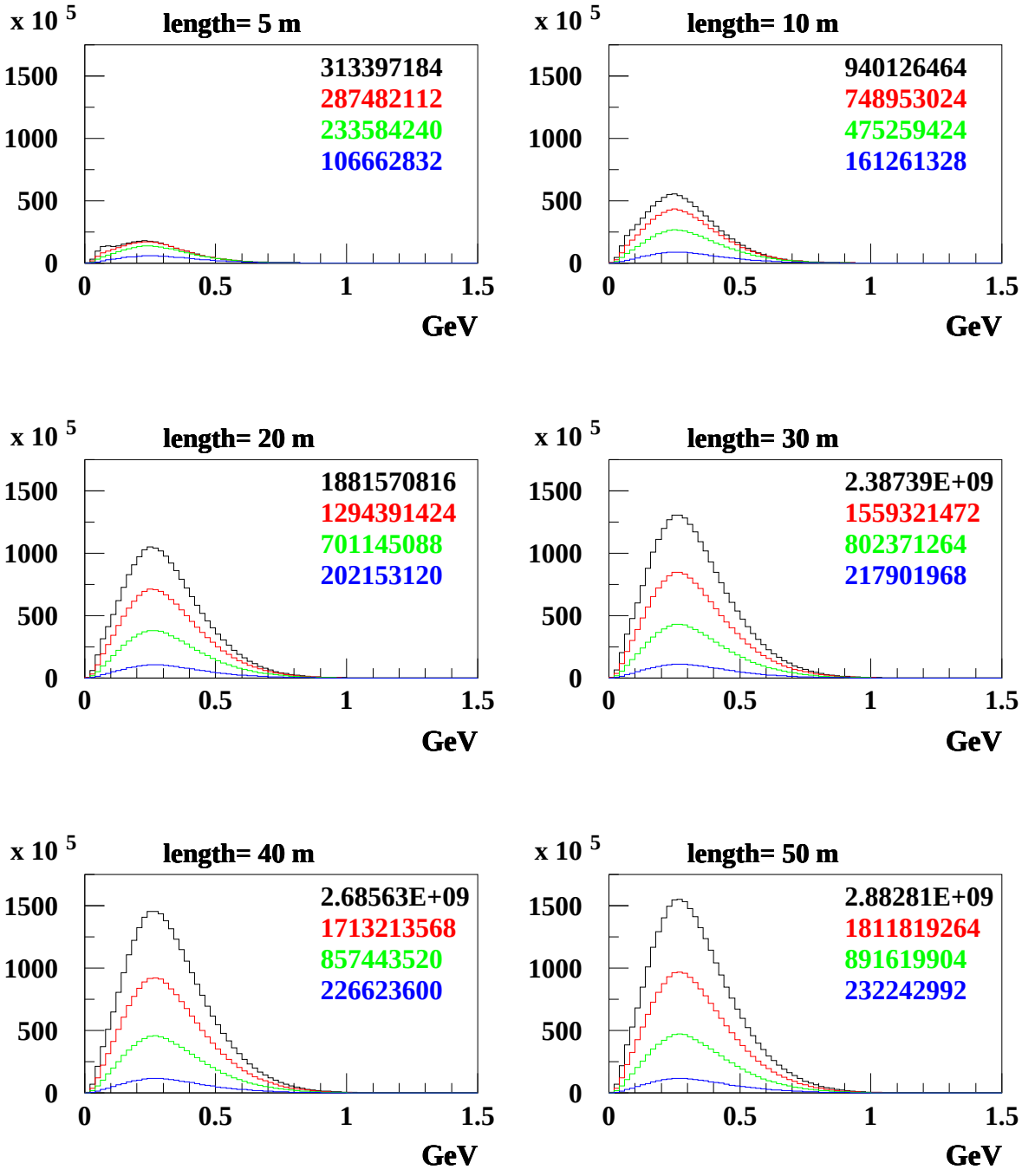


Figure 4.18: $\bar{\nu}_\mu$ fluxes from $\mu^+ \rightarrow e^+\nu_e\bar{\nu}_\mu$, focusing $\pi^-$. Numbers are integrated fluxes. In black radius = 100 cm, in red radius = 75 cm, in green radius = 50 cm, in blue radius = 25 cm

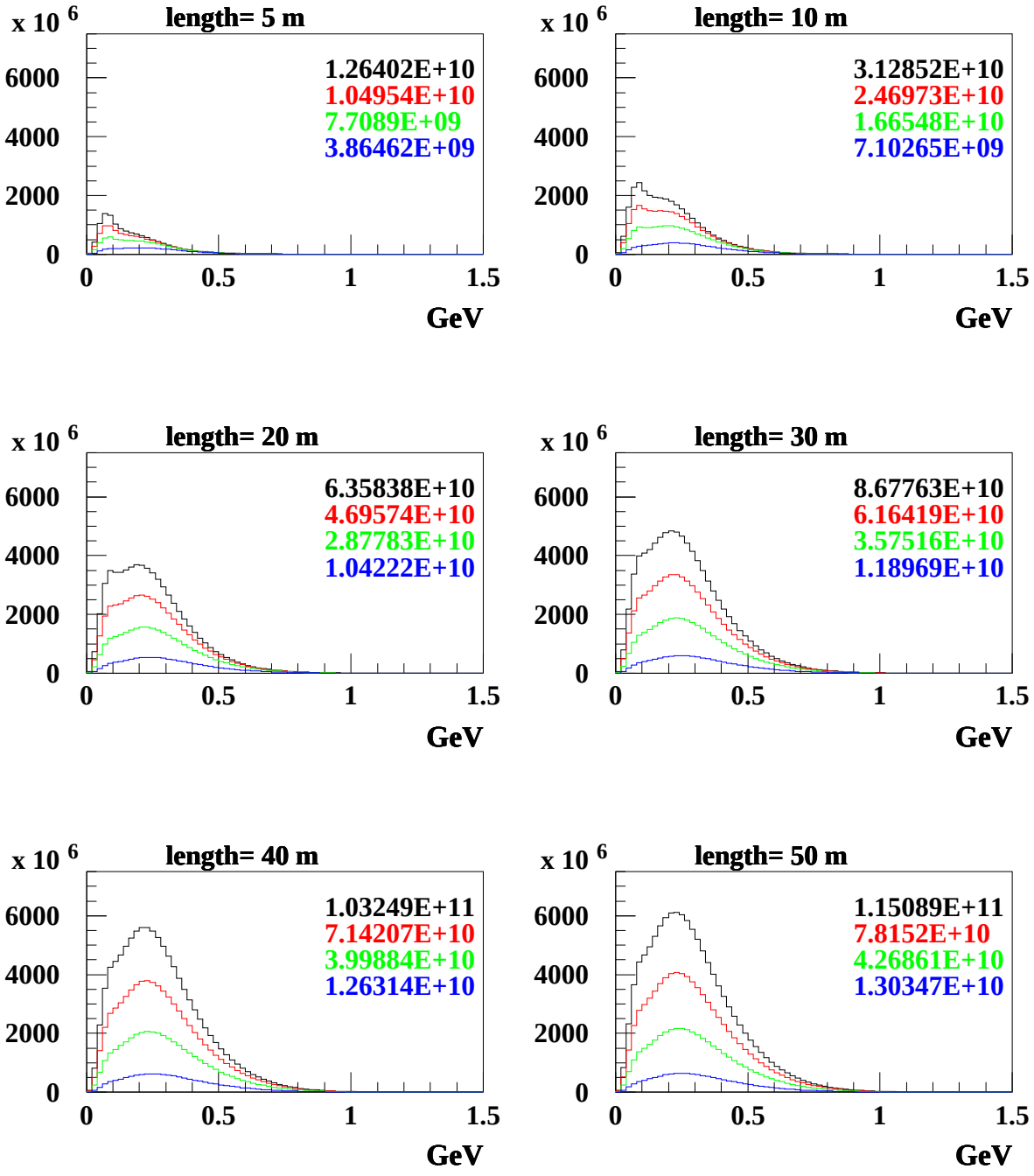


Figure 4.19: $\bar{\nu}_e$ fluxes from $\mu^- \rightarrow e^- \bar{\nu}_e \nu_\mu$, focusing $\pi^-$. Numbers are integrated fluxes. In black radius = 100 cm, in red radius = 75 cm, in green radius = 50 cm, in blue radius = 25 cm

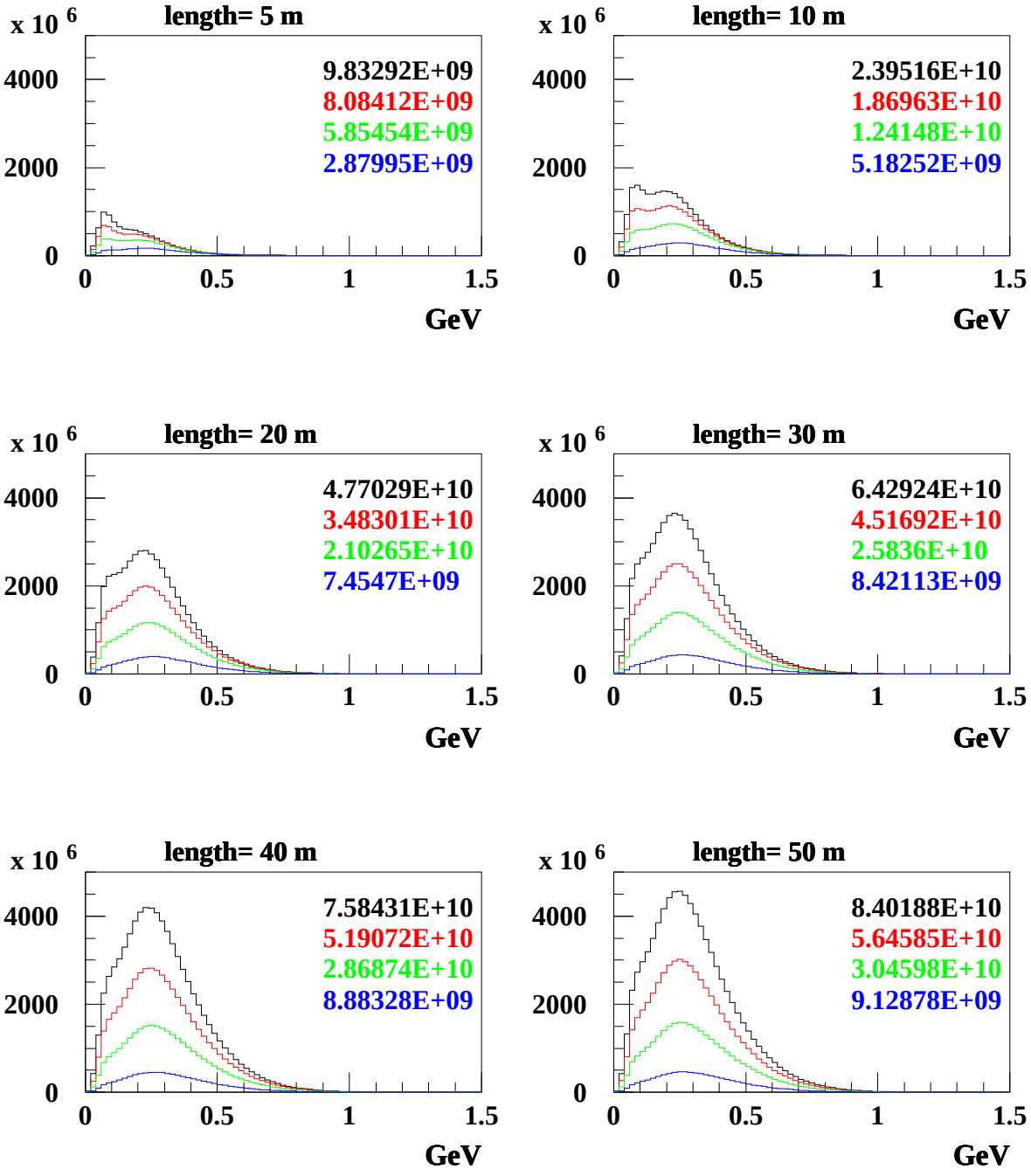


Figure 4.20: $\nu_\mu$ fluxes from $\mu^- \rightarrow e^- \bar{\nu}_e \nu_\mu$, focusing $\pi^-$. Numbers are integrated fluxes. In black radius = 100 cm, in red radius = 75 cm, in green radius = 50 cm, in blue radius = 25 cm

# Chapter 5

# Detectors

There are many factors that influence the detector choice. Mainly these can be summarized as:
- detector mass (dimensions): this affects the total number of events detected and the statistical errors of the observations;
- kind of detector: the main problems are background rejection and systematic errors depending on the technique used.
In this study two solutions has been analyzed: a water Cerenkov (Super Kamiokande-like) and a liquid scintillator (MiniBooNE-like), neglecting cost estimations (anyway attention has been payed not to propose impossible solutions).
The first issue of this analysis is the distance between neutrino production point and the detector. This is dictated by two needs: neutrino oscillation pattern and flux considerations. This experiment would aim to observe neutrino oscillations $\nu_\mu \rightarrow \nu_e$ and measure oscillation parameters (in particular $\theta_{13}$); hence the best target - detector distance should be approximatively over one of the possible oscillation peaks. The oscillations as a function of the distance is shown in figure (5.1), for a mean energy of 250 MeV, for the LMA (Large Mixing Angle) solution $\sin^2(2\theta_{12}) = 0.8$, $\sin^2(2\theta_{23}) = 1$, $\sin^2(2\theta_{13}) = 0.01$, $\delta m^2_{12} = 5\,10^{-5}\,eV^2$, $\delta m^2_{23} = 3.2\,10^{-3}\,eV^2$.
The probability, for a fixed energy, has a structure function of the distance. The oscillation "period" is about 200 km and the first peak is at about 100 km. Although the probability has a superimposed oscillation behaviour with a larger period and it increases going to larger distances, it is not convenient for this experiment to use successive peaks (the second being at 300 km). Neutrino flux decrease with the square of the distance and beyond the first

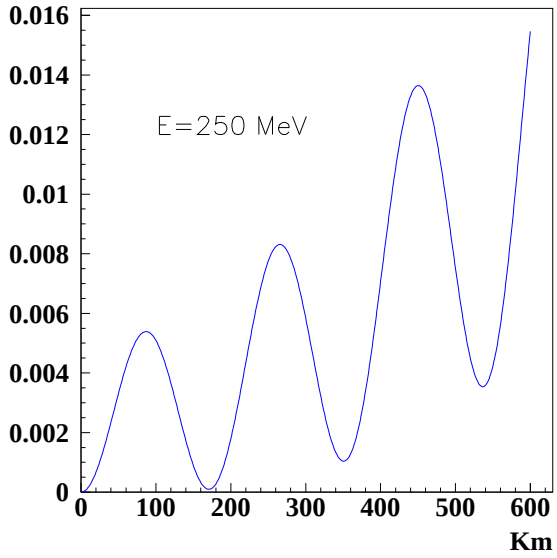


Figure 5.1: Oscillation probability $p(\nu_\mu \rightarrow \nu_e)$ as function of L (km) for a mean energy of 250 MeV.

peak the signal would become too small to be detected with a reasonable detector size.
A detector for neutrino experiments must be shielded by the background due to cosmic rays. Hence its location is usually chosen to be deep underground. In a first analysis it was suggested a detector in the Leman (Geneva) lake, but it has been discarded. In fact this lake it is not deep enough (600 m). Another, more exotic, scenario considered for neutrino experiment, is a detector undersea [62],[63], but it has been excluded for this experiment because of the CERN location (too far away from the sea) .
If an existing laboratory is required, it is possible to make a rough observation of the possible sites using a map (see figure(5.2)). Possible sites for the detector can be:
- LSM (Laboratoire Souterrain de Modane) $\simeq$ 130 km;
- old Monte Bianco laboratory $\simeq$ 60 km.
The second parameter to take into account is the detector mass. Independently from its nature, this parameter is directly related to the number of observable events for two reasons: the solid angle covered by the detector is proportional to its area and the number of possible neutrino interactions

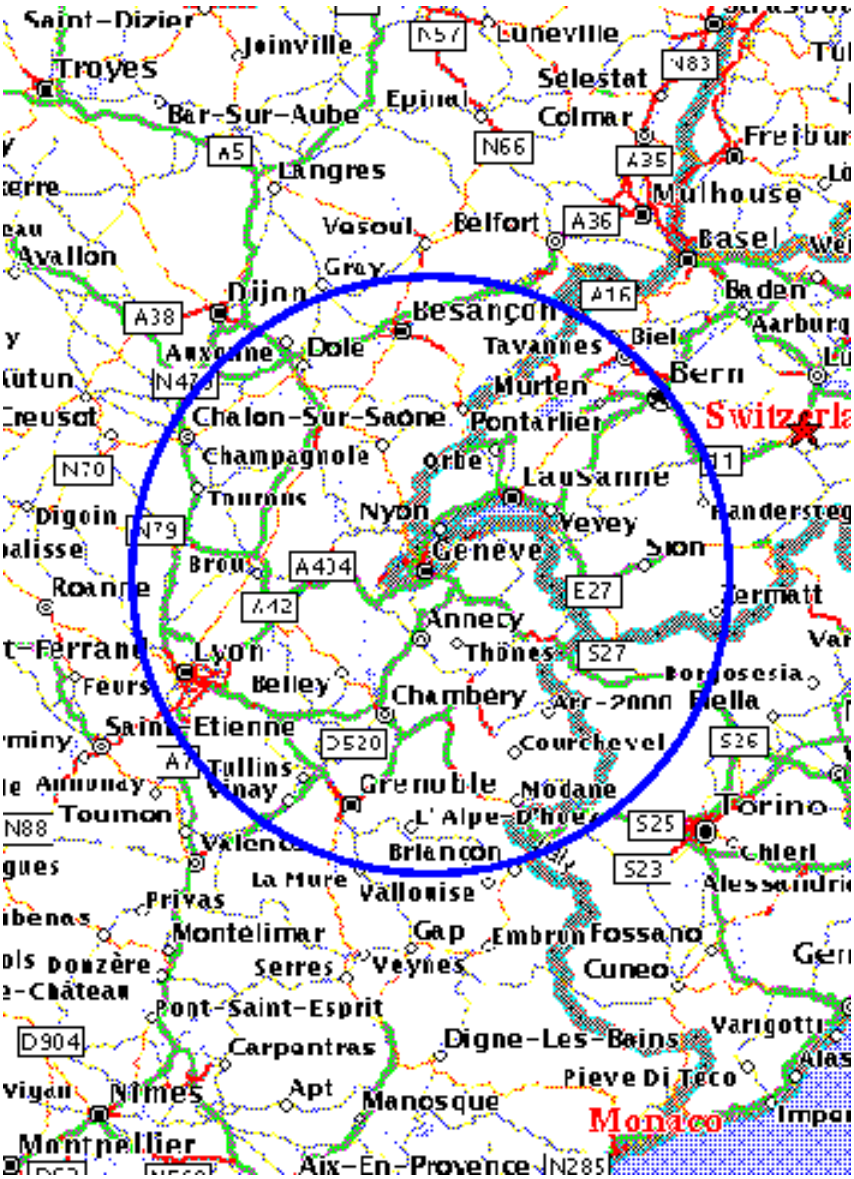


Figure 5.2: Possible detector sites.

is directly proportional to the depth of the detector. Due to the distance from the target, it makes nonsense to increase the detector area because the covered solid angle would increase negligibly. On the other hand the depth of the detector can increase sensibly the number of events, but it is limited by its cost.
The largest uncertainty on the oscillations measurement arise from systematic errors on flux estimations, from the little knowledge about neutrino interaction at these energies and from the detector efficiency. For these reasons it has been suggested to use two detectors: a near one for a precise flux measurement and to study neutrino cross sections and a distant one for the real oscillation experiment. If a distant detector identical to the near one is chosen, then it would be possible to eliminate systematic errors on the detector accuracy simply taking the ratio between the two measured signals.
The detector mass considered is 40 kton. The major problem of this experiment arises from the low number of collected events, hence the detector mass has been chosen in order to ensure a significant number of events, assuming a period of 5 years of data taking.
The typical detector design is composed by two parts: the inner detector, devoted to the observation of neutrino events, and the outer one acting as veto detector for cosmic rays and as a shield from rocks radioactivity.
In figure (5.3)(5.4) artistic schemes of SuperK (water Cerenkov) and MiniBooNE (scintillator) are shown.
The parameters describing the two detectors are summarized in tables (5.1), (5.2).

## 5.1 Water Cerenkov

This kind of detector observes relativistic particles through their emission of Cerenkov light [65]. Water is used as active material to produce Cerenkov radiation. The choice of this material is based on three basic consideration: its low cost, high transparencies and reachable purity.
When a charged particle pass trough a medium with speed faster than light in that medium, a shock wave of radiation, in the visible part of the spectra, is emitted at a fixed angle with respect to the particle trajectory (figure (5.5)). The wavefront creates a cone with an angle ($\theta$) depending on the speed ($\beta$)

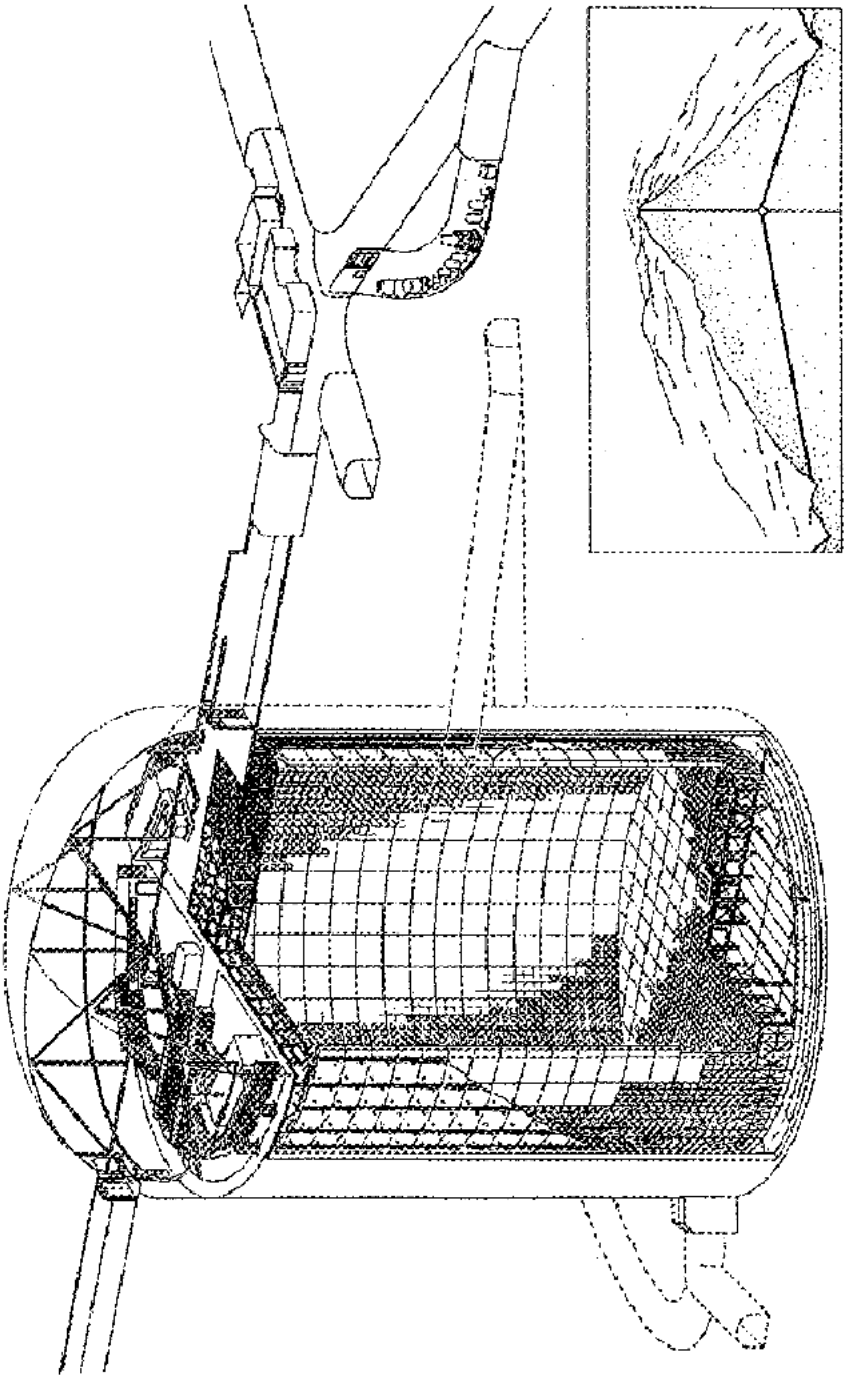

Figure 5.3: Super Kamiokande layout. [21]

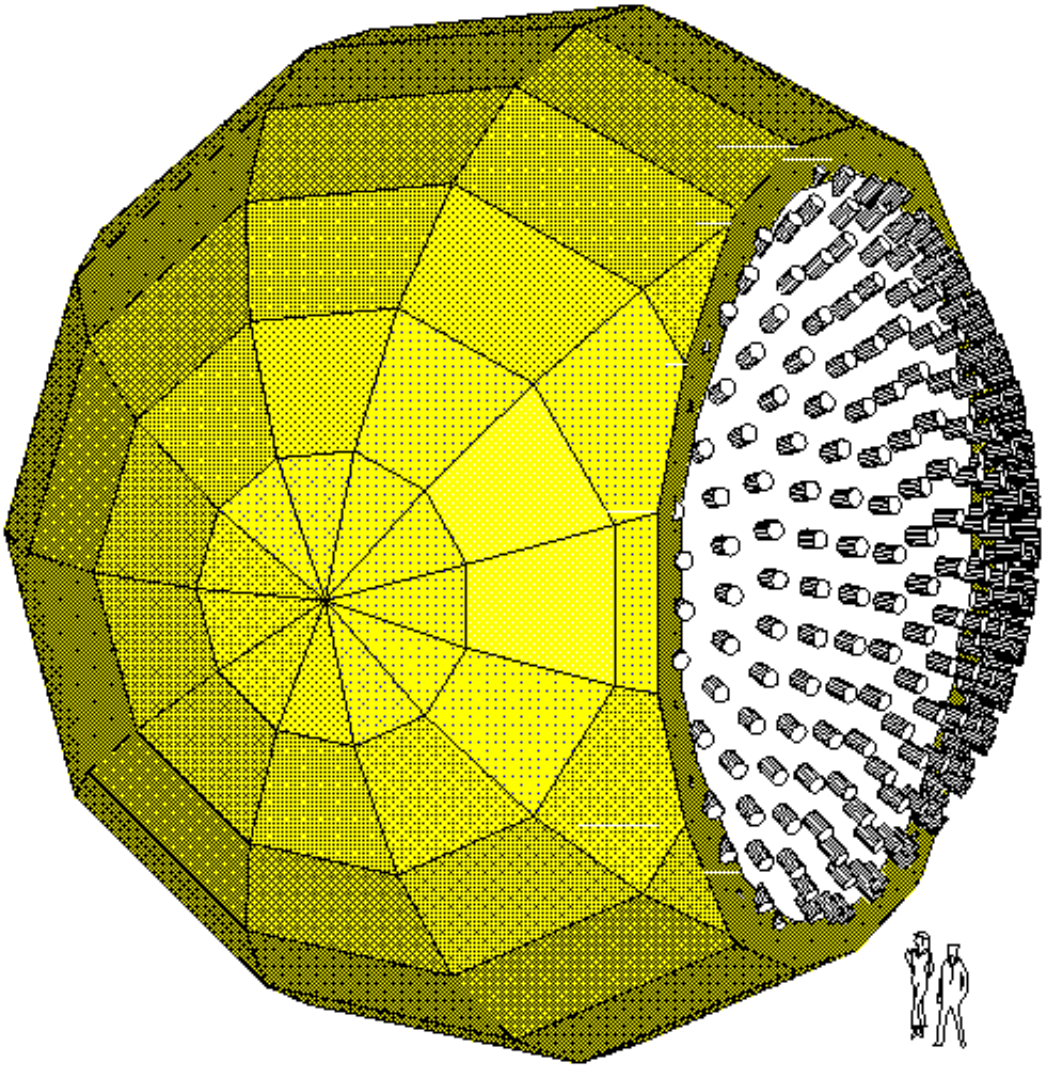

Figure 5.4: MiniBooNE layout.[44]

| Tank | Dimensions | 38 diameter 42m height |
|---|---|---|
| | Volume | 50kton |
| Outer detector | Thickness | 2.6m |
| | Volume | 32 kton |
| | Number of PMT | 1885 |
| Inner detector | Dimension | 3.8m diameter 36.2m height |
| | Volume | 18 kton |
| | Number of PMT | 9398 (40%) |
| Fiducial volume | | 22 kton |

Table 5.1: SuperK datas [21].

| Tank | Dimensions | 12 m diameter |
|---|---|---|
| | Volume | 0.77 kton |
| Outer detector | Thickness | 0.5m |
| | Volume | 0.18 kton |
| | Number of PMT | 292 |
| Inner detector | Dimension | 11 m radius |
| | Volume | 0.6 kton |
| | Number of PMT | 1220 (10%) |
| Fiducial volume | | 0.45 kton |

Table 5.2: MiniBooNE datas [44].

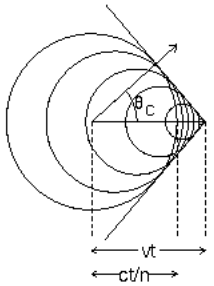


Figure 5.5: Cerenkov radiation.

of the particle:

$$\cos\theta = \frac{1}{\beta n}$$

where $n$ is the refractive index of the medium.
An important characteristic of this kind of radiation is that the light is emitted whenever the speed of the particle exceed a critical value,

$$\beta_c n > 1$$

determining a correspondent critical angle for the radiation emission:

$$\theta_c = arccos\frac{1}{n}$$

In a water Cerenkov detector this radiation is collected by an array of PMT (covering the internal face of the tank) and the ring image is reconstructed via software. The usual procedure is to find an initial vertex and direction using PMT timing informations, then the number of rings is found, with reconstruction software and finally a particle is assigned to each ring. Typical images for electron and muon events are shown in figure (5.6), (5.7).

## 5.2 Scintillator

The scintillation process is triggered by an energy exchange between the particle to detect and the molecules of the scintillator [65]. When a particle moves in a medium brings the molecules onto one of their excited states; these will release energy with the typical exponential law of the fluorescence

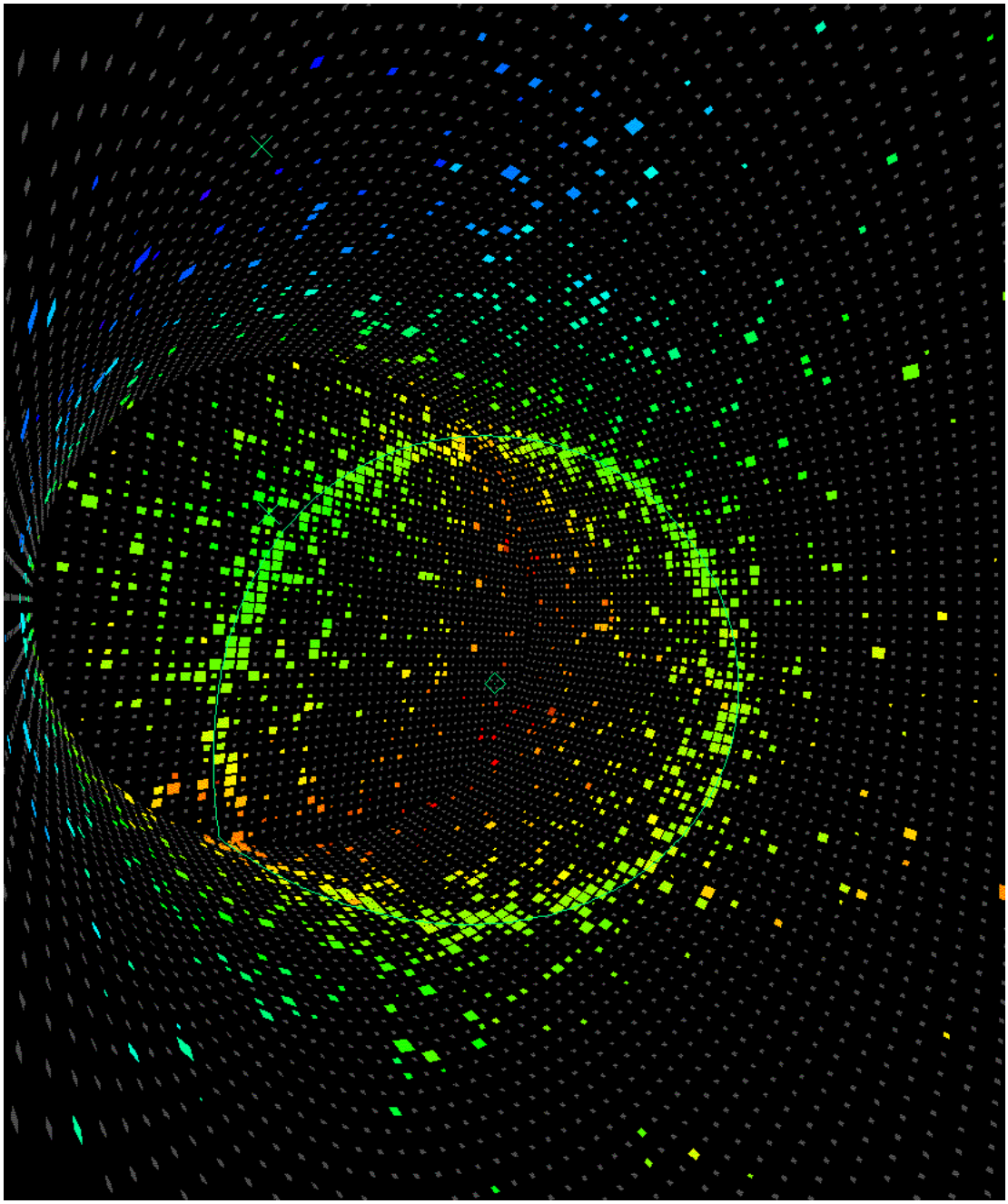

Figure 5.6: Electron event in Super Kamiokande.[21]

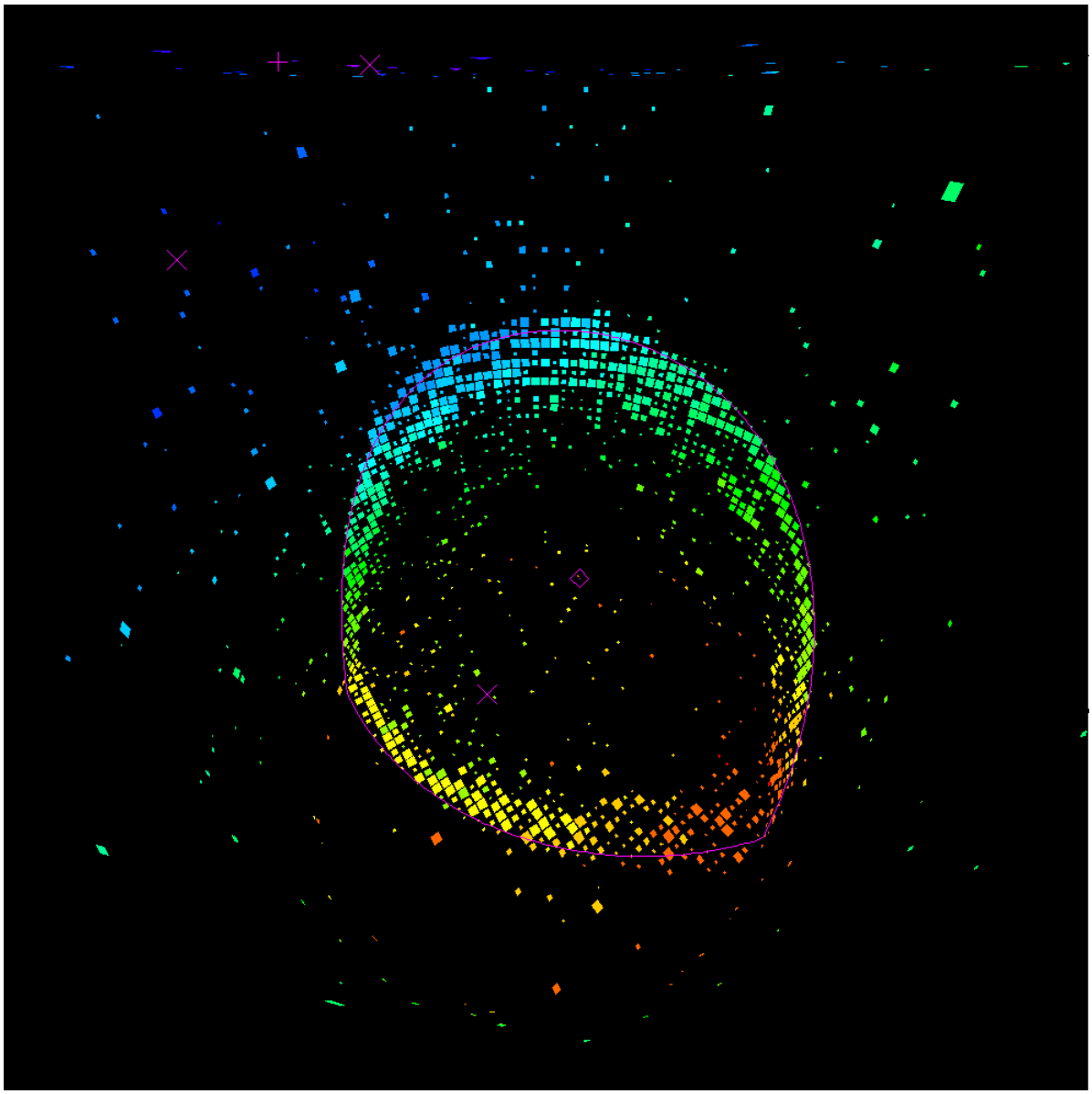

Figure 5.7: Muon event in Super Kamiokande.[21]

decay. An important characteristic of organic scintillators is that the emitted light is produced by single molecules and not by a crystalline lattice. This allows to use organic scintillators diluted in other materials.
There are three main differences between Cerenkov light and scintillation light. The first one is that the light is emitted in the typical range of picoseconds for Cerenkov radiation while the typical range for scintillation light is in the order of nanoseconds, which is the normal mean-life of the excited states of a molecule. The second difference is that Cerenkov light is emitted on a preferencial direction, resulting in a cone, while the scintillation lights is emitted isotropically. Another difference is that Cerenkov light is emitted above an energy threshold depending in the mass of the particle, while there is no threshold in the scintillation process. The two phenomena of Cerenkov and scintillation light are not exclusive. For example in MiniboNE is quoted that 75% of the light comes from Cerenkov radiation while the remaining 25% is scintillation light.
The main challenge for this kind of experiments is to distinguish between electrons and muons going through the detector. The use of both Cerenkov and scintillation light can be used as a powerful tool to reduce this ambiguity. In fact below 1 GeV electrons and muons have very different velocities; muons falls below the Cerenkov threshold much before electrons hence it is possible to look at them only with the scintillation light, while electrons will be observed with both scintillation light and Cerenkov ring.

## 5.3 Event analysis

With a neutrino energy from few tens of MeV up to 1 GeV, the main reactions in the detector are:

| | |
|---|---|
| Charged current quasi elastic scattering: | $\nu + N \rightarrow lepton + N'$ |
| Neutral current elastic scattering: | $\nu + N \rightarrow \nu + N$ |

the second reaction for both $\nu_e$ and $\nu_\mu$ escapes the detection in a water Cerenkov detector and will be ignored in the following
Other possible but less frequent reactions are:

| | |
|---|---|
| Charged current resonant scattering: | $\nu + N \rightarrow lepton + \pi + N'$ |
| Neutral current resonant scattering: | $\nu + N \rightarrow \nu + \pi^0 + N'$ |
| Charged current coherent scattering: | $\nu + O \rightarrow lepton + \pi + O$ |
| Neutral current coherent scattering: | $\nu + O \rightarrow \nu + \pi^0 + O$ |
| Charged current diffractive scattering: | $\nu + p \rightarrow lepton + p + \pi$ |
| Neutral current diffractive scattering: | $\nu + p \rightarrow \nu + p + \pi^0$ |
| Neutrino-electron scattering: | $\nu + e^- \rightarrow \nu + e^-$ |

Where:
- resonant means that the pion is produced via the decay of a nucleon resonance (e.g. $\Delta$)
- coherent means a reaction at low energy which can be though occuring with the entire target nucleus
- diffractive means a reaction occurred with a single nucleon
All these reactions usually produce light in the detector. The informations available and analyzed in an experiment are:

- the number PMT recording light;
- the timing of the initial hit in each tube;
- the number of photoelectrons produced;
- the veto response;

Based on this information it is possible to identify particles emitted in the reactions, their energy and direction and to reconstruct the interaction vertex. The presence of a delayed coincidence can also be used to infer the presence of the decay of a muon stopped inside the detector.
The previous cited reactions can be divided into three classes:
1) events unambiguously recognized as $\nu_e$ interactions;
2) events unambiguously recognized as not being $\nu_e$ interactions (the detected charged particle is a muon);
3) ambiguous events in which it is not possible to assess whether they originate from a $\nu_e$ or $\nu_\mu$ interaction.
Non ambiguous $\nu_e$ events can originate from a $\nu_e$ coming from an oscillated $\nu_\mu$ or from a $\nu_e$ of the beam contamination. The events of classes two and three are usually cut. The following is the list of interactions that lead to class two events:
$\cdot\, \nu_\mu + N \rightarrow \mu^- + N'$ it appears only a $\mu$-like ring

$\cdot\, \nu_\mu + N \rightarrow \mu^- + \pi + N'$ the emitted $\mu$ and the pion produce $\mu$-like rings;
$\cdot\, \nu_\mu + N \rightarrow \nu_\mu + \pi + N'$ the emitted pion produces a $\mu$-like ring;
$\cdot\, \nu_e + N \rightarrow e^- + \pi + N'$ produce two rings one $\mu$-like for the emitted pion and the other $e$-like;
$\cdot\, \nu_e + N \rightarrow \nu_e + \pi + N'$ in this signal event the charged $\pi$ produces a $\mu$-like ring; although this is a $\nu_e$ interaction the difficulty to unambiguously discriminate the pion can lead to huge contamination from charged current quasi elastic scattering.
In addition the following reactions have to be cut away because can be produced by background contamination:
$\cdot\, \nu_\mu + N \rightarrow \nu_\mu + \pi^0 + N'$ and $\nu_e + N \rightarrow \nu_e + \pi^0 + N'$ where $\pi^0 \rightarrow \gamma\gamma$. If the two photons have similar energies it is possible to identify them with a reconstruction algorithm that separates the two rings, however it is not possible to distinguish between the two. Figure (5.8) shows a typical double ring caused by $\pi^0$
$\cdot\, \nu_\mu + N \rightarrow \mu^- + N'$ this is the most frequent reaction and it is crucial not to misidentify the $\mu$ in an $e$.
The two detectors considered reach high efficiency in rejecting the above backgrounds; the main source of background is then a real $\nu_e$ due to the contamination of the initial beam. This intrinsic background is clearly impossible to reduce. This is the reason why particular attention has been payed to the optimal decay tunnel geometry.
A characteristic of all the accelerator experiments is that the beam can be switched on and off. Moreover, usually, the neutrino beam has a time structure due to the time structure of the accelerator used to produce the initial pion beam. This characteristic facilitates considerably the measurement of the environmental background because it can be studied precisely with a beam-on beam-off subtraction.

## 5.4 Oscillated flux

In this section the expected flux of oscillated neutrinos into the detector is studied considering the updated oscillations values of the LMA solution (table 5.3). The oscillated fluxes are produced applying the three family oscillation scheme, as shown in the second chapter, to the fluxes generated with a decay tunnel of 20 m length and 1 m radius. As pointed out above

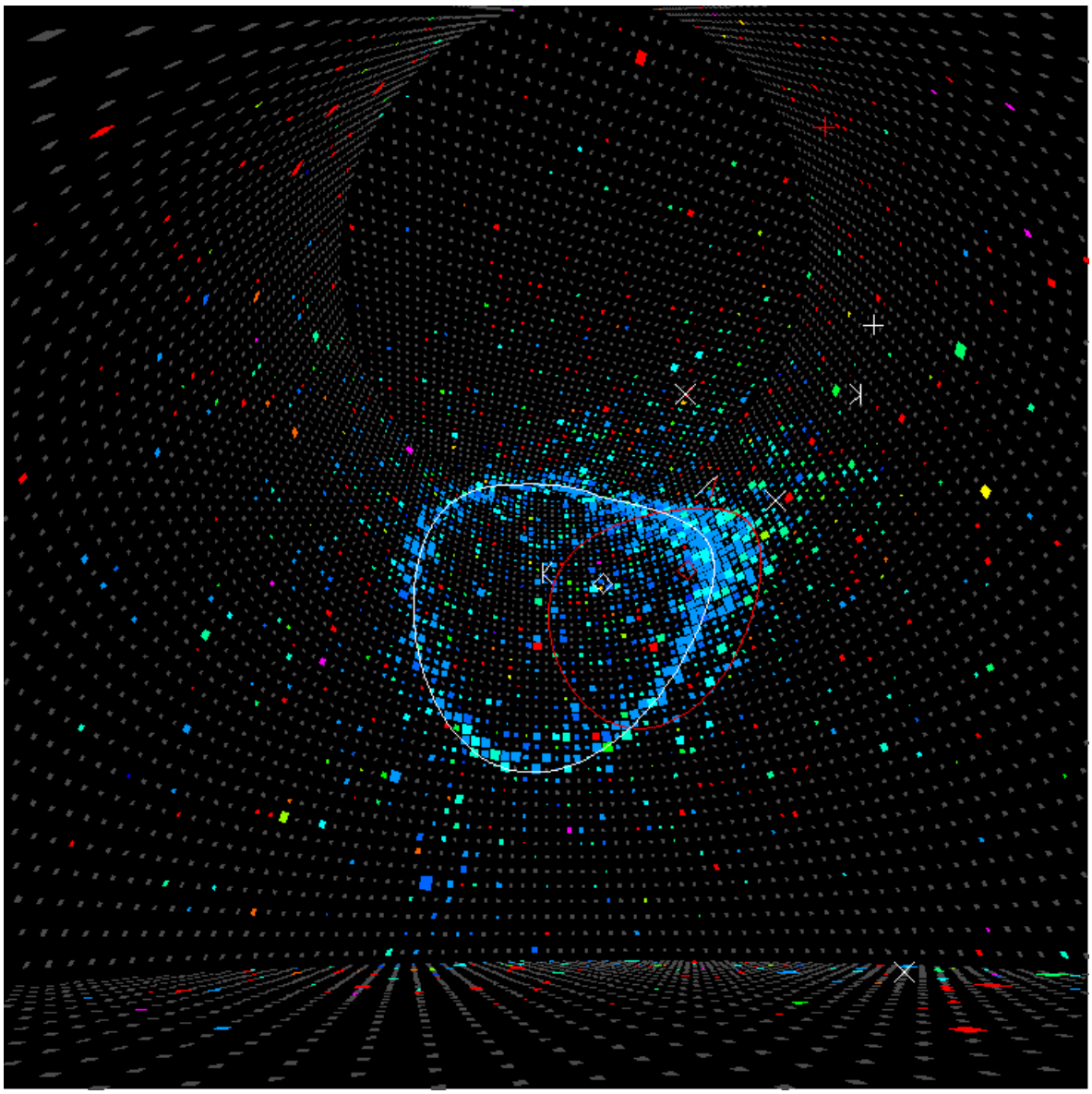

Figure 5.8: $\pi^0$ rings reconstruction in Super Kamiokande.[21]

| | |
|---|---|
| $sin^2 2\theta_{23}$ | 1 |
| $sin^2 2\theta_{12}$ | 0.8 |
| $sin^2 2\theta_{13}$ | 0.01 |
| $\delta m^2_{21}$ | $5\,10^{-}5$ |
| $\delta m^2_{32}$ | $3.2\,10^{-}3$ |

Table 5.3: Updated oscillation parameters (LMA solution).

the detector used is 40 kton mass and it is located at 130 km from the target (roughly corresponding to the distance between CERN and LSM (Laboratoire Souterrain de Modane)).
Using a magnetic horn focusing $\pi^+(\pi^-)$ the number of $\bar{\nu}(\nu)$ produced is three order of magnitude less than the signal hence they will be neglected through all the analysis.

In the following figures the oscillation probabilities as a function of energy and their effect on fluxes are shown. Fluxes are displayed as number of neutrinos per bin. The energy bin dimension is always 20 MeV.
It is possible to observe (figure(5.9),(5.10)) that the $p(\nu_e \rightarrow \nu_e)$ is almost equal to 1 for the whole energy range, excepted for the very first bins, hence the effect of the oscillations on $\nu_e$ is negligible. The $p(\nu_\mu \rightarrow \nu_\mu)$ has a large minimum at about 300 MeV and the resulting flux is practically cut at that energy (figure(5.11),(5.12)). The $p(\nu_\mu \rightarrow \nu_e)$ is the probability this experiment would take advantage of (figure (5.13)). This probability is very small; as can be seen from figure (5.14) the flux of oscillated $\nu_\mu$ is almost three order of magnitude lower than the flux of unoscillated $\nu_\mu$. The large fraction of the $\nu_\mu$ will oscillate into $\nu_\tau$ (figure (5.15),(5.16)) that are completely invisible to this experiment because their energy is far below the $\tau$ production threshold. The last figure (5.17) shows the total flux of $\nu_e$ and the intrinsic background of $\nu_e$ from the beam contamination.
The same kind of plots are shown for $\bar{\nu}_\mu$ when the polarity of the horn is inverted to focalize $\pi^-$, figure (5.18)-(5.26).

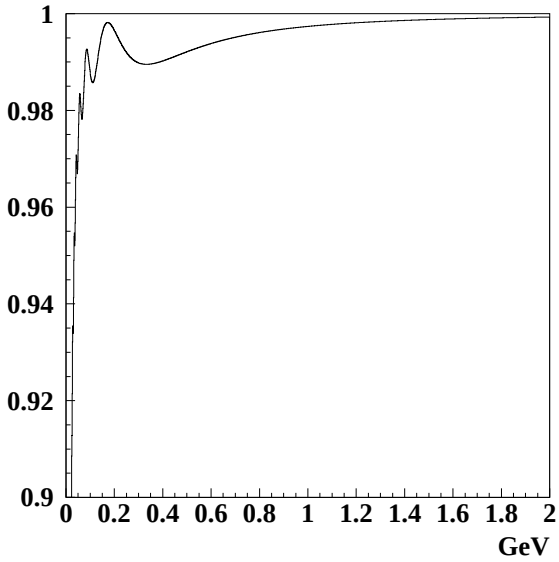


Figure 5.9: Oscillation probability $p(\nu_e \rightarrow \nu_e)$ for a fixed length of 130 km.

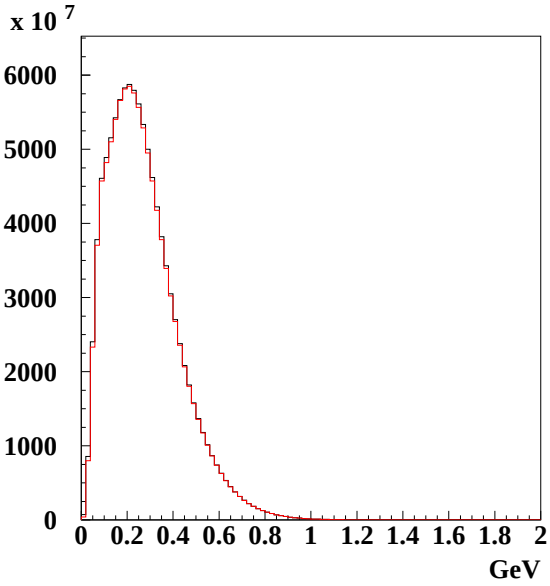


Figure 5.10: (black) Unoscillated $\nu_e$ flux and (red) oscillated $\nu_e \rightarrow \nu_e$ flux, for a fixed length of 130 km.

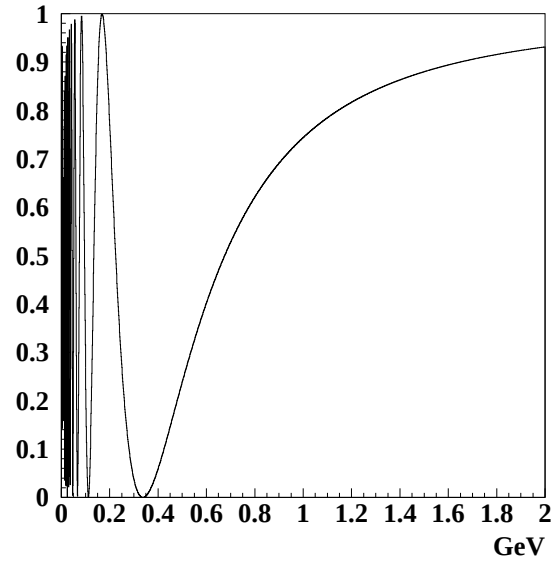


Figure 5.11: Oscillation probability $p(\nu_\mu \rightarrow \nu_\mu)$ for a fixed length of 130 km.

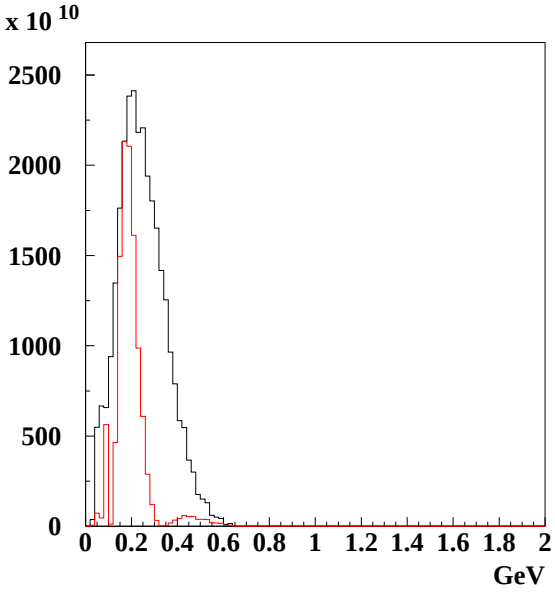


Figure 5.12: (black) Unoscillated $\nu_\mu$ flux and (red) oscillated $\nu_\mu \rightarrow \nu_\mu$ flux, for a fixed length of 130 km.

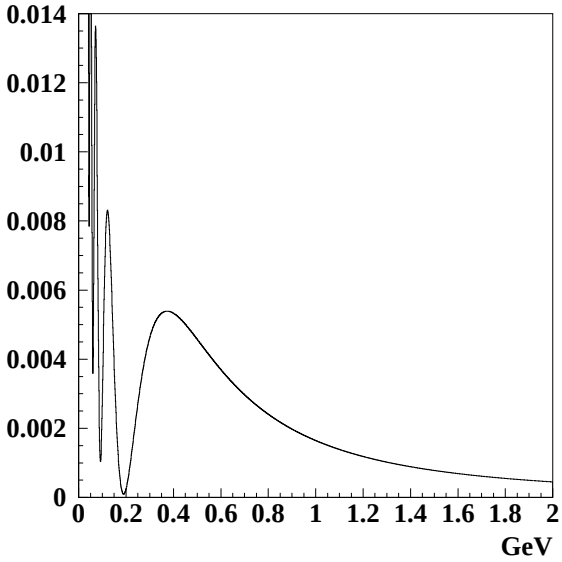


Figure 5.13: Oscillation probability $p(\nu_\mu \rightarrow \nu_e)$ for a fixed length of 130 km.

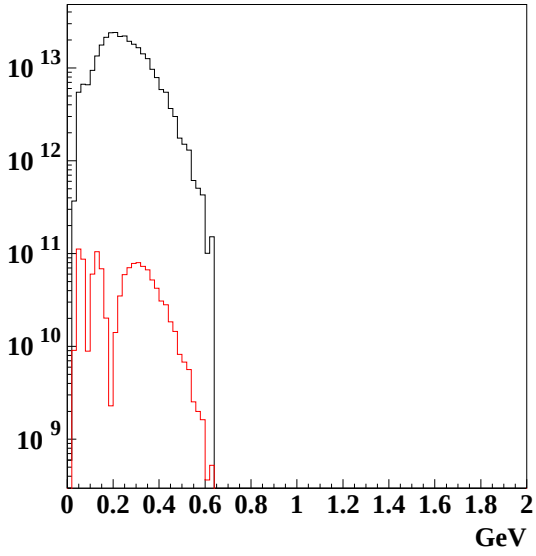


Figure 5.14: (black) Unoscillated $\nu_\mu$ flux and (red) oscillated $\nu_\mu \rightarrow \nu_e$ flux, three order of magnitude less, for a fixed length of 130 km.

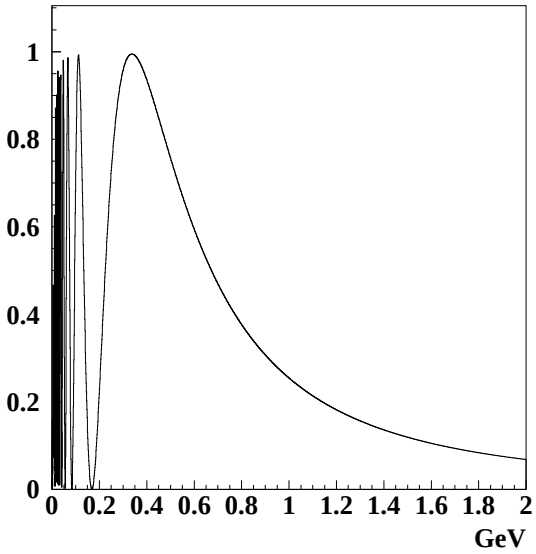


Figure 5.15: Oscillation probability $p(\nu_\mu \rightarrow \nu_\tau)$ for a fixed length of 130 km.

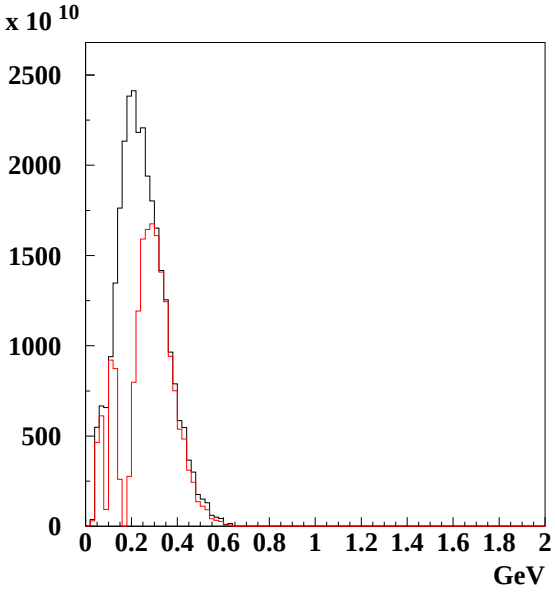


Figure 5.16: (black) Unoscillated $\nu_\mu$ flux and (red) oscillated $\nu_\mu \rightarrow \nu_\tau$ flux, for a fixed length of 130 km.

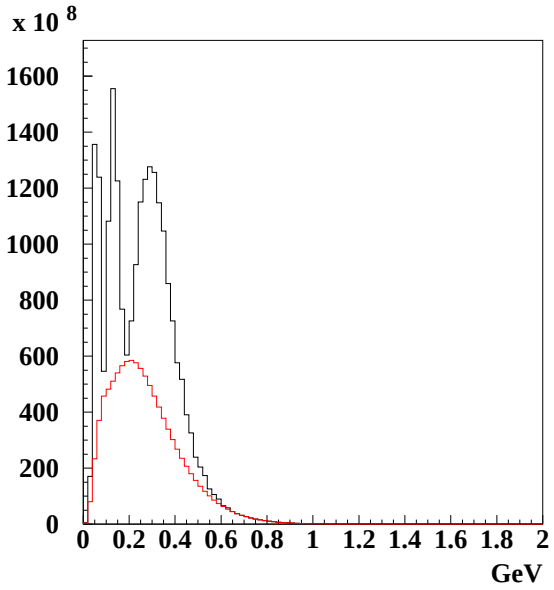


Figure 5.17: (black) Total $\nu_e$ flux, (red) $\nu_e$ flux from the beam, for a fixed length of 130 km.

## 5.5 Events

In this section the relation between the oscillated neutrino flux, and the detector is analyzed.
The number of neutrino interactions in the detector is a function of the neutrino energy, the length of the neutrino path in the detector and the cross section. The rate of interactions per second can be calculate with (5.1):

$$\frac{N_{events}}{s} = \sigma \left[\frac{cm^2}{nucleon}\right] \mathcal{N} \left[\frac{nucleon}{g}\right] \rho \left[\frac{g}{cm^3}\right] l\,[cm]\, \phi \left[\frac{\nu}{s}\right] \tag{5.1}$$

where:
$\sigma$ is the neutrino cross section
$\mathcal{N}$ is the Avogadro's number
$\rho$ is the density of the target material
$l$ is the length of the neutrino path in the detector
$\phi$ is the flux of neutrino per second.
The number of events has been analyzed using first the rough linear neutrino cross section without any events rejection and then a more accurate analysis

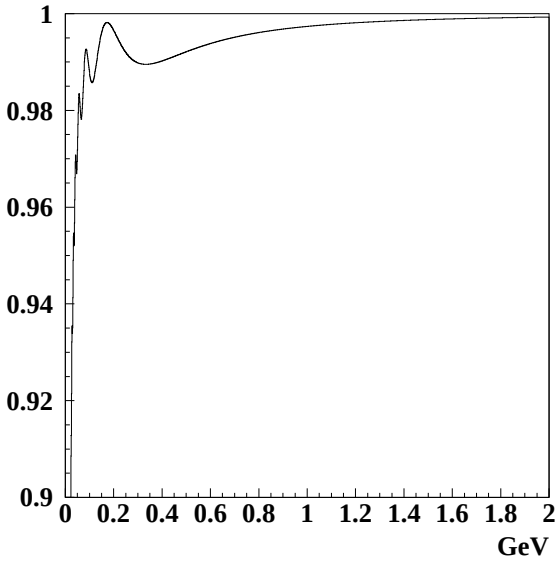


Figure 5.18: Oscillation probability $p(\bar{\nu}_e \rightarrow \bar{\nu}_e)$ for a fixed length of 130 km.

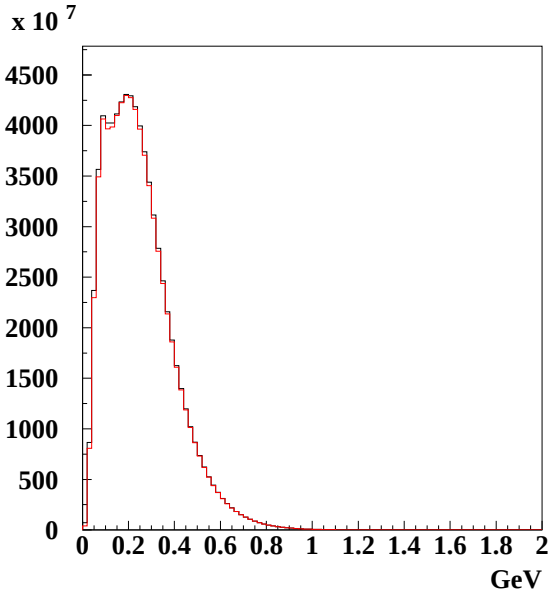


Figure 5.19: (black) Unoscillated $\bar{\nu}_e$ flux and (red) oscillated $\bar{\nu}_e \rightarrow \bar{\nu}_e$ flux, for a fixed length of 130 km.

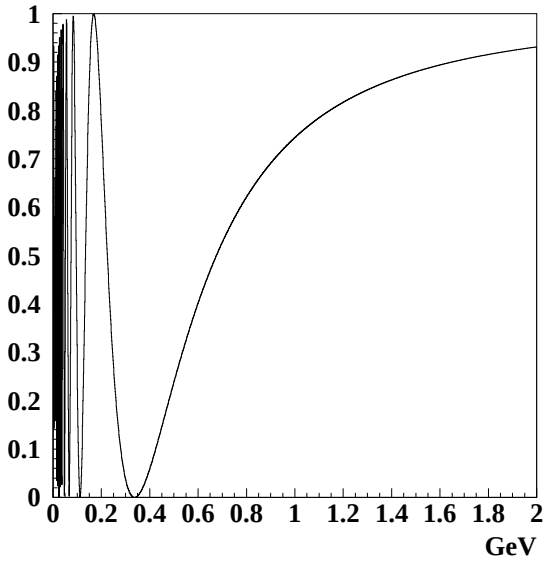


Figure 5.20: Oscillation probability $p(\bar{\nu}_\mu \rightarrow \bar{\nu}_\mu)$ for a fixed length of 130 km.

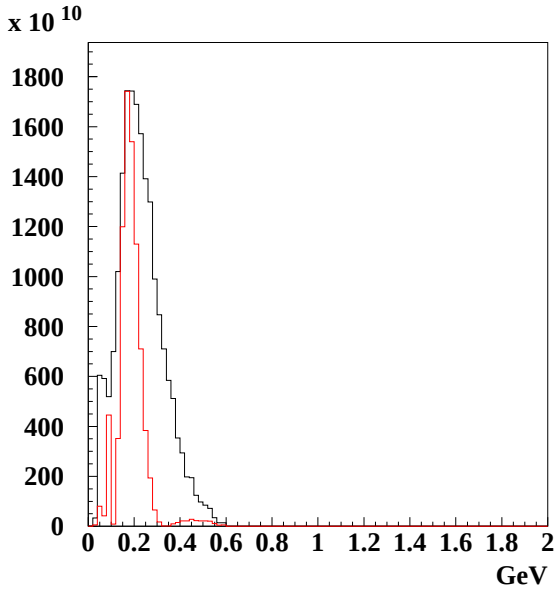


Figure 5.21: (black) Unoscillated $\bar{\nu}_\mu$ flux and (red) oscillated $\bar{\nu}_\mu \rightarrow \bar{\nu}_\mu$ flux, for a fixed length of 130 km.

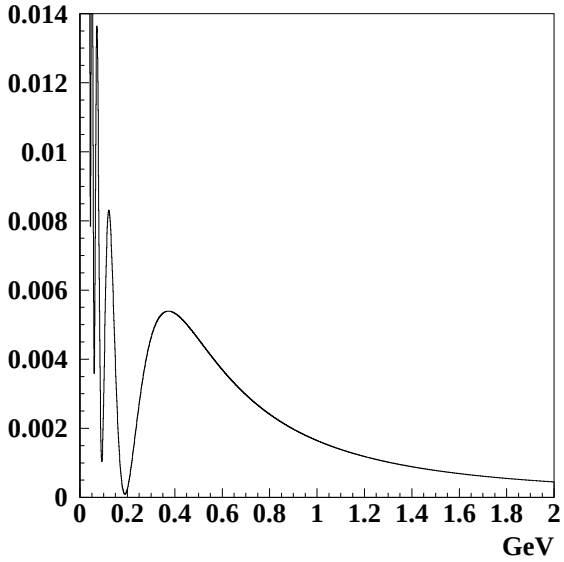


Figure 5.22: Oscillation probability $p(\bar{\nu}_\mu \rightarrow \bar{\nu}_e)$ for a fixed length of 130 km.

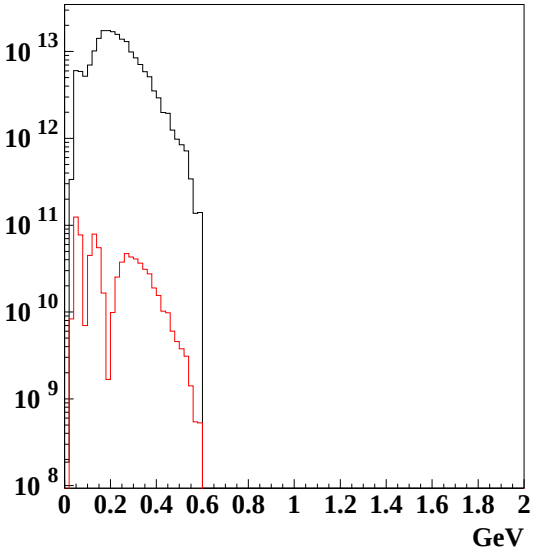


Figure 5.23: (black) Unoscillated $\bar{\nu}_\mu$ flux and (red) oscillated $\bar{\nu}_\mu \rightarrow \bar{\nu}_e$ flux, three order of magnitude less, for a fixed length of 130 km.

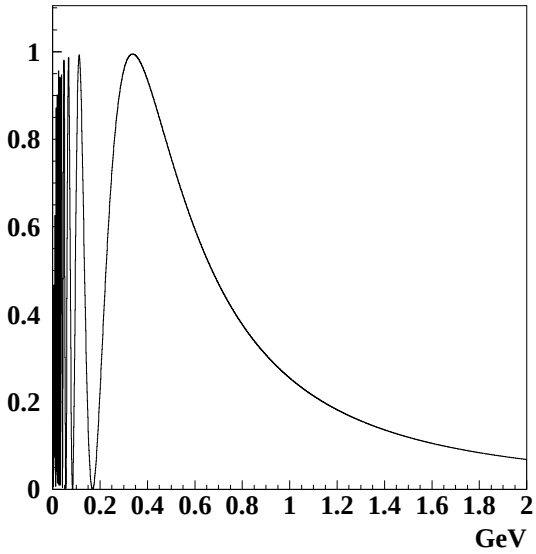


Figure 5.24: Oscillation probability $p(\bar{\nu}_\mu \rightarrow \bar{\nu}_\tau)$ for a fixed length of 130 km.

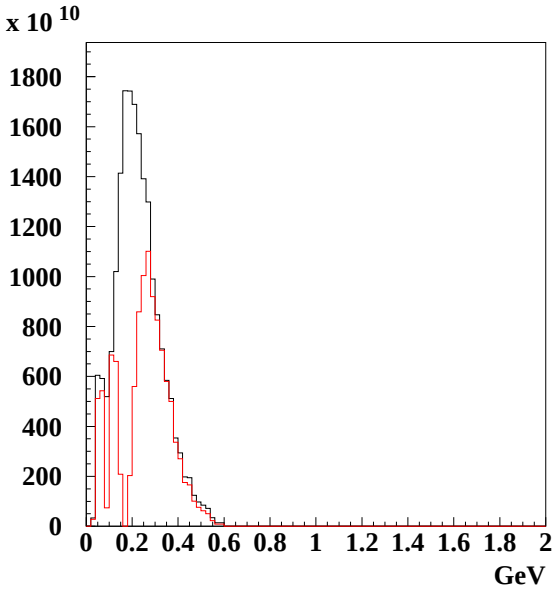


Figure 5.25: (black) Unoscillated $\bar{\nu}_\mu$ flux and (red) oscillated $\bar{\nu}_\mu \rightarrow \bar{\nu}_\tau$ flux, for a fixed length of 130 km.

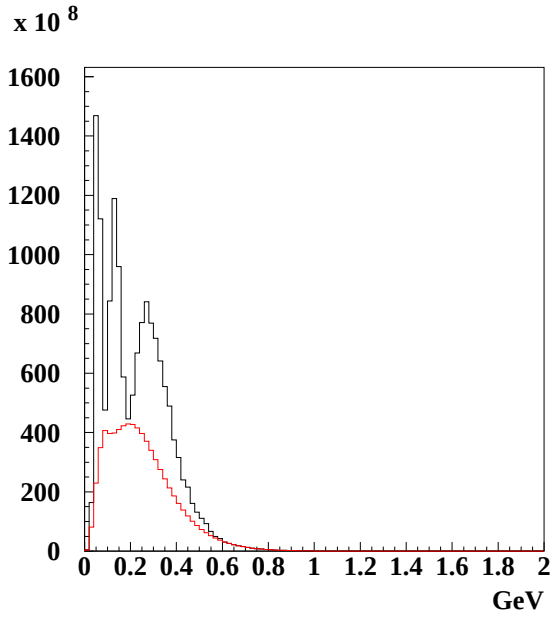


Figure 5.26: (black) Total $\bar{\nu}_e$ flux, (red) $\bar{\nu}_e$ flux from the beam, for a fixed length of 130 km.

with two different kinds of detectors, a water Cerenkov and a scintillator has been performed.
As shown in figure (5.27), the quasi elestic cross section, for low energies, can be considered in first approximation as linearly dependent from the energy.[64]

$$\sigma_\nu \simeq 0.7\,10^{-38}\left[\frac{cm^2}{nucleon}\right] \times E_\nu$$

$$\sigma_{\bar{\nu}} \simeq 0.3\,10^{-38}\left[\frac{cm^2}{nucleon}\right] \times E_{\bar{\nu}}$$

The reactions considered for this cross sections are:

$$\nu + n \rightarrow l^- + p$$
$$\bar{\nu} + p \rightarrow l^+ + n$$

Figure (5.28) shows the number of events calculated considering the rough approximation of linear cross section and a data taking of 5 years. It is

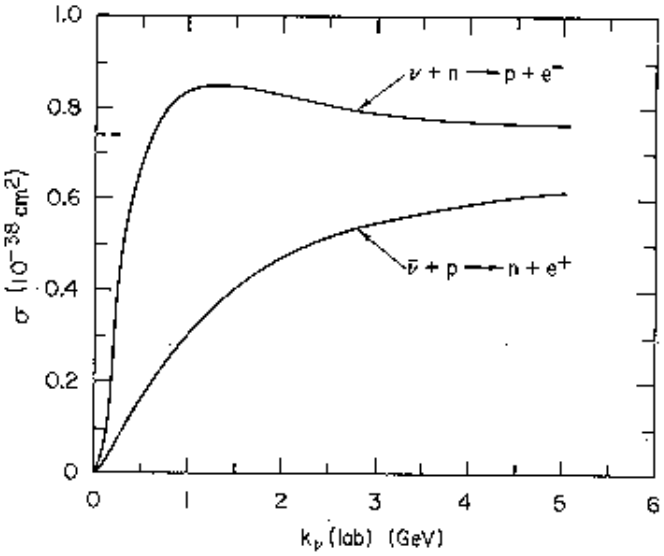


Figure 5.27: Cross section for the quasi elastic scattering for $\nu$ and $\bar{\nu}$[64]

| | total $\nu_e$ events | oscillated $\nu_e$ events | beam $\nu_e$ events |
|---|---|---|---|
| Horn focusing $\pi+$ | 40 | 20 | 20 |
| Horn focusing $\pi-$ | 10 | 5 | 5 |

Table 5.4: Events considering linear cross sections

worthwhile to notice that the cross section will smear out pronounced peaks at low energies (figure (5.28),(5.29)). The number of events is bigger than the one obtained, as will be shown, with the other two detectors. The ratio between signal ($\nu_\mu \rightarrow \nu_e$) and background ($\nu_e$ of the beam) is about 1.

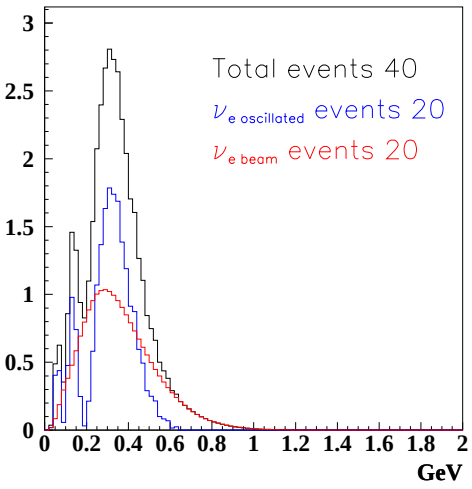


Figure 5.28: Number of events considering linear cross section for a magnetic horn focusing $\pi^+$.(black) total number of events, (blue) oscillated events, (red) beam events

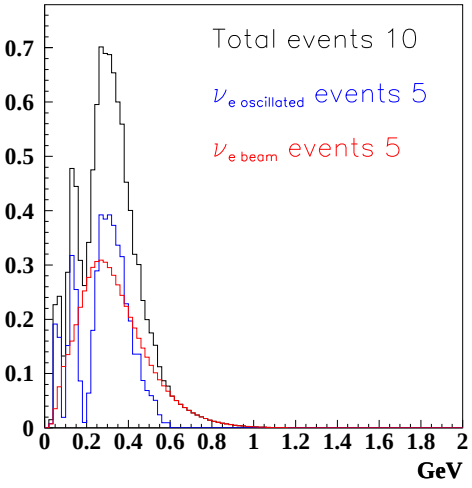


Figure 5.29: Number of events considering linear cross section for a magnetic horn focusing $\pi^-$.(black) total number of events, (blue) oscillated events, (red) beam events

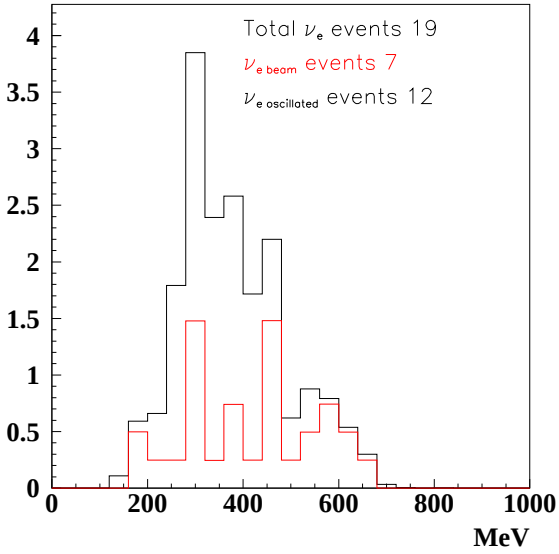


Figure 5.30: Number of events in a 40 kton water Cerenkov detector for a magnetic horn focusing $\pi^+$.(black) total number of events, (red) beam events

For a more precise evaluation of the expected number of events in the detector it is necessary to use more accurate descriptions of the neutrino interaction.
To study the water Cerenkov detector, it has been possible to use the full Super Kamiokande simulation software with a detector of 40 kton (considering the same PMT coverage as Super Kamiokande). This algorithm includes the updated neutrino cross sections, the realistic threshold on visible energy for particle detection (considering kinematic and Cerenkov thresholds and the effect of Pauli blocking) and the full data rejection procedure.
In figures (5.30)-(5.33) the number of events for the two polarities of the magnetic horn, focusing $\pi^+$ and $\pi^-$, are shown; these results are summarized in table (5.5) always for 5 years of data taking.

For the analysis of the number of events in a scintillator detector a 40 kton MiniBooNE-like detector has been considered. The dominant reactions in the scintillator are [44]:

$$\nu_e(\bar{\nu}_e) + C \rightarrow e^{\pm} + N$$

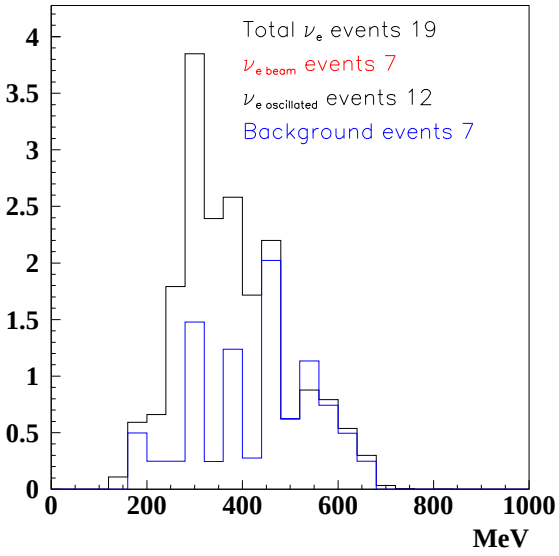


Figure 5.31: Number of events in a 40 kton water Cerenkov detector for a magnetic horn focusing $\pi^+$.(black) total number of events, (blue) background events

| | total $\nu_e$ events | oscillated $\nu_e$ events | beam $\nu_e$ events | background events |
|---|---|---|---|---|
| Horn focusing $\pi+$ | 19 | 12 | 7 | 7 |
| Horn focusing $\pi-$ | 5 | 3 | 2 | 3 |

Table 5.5: Events in a 40 kton water Cerenkov detector.

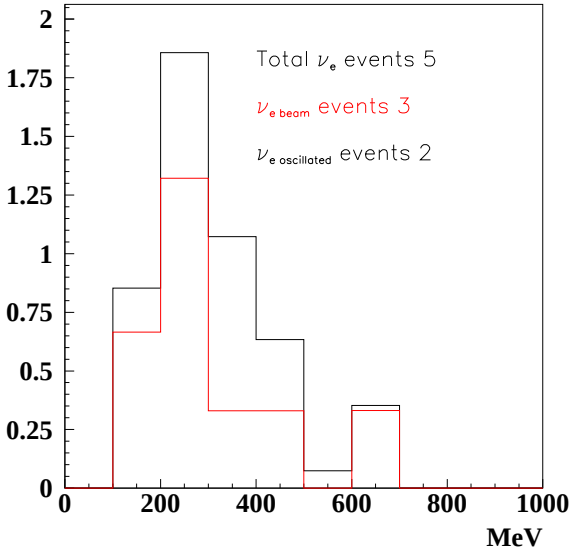


Figure 5.32: Number of events in a 40 kton water Cerenkov detector for a magnetic horn focusing $\pi^-$.(black) total number of events, (red) beam events

$$\nu_\mu(\bar{\nu}_\mu) + C \rightarrow \mu^\pm + N$$
$$\nu_\mu(\bar{\nu}_\mu) + e^- \rightarrow \nu_\mu(\bar{\nu}_\mu) + e^-$$
$$\nu_\mu(\bar{\nu}_\mu) + C \rightarrow \nu_\mu(\bar{\nu}_\mu) + \pi^0 + N$$
$$\nu_\mu(\bar{\nu}_\mu) + C \rightarrow \nu_\mu(\bar{\nu}_\mu) + \pi + N$$
$$\nu_\mu(\bar{\nu}_\mu) + C \rightarrow \mu^\pm + \pi + N$$

Interaction probability for these reactions are reported in figures (5.34),(5.35) [44].

The oscillated flux and cross sections have been used to evaluate the number of detected events for every energy bin. Figure (5.36) shows the calculated energy distribution of the oscillated $\nu_e$ together with the events coming from beam contamination. The spectrum of $\nu_\mu(\bar{\nu}_\mu) + C \rightarrow \nu_\mu(\bar{\nu}_\mu) + \pi^0 + N$ events is also shown because, as discussed above, $\pi^0$ can be confused with electron events. Figure (5.37) shows the energy distribution of events due to $\nu_\mu$ interactions before any cut to reduce backgrounds is applied. It is possible to observe that almost all the background events come from $\nu_\mu(\bar{\nu}_\mu) + C \rightarrow \mu^\pm N$. Anyway it doesn't represent a problem, because they are very well recognized

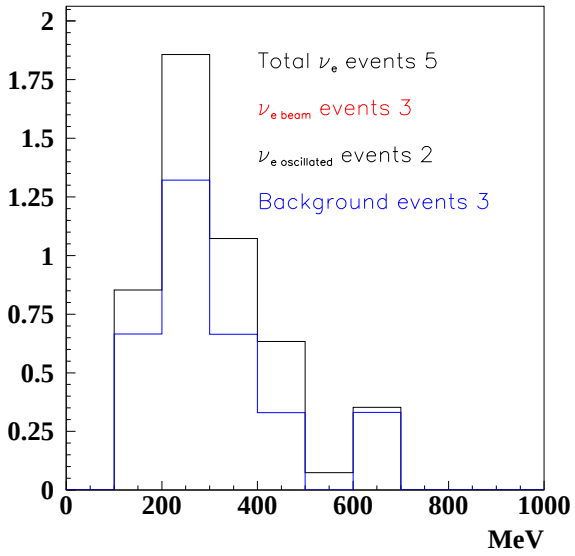


Figure 5.33: Number of events in a 40 kton water Cerenkov detector for a magnetic horn focusing $\pi^-$.(black) total number of events, (blue) background events

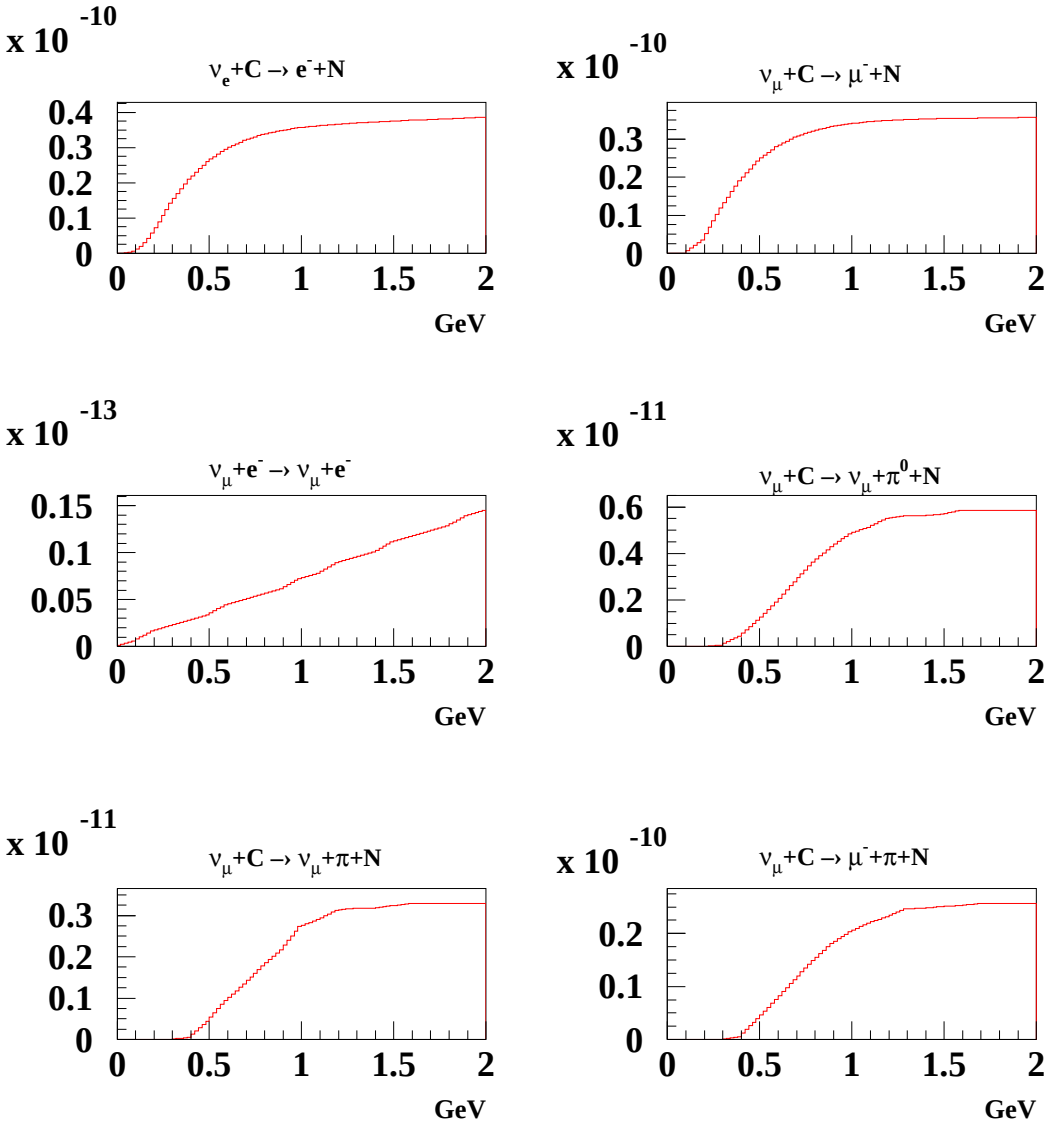


Figure 5.34: Probability of neutrino interaction in 40 kton liquid scintillator detector as funtion of neutrino energy, for different processes.

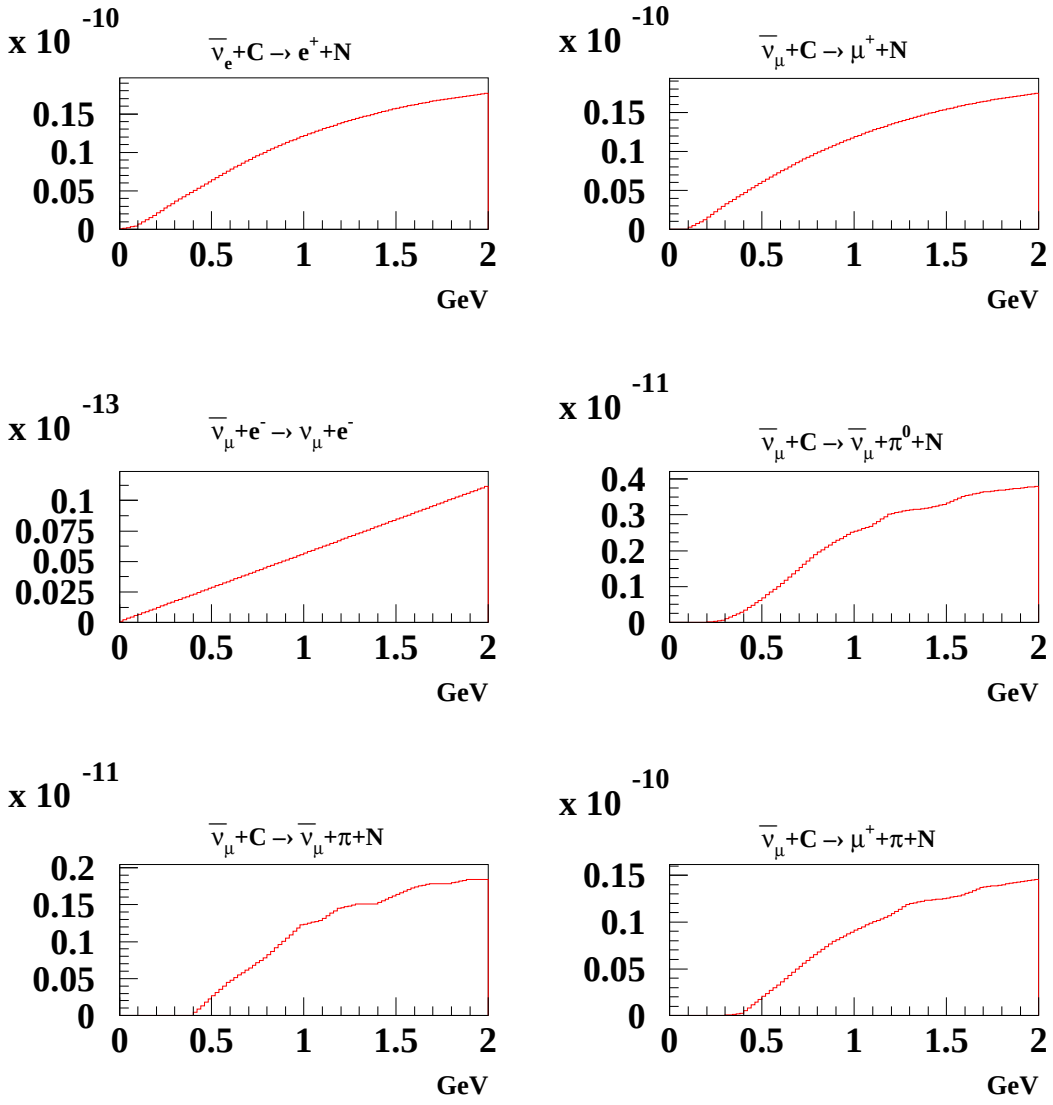


Figure 5.35: Probability of antineutrino interaction in 40 kton liquid scintillator detector as funtion of neutrino energy, for different processes.

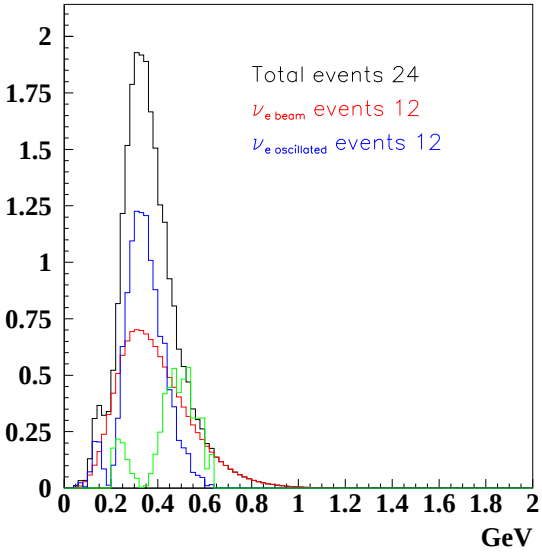


Figure 5.36: Spectrum of events in a 40 kton scintillator detector. (blue) $\nu_e$ oscillated events, (red) $\nu_e$ beam events, (black) total number of events.(green) events from $\nu_\mu + C \rightarrow \nu_\mu + \pi^0 + N$.

as $\nu_\mu(\bar{\nu}_\mu)$ events.
In table (5.6) suppression factors and signal efficiency published by the MiniBooNE collaboration are shown [44]. It is possible to observe that the suppression factor on $\nu_\mu + C \rightarrow \mu^- N$ is $10^{-3}$ and reduces considerably the number of misleading registered events. Figure (5.38) shows the event spectra for all the signal and background reactions, combined with the suppression factors. Figures (5.39)-(5.42) shows the analog results computed for a $\bar{\nu}_\mu$ beam obtained with a magnetic horn focusing $\pi^-$.
All the results are summarized in table (5.7)

It is necessary to analyze the difference in the number of events found for the three estimates. Using the linear cross section without any kind of rejection on the events is a too rough approximation of the reality. The only interesting information coming from this analysis can be an upper limit on the expected number of events.
The analysis of the water Cerenkov detector is the most accurate, because is

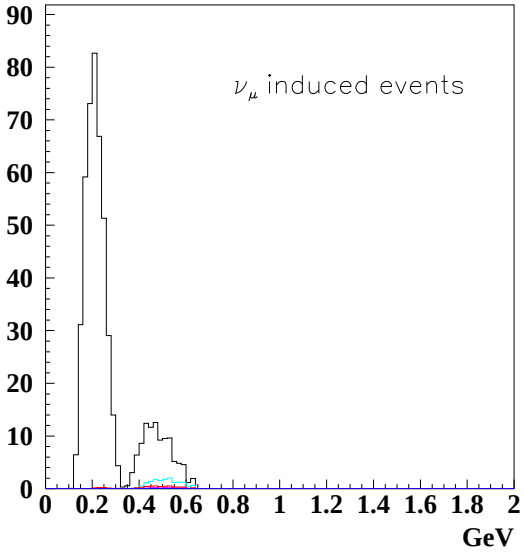


Figure 5.37: Spectrum of $\nu_\mu$ events in a 40 kton scintillator detector. (black) $\nu_\mu + C \to \mu^- + N$, (green) $\nu_\mu + C \to \nu_\mu + \pi^0 + N$, (red) $\nu_\mu + C \to \nu_\mu + \pi + N$, (blue) other events.

| Reaction | Suppression factor |
|---|---|
| $\nu_\mu(\bar{\nu_\mu}) + C \to \mu^\pm + N$ | $10^{-3}$ |
| $\nu_\mu(\bar{\nu_\mu}) + e^- \to \nu_\mu(\bar{\nu_\mu}) + e^-$ | $10^{-1}$ |
| $\nu_\mu(\bar{\nu_\mu}) + C \to \nu_\mu(\bar{\nu_\mu}) + \pi^0 + N$ | $10^{-2}$ |
| $\nu_\mu(\bar{\nu_\mu}) + C \to \nu_\mu(\bar{\nu_\mu}) + \pi + N$ | $10^{-3}$ |
| $\nu_\mu(\bar{\nu_\mu}) + C \to \mu^\pm + \pi + N$ | $10^{-4}$ |
| $\nu_e(\bar{\nu_e}) + C \to e^\pm N$ | 0.5 |

Table 5.6: Background suppression factors and signal efficiency in the MiniBooNE detector.

| | total $\nu_e$ events | oscillated $\nu_e$ events | beam $\nu_e$ events | background events |
|---|---|---|---|---|
| Horn focusing $\pi+$ | 11.9 | 5.8 | 6.1 | 0.8 |
| Horn focusing $\pi-$ | 2.4 | 1.2 | 1.2 | 0.2 |

Table 5.7: Events in a 40 kton scintillator detector.

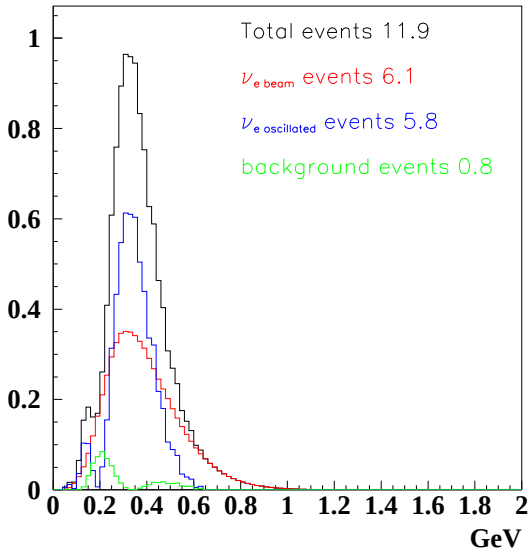


Figure 5.38: Final spectrum of events in 40 kton scintillator detector, considering suppression factors and signal efficiency. (blue) $\nu_e$ oscillated events, (red) $\nu_e$ beam events, (black) total number of $\nu_e$ events.(green) background events.

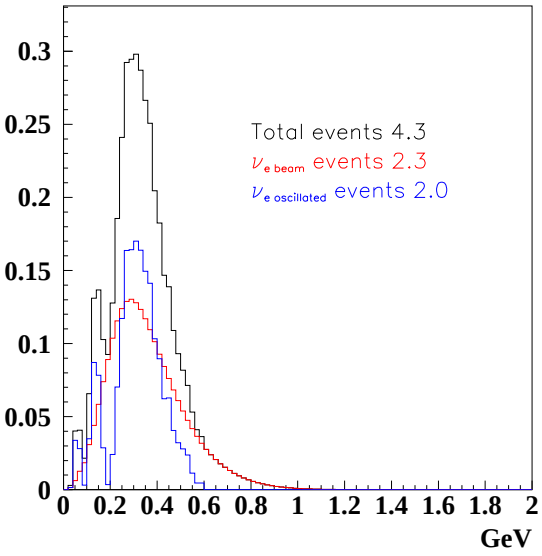


Figure 5.39: Spectrum of events in a 40 kton scintillator detector. (blue) $\bar{\nu}_e$ oscillated events, (red) $\bar{\nu}_e$ beam events, (black) total number of events.

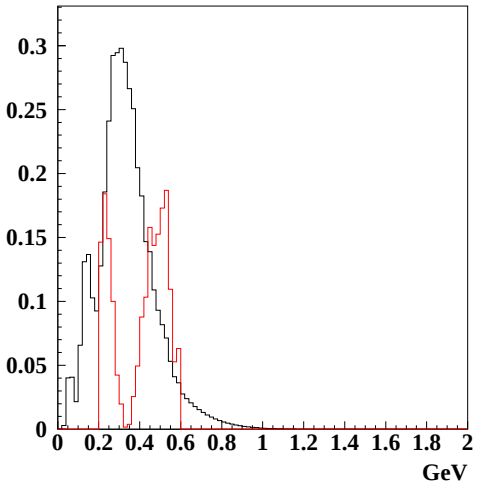


Figure 5.40: Spectrum of (red) $\bar{\nu}_\mu + C \rightarrow \bar{\nu}_\mu + \pi^0 + N$ events, (black) total number of $\bar{\nu}_e$ events, in a 40 kton scintillator detector.

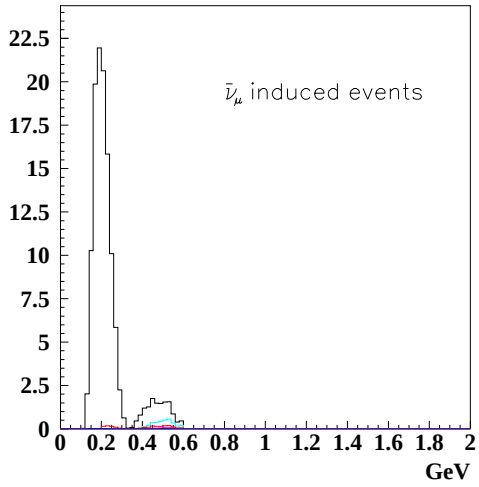


Figure 5.41: Spectrum of $\bar{\nu}_\mu$ events in a 40 kton scintillator detector. (black) $\bar{\nu}_\mu + C \rightarrow \mu^+ + N$, (green) $\bar{\nu}_\mu + C \rightarrow \bar{\nu}_\mu + \pi^0 + N$, (red) $\bar{\nu}_\mu + C \rightarrow \bar{\nu}_\mu + \pi + N$, (blue) other events

performed taking into account all the parameters for a real event analysis. In particular is the only examined estimate that take advantage of the rejection algorithm on both signal and background events.
The scintillator analysis has been performed with cross sections stated by the MiniBooNE collaboration. These values have been rescaled with the updated correcting factors the LSND collaboration has published [66], hence the description of the neutrino interaction is reasonably accurate. The main reason to justify the difference in the number of events (table (5.5),(5.7)) is again the lack of the full simulation.
The final result of this analysis is that a 40 kton detector based on water Cerenkov light or scintillation detection can suit the necessity of this experiment.

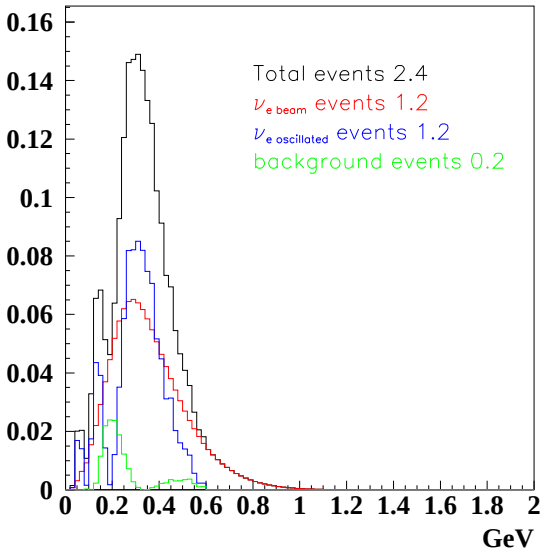


Figure 5.42: Final spectrum of events in 40 kton scintillator detector, considering suppression factors and signal efficiency. (blue) $\bar{\nu}_e$ oscillated events, (red) $\bar{\nu}_e$ beam events, (black) total number of $\bar{\nu}_e$ events, (green) background events

# Chapter 6

# Sensitivity on $\theta_{13}$

The sensitivity of this experiment in the measurement of $\theta_{13}$ has been evaluated considering the beam configuration with a decay tunnel of 20 m length and 1 m radius and a 40 kton water Cerenkov detector located at 130 km with a data taking of 5 years (1 year of data taking corresponding to $10^7 s$). As explained in the previous chapter no significant discrepancy in the final number of events can be observed using a water Cerenkov detector instead of a scintillator. However, the water Cerenkov is considered here because the events analysis performed on it is the most accurate.

## 6.1 The likelihood method

In the search for neutrino oscillation evidence, the likelihood method is generally used to establish either a non zero mixing angle or mass difference, with adequate statistical significance or, in case of no evidence for oscillations, set an upper limit on the considered parameters. The general statement of the problem is the following: the observed number of neutrino interaction is compared with the expected number computed using a model for the oscillations; the expected number must also include an estimate of the number of background events expected; the model describing the oscillations involves a certain number of parameters; as shown in the second chapter, there are three mixing angles, three mass differences and a phase $\delta$ for CP violation; hence a statistical method is required to find the parameters that best fit the experimental data.
The maximum likelihood method is generally used to extract parameters

from experimental data. Suppose to have an energy interval divided into a collection of N bins. Let $n_i$ be the number of events in the bin i ($i = 1, ..., n$). Suppose to have a fitting function F, depending on a set of m parameters $(a_1, ..., a_m)$. For the neutrino problem F is a function composed by the product of two terms: one built with the knowledge about neutrino flux and interactions in the detector and a second one based on the neutrino oscillation model, depending on the previous parameters. The object of the analysis is to find the values of the parameters that best fit the data distribution. To do this for each energy bin it is necessary to convert the function F into a normalized distribution probability:

$$P_i = P(n_i; a_1, ...a_m)$$

Neutrino experiments belongs to the class of the counting experiments and the distribution probability is poissonian,

$$P(\mu_i, n_i) = \frac{e^{-\mu_i}\,\mu_i^{n_i}}{n_i!}$$

where $\mu_i$ is the mean expected number of events assuming neutrino oscillations and $n_i$ is the number of measured events. The mean values $\mu_i$ are function of the oscillation parameters, hence $P_i$ is more properly written as

$$P_i = P(\mu_i, n_i) = P(n_i; a_1, ...a_m)$$

The likelihood function is generally defined as the product of the individual probability densities:

$$\mathcal{L}(a_1, ..a_m) = \prod_{i=1}^{N} P_i$$

The aim is to find the best set of parameters that maximize this function. Because the probability of observing a particular number of events is a number less than 1, the product of a large number of such probabilities in the likelihood can be a very small number and, using a computer to analyze this function, can lead to accuracy problems. To avoid this kind of problems is usually preferable to maximize the logarithm of the likelihood:

$$M = \log \mathcal{L} = \chi^2$$

(In the case of gaussian distributed data a similar definition leads to the usual definition of $\chi^2$.)

In the considered neutrino experiment the number of events for each bin is very small, hence the total number of events has been decided to study as an unbinned distribution disregarding the energy spectrum.
In this circumstance the log-likelihood assumes this particular expression [57]:

$$\chi^2 = 2(N_{th} - N_{obs}) + 2N_{obs}\log(\frac{N_{obs}}{N_{th}})$$

where $N_{th}$ is the number of expected neutrinos considering oscillations and $N_{obs}$ is the number of observed neutrinos without oscillations.

## 6.2 Oscillation parameter $\theta_{13}$

The sensitivity of this experiment is bounded by statistical and systematic errors.
Statistical errors can be easily accounted for using the Poisson fluctuations of the events coming from oscillated $\nu_e$, beam contamination $\nu_e$, and background.
Systematic errors are very difficult to analyze and in this study it has been possible only to give an approximate estimation. The dominant systematic errors will come from the uncertainties in the pion beam study and in the detector study, for the latter mainly coming from neutrino cross sections and background rejection. For the evaluation of the systematic errors on the beam in this experiment the values coming from the experience of the MiniBooNE collaboration has been considered stating an $\epsilon_{syst}$ of 10% as conservative and 5% as possible [44]. MiniBooNE use the neutrino beam coming from the FNAL (Fermi National Accelerator Center) Booster. In that setup $\nu_\mu$ come from the decay of the pions while the primary background due to $\nu_e$ comes also from kaons. When the ratio $\nu_\mu/\nu_e$ is considered systematic errors of the two fluxes don't disappear. Hence it is necessary to take into account the $k/\pi$ ratio predicted by the MC simulation in final neutrino fluxes estimate.
At the energy of the SPL (2.2 GeV), kaon production is almost totally suppressed, $\nu_\mu$ and $\nu_e$ come from the same production chain of the pion-muon decay, hence systematic errors on the ratio $\nu_\mu/\nu_e$ in the final neutrino flux cancel each other. An important consideration is that in the next years will be available the $\pi$ production cross section measured by HARP [67] down to a precision of few %. The present errors on these cross sections at the SPL energy are approximatively 30-40%.

The systematic errors on the considered water Cerenkov detector can be monitored only using a near detector having the task to measure $\nu_e$ fluxes, neutrino cross sections and the effective detector efficiency.
With these considerations a reasonable estimate of the systematic errors should lead to 5% as conservative and 2% as possible.
Sensitivity is usually defined [68] as:

$$S = \frac{N_{osc}}{\sqrt{N_{osc} + N_{beam} + N_{bkg} + ((N_{osc} + N_{beam}) * \epsilon_{syst})^2}}$$

where $N_{osc}$ is the number of events coming from oscillated neutrinos, $N_{beam}$ is the number of events coming from the $\nu_e$ initial contamination of the beam, $N_{bkg}$ are background events and $\epsilon_{syst}$ is the systematic error.
Considering as explained in the first chapter the LMA (Large Mixing Angle) solutions $\sin^2(2\theta_{12}) = 0.8$, $\sin^2(2\theta_{23}) = 1$, $\sin^2(2\theta_{13}) = 0.01$, $\delta m^2_{12} = 5\,10^{-5}\,eV^2$, $\delta m^2_{23} = 3.2\,10^{-3}\,eV^2$ and the usual decay tunnel detector setup, the number of events can be read from the previous chapter: 12 oscillated events, 7 beam events and 7 background events. With this values and $\epsilon_{syst} = 2\%$, the sensitivity is S=2.5. The standard way to improve this number is to select an energy window to cut part of the background but in the considered case there is no significant energy separation between signal and background.
The sensitivity study on oscillations parameters is usually performed in terms of exclusion plots. The exclusion line is a level curve on the likelihood function at a certain value of confidence level. Usually in these plots are displayed the 90% and 95% confidence level curves. The meaning of the exclusion plot is that for all the points $(\sin^2(2\theta), \delta m^2)$ on the right of the exclusion line in the parameters plane, it is possible to say that can be excluded as true values of the parameters with a certain confidence level. The relevant parameters in the probability oscillation $p(\nu_\mu \to \nu_e)$ are the mixing angle $\theta_{13}$ and the mass difference $\delta m^2_{23}$ then the $\chi^2$ function is defined with 2 degree of freedom. The plot in figure (6.1) is calculated assuming the normal $\chi^2$ probability distribution.
It is possible to observe that the 90% C.L. plot extends down to $\sin^2(2\theta_{13}) \geq 4\,10^{-3}$ and the 95% C.L. extends down to $\sin^2(2\theta_{13}) \geq 6\,10^{-3}$, to be compared with the present limit on the measurement of $\sin^2(2\theta_{13})$ coming from CHOOZ. This experiment has been briefly described in the first chapter. The final CHOOZ analysis [39] state the exclusion plot in figure (6.2). In this plot the 90% C.L. extends down to $\sin^2(2\theta_{13}) \geq 2\,10^{-2}$ and the 95% C.L.

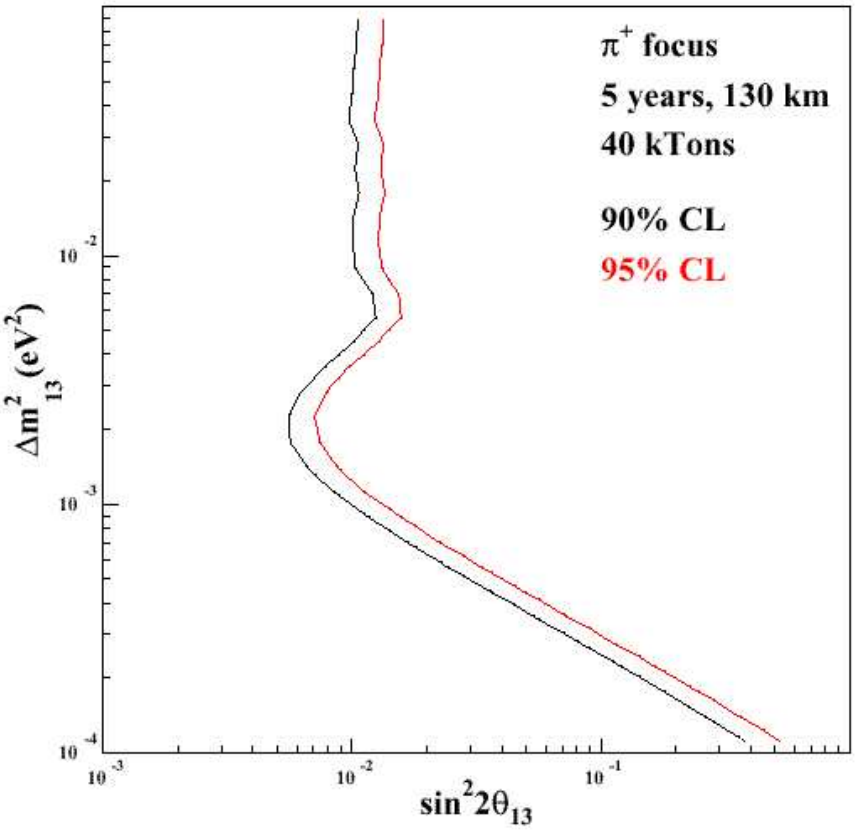


Figure 6.1: Exclusion plot produced considering the usual beam configuration with a decay tunnel of 20 m length and 100 cm radius and a 40 kton water Cerenkov detector located at 130 km with data taking of 5 years (1 year corresponding to $10^7 s$)

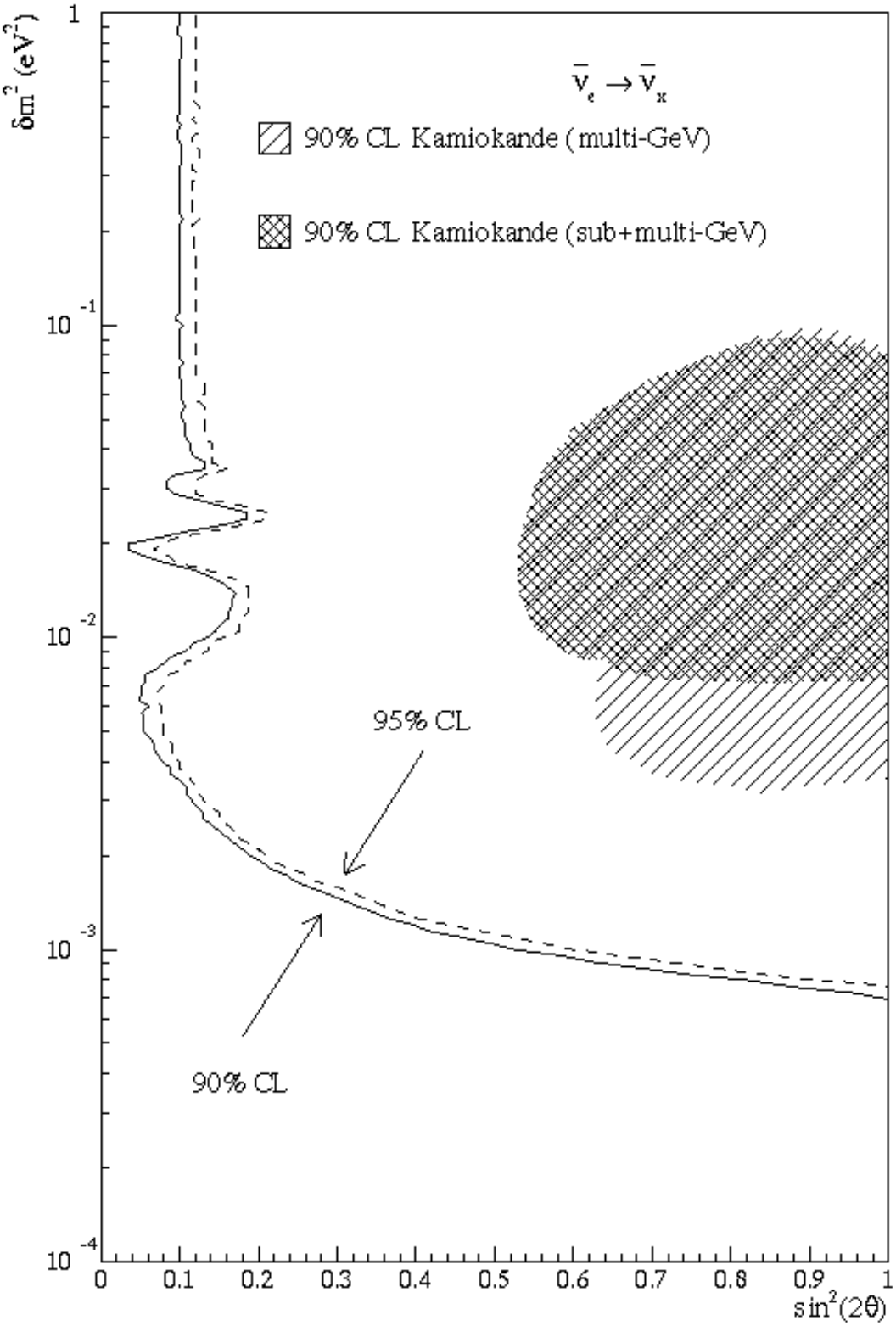


Figure 6.2: CHOOZ Exclusion plot.[39]

extends down to $\sin^2(2\theta_{13}) \geq 6\,10^{-2}$. Comparing the two exclusion plots, it is possible to observe an improvement on $\sin^2(2\theta_{13})$ sensitivity by almost one order of magnitude.

# Chapter 7

# Conclusions

The potentiality of the SPL-based neutrino superbeam has been investigated. Neutrino fluxes have been studied considering the SPL as proton source. Proton kinetic energy from this accelerator is 2.2 GeV with a rate of $10^{23}$ pot/year (pot: protons on target). For the pion production the considered target is a mercury jet with a length of 26 cm ($\sim$ 2 interaction lengths) and a radius of 0.75 cm. At this energy kaon production is almost completely suppressed.
The simulated magnetic horn is that studied for the Neutrino Factory which is probably not the best choice for this superbeam application. In fact the considered horn has a point to point optics while it would be better to consider a point to parallel one. Flux calculations, which is the main part of this study, have been performed analytically studying the decay probability distribution of pions and subsequent muons. A FORTRAN program has been implemented for calculations. Only pions coming from the horn have been considered. Only a small number of muons have been found at the end of the horn. They come from low energy pion decayed during the focusing process and, since they are at very low energy too, they have been neglected.
Particular attention has been payed on the decay tunnel geometry because is the only tool to define the beam purity. The decay tunnel configuration has been studied systematically producing fluxes for a big set of geometry parameters. The best choice has been found in a cylindrical shape of 20 meters length and 1 meter radius. No significative energy difference between $\nu_\mu$ from pions and $\nu_e$ from muons varying the decay tunnel geometry has been found, hence it is not possible to think about energy cuts on the pion beam to improve the purity of the final neutrino beam. No significant difference

have been observed in the best configuration for a decay tunnel used for $\pi^+$ or $\pi^-$ beam. The optimization lead to a ratio between the number of $\nu_e$ and $\nu_\mu$ of the superbeam equal to about 0.35% for both polarities of the horn.
The total flux in a detector of $10 \times 10\, m^2$ at 130 km considering $10^{23}$ pot (1 year of SPL run) is $6.5\, 10^{13}$ $\nu_\mu$ and $2.3\, 10^{11}$ $\nu_e$ with a horn focusing $\pi^+$ and $4.32\, 10^{13}$ $\bar{\nu}_\mu$ and $1.6\, 10^{11}$ $\bar{\nu}_e$ with a horn focusing $\pi^-$. The mean energy of the neutrino beam, in the optimal configuration for the decay tunnel, is about 250 MeV.
The aim of this experiment is to observe $\nu_\mu \rightarrow \nu_e$ oscillations, hence the position of the detector plays an important role for two reasons: neutrino flux decreases with the square of the distance from the production point and also the oscillation probability changes with the distance. The possible location has to be chosen near an oscillation probability peak and in a place where a neutrino laboratory already exists. The suggested detector position is at LSM (Laboratoire Souterrain de Modane) which is 130 km away from the decay tunnel and near the first oscillation peak for a mean energy of 250 MeV. The detector analysis has been performed neglecting costs but anyway attention has been payed not to propose impossible solutions. The mass of the detector has been chosen in 40 kton which permits to obtain enough statistics considering a reasonable data taking period of 5 years.
The detector study has been performed on a scintillator MiniBoone-like detector and on a water Cerenkov Super Kamiokande-like. For the first a reasonable estimations of the number of events and background rejection has been given considering the estimates published in the MiniBooNE proposal. For the water Cerenkov detector the full Super Kamiokande simulation has been used, hence with an extremely precise analysis of events reconstruction and background rejection. The number of observed events are 12 oscillated events for water Cerenkov and 6 for the scintillator, 7 beam events for the water Cerenkov and 6 for the scintillator and 7 background events in the water Cerenkov and 1 for the scintillator. The number of events for antineutrinos are considerably smaller due to the lower flux and cross sections. The comparison between the two detectors can be done taking into account that for the scintillator a full simulation has not been done. Anyway with these considerations, it is possible to observe that data doesn't show any large discrepancy in the final number of events, hence both detectors can suit the requirement of this experiment.
The study of $\theta_{13}$ as been performed with the horn focusing $\pi^+$ because it permits to obtain neutrinos instead of antineutrinos that have larger cross

sections and then a larger number of events. The analysis has been performed with the likelihood method and expressed in the usual form of an exclusion plot. The final results show a sensitivity on $\sin^2(2\theta_{13})$ down to 0.004 at the 90% confidence level and 0.006 at 95% confidence level, for $1\,10^{-3} \leq \delta m^2_{23} \leq 2\,10^{-3} eV^2$. In this $\delta m^2_{23}$ range the present limit on $\sin^2(2\theta_{13})$ comes from the CHOOZ experiment which has published the final analysis with 0.02 at 90% of confidence level, hence with this experiment there could be an improvement of about one order of magnitude in sensitivity.
The present study will be followed by a number of other investigations on different aspects of the superbeam.
The target is still developing and it is possible to imagine an improvement on the number of produced pion per proton. The horn geometry will be optimized for this experiment considering a point to parallel optics. Anyway the major uncertainty in the final neutrino flux remains in the hadron cross sections at these energies, which is under investigation with the HARP experiment.
Great attention will be devoted to the study of the oscillation parameters, particularly the phase $\delta$ for the CP violation. In fact the big advantage in the use of a magnetic horn is that this device is charge selective, hence changing the polarity of the current it is possible to switch from a neutrino beam to an antineutrino beam. Considering

$$\frac{P(\nu_\mu \rightarrow \nu_e) - P(\bar{\nu}_\mu \rightarrow \ \bar{\nu}_e)}{P(\nu_\mu \rightarrow \nu_e) + P(\bar{\nu}_\mu \rightarrow \bar{\nu}_e)}$$

it is possible to investigate CP violation in the leptonic sector. For this study will be necessary a deeper understanding of the systematic errors on pion production, on neutrino cross sections at these energies and on the detector effects.

# Appendix A

# Flux program

```
c ***********************************************************************
c                            NEUTRINO FLUXES
c
c ***********************************************************************

c Number of bins in neutrino's energy
      parameter (nbine=100)

c Data types
      real*8 ProbnmP(nbine)
      real*8 ProbamP(nbine)
      real*8 Probne(nbine)
      real*8 Probnm(nbine)
      real*8 Probae(nbine)
      real*8 Probam(nbine)
      real*8 P(3)
      real*8 ex(3)
      real*8 ey(3)
      real*8 ez(3)
      real*8 w(3)
      real*8 ux(3)
      real*8 uy(3)
      real*8 uz(3)
      real*8 xpion(3)
      real*8 pmupi(3)
```

```
      real*8 pmuvet(3)
      real*8 punit(3)
      real*8 null(3)
      real qrndm
      real*8 Mmu,Mpi,al,de
      real*8 Ppi,d,pi,emustr,pmustr,dfi,dcstsm
      real*8 geomp,geome,geomm
      real*8 x,y,z,px,py,pz,et,ctoff,www
      real*8 epi,betapi,gammap,ca,sa,enustr,enup,prb
      real*8 cststm,emu,pmul,pmut,pmu,sntstr,betamu,cosr
      real*8 ctsn,dprobe,dprobm,enu,a,probdkpi,probdkmu
      real*8 costante,tl,tr,cstzero,fi,fizero,enuzero
      integer nfile,npions
      real*8 dum
      real*8 gammamu,MupolT,MupolL,costheta
      real*8 nmuons(nbine)
      integer ntotmuons
      real*8 threshold
      integer muonp,muonm

c Initialize probabilities arrays to zero
      do 39 i=1,nbine
         ProbnmP(i)=0.d0
         ProbamP(i)=0.d0
         Probne(i) =0.d0
         Probnm(i) =0.d0
         Probae(i) =0.d0
         Probam(i) =0.d0
         nmuons(i) =0.d0
39    continue

       do 20 i=1,3
         P(i)     =0.d0
         null(i)  =0.d0
         w(i)     =0.d0
         ux(i)    =0.d0
         uy(i)    =0.d0
         uz(i)    =0.d0
```

```
         xpion(i) =0.d0
         pmupi(i) =0.d0
         pmuvet(i)=0.d0
         punit(i) =0.d0
         null(i)  =0.d0
 20   continue

      ntotmuons=0

c Averaged muon polarization variables
      sumpolp=0.d0
      sumpolm=0.d0
      muonp=0
      muonm=0

c ********************************************************************
c System constants:

c Distance tunnel decay, detector (in m)
      d=50000.d0

c Side of the detector (in m)
      al=10.d0

c Tunnel radius and length (in cm)
      tl=2000.d0
      tr=100.d0

c ********************************************************************

c Input file
      nfile=93

c Number of pions in the file
      npions=999995

c Errors file:
c      open(UNIT=2,FILE='errors.20',STATUS='UNKNOWN')
```

```
c      write(2,*)'This file contains the "errors" of the computation'

c      open(UNIT=4,FILE='pol100-.20',STATUS='UNKNOWN')

c Greek Pi
      Pi=acos(-1.d0)

c Pion and muon's mass
      Mpi=0.13956995d0
      Mmu=0.105658389d0

c Energy and momentum of the muon in the centre of mass of the pion
      emustr=(mpi**2+mmu**2)/(2.d0*mpi)
      pmustr=(mpi**2-mmu**2)/(2.d0*mpi)

c Bins
c Number of bins in fi and in cos theta star:
      nbinfi=12
      nbcst=20

c Dimensions of the bins:
      dfi=2.d0*Pi/nbinfi
      dcstsm=2.d0/nbcst
      de=2.d0/nbine

c Versor: ez (direction tunnel decay detector)
      ez(1)=0.d0
      ez(2)=0.d0
      ez(3)=1.d0

c Normalization + useful constants (these are some costants that
c appear in the formulas so I calculate once here)
      geomp=(1/(4.d0*Pi))*((al**2)/(d**2))
      geome=de*((3.d0/Pi)*(al**2)*(1.d0/(d**2)))/(nbcst*nbinfi)
      geomm=de*((1.d0/(2.d0*Pi))*(al**2)*(1.d0/(d**2)))/(nbcst*nbinfi)

c Read Pion datas
```

```
c m is just a counter
      m=0

c ni is the number of the event in the Monte Carlo simulation
      ni=0
      do while (ni.lt.npions)
         read (nfile,*)ni,jp,x,y,z,px,py,pz,et,ctoff,www

c Check if the the particle is a pion + (jp=3) or a pion - (jp=4).
c If it is not go to next pion
         if ((jp.ne.3).and.(jp.ne.4)) goto 1234

c Increase the pion counter
         m=m+1

c Initial position of the pion (z=0)
         if (x.gt.tr) then
c            write(2,*)'Pion #:',m,'events',ni,'has x > tunnel radius'
            goto 1234
         endif

         if (y.gt.tr) then
c            write(2,*)'Pion #:',m,'events',ni,'has y > tunnel radius'
            goto 1234
         endif

         xpion(1)=x
         xpion(2)=y
         xpion(3)=0.d0

c Initial momentum of the pion (lab frame)
         P(1)=Px
         P(2)=Py
         P(3)=Pz

c Momentum, energy, beta, gamma of the pion
         Ppi=dsqrt(Px**2+Py**2+Pz**2)
         epi=et
```

```
         Betapi=ppi/epi
         Gammap=epi/mpi

c If the pion is at rest, ignore it
         call dvmod(p,3,dum)
         if (dum.eq.0.d0) then
c            write(2,*)'Pion #:',m,'events',ni,'is at rest'
            goto 1234
         endif

c Normalize the pion momentum
         call dvunit(p,uz,3)

c Create the pion frame
         call dcross(ez,uz,uy)
         call dvunit(uy,w,3)
         call ducopy(w,uy,3)
         call ducopy(uy,ey,3)

c Checks if the direction uz of the pion is parallel to ez (i.e.uy=0)
         call dvmod(uy,3,dum)
         if (dum.eq.0.d0) then
c            write(2,*)'Pion #:',m,'events',ni,'uz is parallel to ez '
            uy(1)=0.d0
            uy(2)=1.d0
            uy(3)=0.d0
            ey(1)=0.d0
            ey(2)=1.d0
            ey(3)=0.d0
          end if

c Pion frame
         call dcross(uy,uz,ux)
         call dvunit(ux,w,3)
         call ducopy(w,ux,3)

c Lab frame
         call dcross(ey,ez,ex)
```

```
          call dvunit(ex,w,3)
          call ducopy(w,ex,3)


c Neutrinos from the Pions
c To go into the detector the neutrino must have an angle in the lab
c equal to the Pion angle (lab frame)

c Angle from the neutrino trajectory and the ez axis of the lab
          ca=(pz/ppi)
          sa=dsqrt(1.d0-ca**2)

c Energy of the neutrino in the center of mass of the pion (2 body
c decay so the energy is fixed)
c         enustr=.0297917
          enustr=(mpi**2-mmu**2)/(2.d0*mpi)

c Boost of the energy from the pion frame to the lab frame
         enup=gammap*enustr*(1.d0+betapi*((betapi-ca)/(betapi*ca-1.d0)))

c Calculate the number of the bin occupated by the neutrino (lab frame)
          iep=int(enup/de)+1

c Decay tunnel effect
          probdkpi=0.d0
          call probdkm(tl,tr,p,xpion,null,probdkpi,probdkmu,1)

c Calculates the probability to reach the detector
          prb=geomp*((1.d0-(betapi**2))/(betapi*ca-1.d0)**2)*probdkpi

c Put the probability (like a weight) in the right bin of energy
          if (jp.eq.3) probnmP(iep)=probnmP(iep)+prb
          if (jp.eq.4) probamP(iep)=probamP(iep)+prb

c Muons from the pion
c To calculate the probability I sample the sphere in
c cos(theta star), fi
```

```
c I generate a random number to start cos theta star this should avoid
c big statistical errors
         cstzero=(2.d0*rndm(qrndm))/nbcst

c Loop in cos theta star (pion decay)
         do 50 ibcst=1,nbcst
            cststm=-1.d0+cstzero+(ibcst-1)*dcstsm

c Muon's energy in the lab frame (depends on cos theta star)
            Emu=Gammap*Emustr+Betapi*Gammap*Pmustr*cststm

c Longitudinal momentum
            Pmul=Betapi*Gammap*Emustr+Gammap*Pmustr*cststm

            sntstr=dsqrt(dabs(1.d0-(cststm**2)))

c Transverse momentum (obviously no boost)
            Pmut=Pmustr*sntstr
            Pmu=dsqrt(Pmul**2+Pmut**2)
            betamu=Pmu/Emu
            gammamu=emu/mmu

c Muon Polarization
            MupolT=((gammap*betapi)/(gammamu*betamu))*sntstr

            threshold=-(pmustr/(betapi*emustr))

c Sign of longitudinal polarization
            MupolL=dsqrt(1.d0-(MupolT**2))

c For mu+
            if ((jp.eq.3).and.(cststm.gt.threshold)) MupolL=-MupolL
            if ((jp.eq.3).and.(cststm.lt.threshold)) MupolL=MupolL
c For mu-
            if ((jp.eq.4).and.(cststm.gt.threshold)) MupolL=MupolL
            if ((jp.eq.4).and.(cststm.lt.threshold)) MupolL=-MupolL

c I generate a random number for the start of fi this should avoid
```

```
c big statistical errors
            fizero=2.d0*Pi*rndm(qrndm)

c LOOP IN FI
            do 70 ifi=1,nbinfi
               fi=(ifi-1)*dfi+fizero

c Fi is periodic of 2*Pi
               if (fi.gt.2.d0*Pi) fi=fi-2.d0*Pi

c Muon momentum in the boosted frame (lab frame) but with axis
c parallels to pion axis
               pmupi(1)=pmut*cos(fi)
               pmupi(2)=pmut*sin(fi)
               pmupi(3)=pmul

c Muon momentum in the decay tunnel - detector frame (lab frame) with
c the correct axis
               pmuvet(1)=pmupi(1)*ux(1)+pmupi(2)*uy(1)+pmupi(3)*uz(1)
               pmuvet(2)=pmupi(1)*ux(2)+pmupi(2)*uy(2)+pmupi(3)*uz(2)
               pmuvet(3)=pmupi(1)*ux(3)+pmupi(2)*uy(3)+pmupi(3)*uz(3)

c Tunnel Decay effect
               probdkmu=0.d0
               call probdkm(tl,tr,p,xpion,pmuvet,probdkpi,probdkmu,2)

c The neutrino angle
               call dvunit(pmuvet,punit,3)
               call dvdot(punit,ez,3,cosr)

c The same angle in the muon frame (muon decay)
               ctsn=(betamu-cosr)/((betamu*cosr)-1.d0)

c Angle between the neutrino momentum vector and muon direction
               costheta=ctsn

c Number of occupated bins
               nboc=int(Emu/de)+1
```

```
c I generate a random number for enu's middle of the bin
               enuzero=rndm(qrndm)

c LOOP IN NEUTRINO ENERGY
               ie=0
               do 60 ie=1,nboc
                  dprobe=0.d0
                  dprobm=0.d0
                  enu=emu-((ie-enuzero)*de)

c FORMULAS
c This is just to semplify the formula
                  a=(2.d0*enu/emu)*(1.d0/(1.d0+betamu*ctsn))

                  if (a.gt.1.d0) then
c                     write(2,*)'Pion #:',m,'event:',ni,
c     +                   'MU cos(theta*)=',cststm,'fi=',fi,'Enu*',enu,
c     +                   '"a">1'
                     goto 60
                  endif
                  if (a.lt.0.d0) then
c                     write(2,*)'Pion #:',m,'event:',ni,
c     +                   'MU cos(theta*)=',cststm,'fi=',fi,'Enu*',enu,
c     +                   '"a"<0'
                     goto 60
                  endif

c Formulas without Polarization
c          dprobe=geome*(a**2-a**3)*(a/enu)*((1.d0-(betamu**2))/
c     +           ((betamu*cosr-1.d0)**2))*probdkmu

c          dprobm=geomm*(3.d0*a**2-2.d0*a**3)*(a/enu)*
c     +           ((1.d0-(betamu**2))/((betamu*cosr-1.d0)**2))*probdkmu

c Formulas with Polarization

          if (jp.eq.3) then
```

```
            dprobe=geome*((a**2-a**3)-(MupolL*(a**2-a**3)*costheta))*
     +   (a/enu)*((1.d0-(betamu**2))/((betamu*cosr-1.d0)**2))*probdkmu

            dprobm=geomm*((3.d0*a**2-2.d0*a**3)-
     +            (MupolL*(a**2-2.d0*a**3)*costheta))*(a/enu)*
     +            ((1.d0-(betamu**2))/((betamu*cosr-1.d0)**2))*probdkmu
          endif

          if (jp.eq.4) then

            dprobe=geome*((a**2-a**3)+(MupolL*(a**2-a**3)*costheta))*
     +    (a/enu)*((1.d0-(betamu**2))/((betamu*cosr-1.d0)**2))*probdkmu

            dprobm=geomm*((3.d0*a**2-2.d0*a**3)+
     +            (MupolL*(a**2-2.d0*a**3)*costheta))*(a/enu)*
     +            ((1.d0-(betamu**2))/((betamu*cosr-1.d0)**2))*probdkmu
          endif


c Put the probability in the right energy bin
            if (jp.eq.3) then
                Probne(nboc-ie+1)=Probne(nboc-ie+1)+dprobe
                Probam(nboc-ie+1)=Probam(nboc-ie+1)+dprobm
               end if

            if (jp.eq.4) then
                Probae(nboc-ie+1)=Probae(nboc-ie+1)+dprobe
                Probnm(nboc-ie+1)=Probnm(nboc-ie+1)+dprobm
               end if

60            continue
c End loop in neutrino energy


70        continue
c End loop in fi
```

```
50    continue
c End loop in cos theta star

c On-line output
      write(*,*)m,ni

1234  end do
c End of the main loop


c Costant (normalization) to transform probability into fluxes
c
c 10^(16-6+7)
c
c 10^16 protons/second
c 10^6 protons to produce pions
c 10^7 second/year
      costante=1.d17

c OUTPUT
      write(*,*)'Writing output files'
      open(UNIT=1,FILE='fluxpol100+.20',STATUS='UNKNOWN')
      open(UNIT=3,FILE='muondistr100+.20',STATUS='UNKNOWN')
      do 300 ie=1,nbine
        write(1,*)ie,(ie*de),probnmP(ie)*costante,probamP(ie)*costante,
     +probne(ie)*costante,probam(ie)*costante,probae(ie)*costante,
     +probnm(ie)*costante
        write(3,*)(ie*de),nmuons(ie)
300     continue

        close(UNIT=1)
        close(UNIT=3)

      write(*,*)'END!'
c

c Close error file
```

```
c      close(UNIT=2)

100   end



c Calculates muon and pion decay probabilities for a pi->mu  decay
c in a tunnel of length z0 and radius r0
c if idptc=1 looks only at the pion
c Coordinates in the lab frame.
c--------------------------------------------------------------------
       subroutine probdkm
     +(tunnel_length,tunnel_radius,ppi,xpi,pmu,probpi,probmu,idptc)
c--------------------------------------------------------------------
       real*8 tunnel_length,tunnel_radius
       real*8 dprobmu
       real*8 ppi(3),xpi(3),xpin(3),pmu(3),upi(3),umu(3)
       real*8 ampi,ammu,ctpi,ctmu,appi,apmu,path0pi,path0mu
       real*8 probpi,probmu,ap,param,r0,z0,pathpi,bp,cp,xfin,yfin,zfin
       real*8 dl,a,b,c,pat,xmufin,ymufin,zmufin,tlambda,pathmu
       integer nsteps,idptc

c  Units are cm and GeV.

        ampi=0.13956995d0
        ammu=0.105658398d0
        ctpi=780.45d0
        ctmu=65865.d0

        r0= tunnel_radius
        z0= tunnel_length

        call dvmod(ppi,3,appi)
        call dvmod(pmu,3,apmu)

        path0pi=ctpi*appi/ampi
        path0mu=ctmu*apmu/ammu
```

```
        call dvunit(ppi,upi,3)
        call dvunit(pmu,umu,3)

        probpi=0.d0
        probmu=0.d0

c  First the pion

        call dvdot(upi,upi,2,ap)
        if (ap.eq.0.d0) then
           param=z0/upi(3)
           pathpi=z0
           goto 378
           endif
        call dvdot(upi,xpi,2,bp)
        call dvdot(xpi,xpi,2,cp)
        cp=cp-r0**2
        if ((bp*bp-ap*cp).lt.0.d0) then
           probpi=0.d0
           write(*,*)'sqrt<0 pi'
           goto 357
           endif
        param=(-bp+dsqrt(bp*bp-ap*cp))/ap

c     Pion on the walls
        if (param*upi(3).le.z0) then
           xfin=upi(1)*param+xpi(1)
           yfin=upi(2)*param+xpi(2)
           zfin=upi(3)*param
           endif

c     Pion on the end plate
        if (param*upi(3).gt.z0) then
           param=z0/upi(3)
           xfin=upi(1)*param+xpi(1)
           yfin=upi(2)*param+xpi(2)
           zfin=z0
           endif
```

```
c   and the path available for decay
       pathpi=dsqrt((xfin-xpi(1))**2+(yfin-xpi(2))**2+(zfin-xpi(3))**2)



c now the probability that the pion decays
378    probpi=1.d0-dexp(-pathpi/path0pi)


386    if (idptc.eq.1) goto 357




c Now the muon. I have to do a step integration
c arbitrarily chose 10cm steps

        nsteps=int(param/10.d0)+1
        dl=param/nsteps

c I calculate A which will remain through the loop
        call dvdot(umu,umu,2,a)

        do istep=1,nsteps
        pat=dl*(istep-0.5d0)

        xpin(1)=xpi(1)+upi(1)*pat
        xpin(2)=xpi(2)+upi(2)*pat
        xpin(3)=xpi(3)+upi(3)*pat

        if (a.eq.0.d0) then
           xmufin=xpin(1)
           ymufin=xpin(2)
           zmufin=z0
           goto 234
           endif
```

```
        call dvdot(xpin,umu,2,b)
        call dvdot(xpin,xpin,2,c)
        c=c-r0**2

        if  (B*B-A*C.lt.0.d0) then
           dprobmu=0.d0
           write(*,*)'sqrt<0 mu'
           goto 412
        end if
        tlambda=(-B+dsqrt(B*B-A*C))/A

c on the walls
        if ((tlambda*umu(3)+xpin(3)).le.z0) then
           xmufin=umu(1)*tlambda+xpin(1)
           ymufin=umu(2)*tlambda+xpin(2)
           zmufin=umu(3)*tlambda+xpin(3)
           endif

c on the end plate
        if ((tlambda*umu(3)+xpin(3)).gt.z0) then
           tlambda=z0/umu(3)
           xmufin=upi(1)*tlambda+xpin(1)
           ymufin=upi(2)*tlambda+xpin(2)
           zmufin=z0
           endif

234     pathmu=dsqrt((xmufin-xpin(1))**2+(ymufin-xpin(2))**2+
     + (zmufin-xpin(3))**2)



c The muon decay probability is now integrated

       dprobmu=(1.d0-dexp(-pathmu/path0mu))
     +          * dl/path0pi*(dexp(-pat/path0pi))
```

```
 412    probmu=probmu+dprobmu

        enddo
357     return
        end


c Simple subroutines for double precision array algebra

      subroutine ducopy(a,b,n)
      real*8 a(n),b(n)
      integer n,i
      do 10 i=1,n
         b(i)=a(i)
 10   enddo
      return
      end

      subroutine dcross(a,b,c)
      real*8 a(3),b(3),c(3)
      c(1)=a(2)*b(3)-a(3)*b(2)
      c(2)=-a(1)*b(3)+a(3)*b(1)
      c(3)=a(1)*b(2)-a(2)*b(1)
      return
      end

      subroutine dvunit(a,b,n)
      real*8 a(n),b(n),m,c
      integer i,n
      c=0.D0
      do 10 i=1,n
         c=c+a(i)**2
 10   enddo
      m=dsqrt(c)
      do 20 i=1,n
         b(i)=a(i)/m
 20   enddo
      return
```

```
      end

      subroutine dvdot(a,b,n,ris)
      real*8 a(n),b(n),dot,ris
      integer n,i
      dot=0.D0
      do 10 i=1,n
         dot=dot+a(i)*b(i)
 10   continue
      ris=dot
      return
      end

      subroutine dvmod(a,n,ris)
      real*8 a(n),b,ris
      integer n,i
      b=0.D0
      do 10 i=1,n
         b=b+a(i)**2
 10   enddo
      ris=dsqrt(b)
      return
      end
```

# Appendix B

# Oscillations program

```
c*********************************************************************
c                           NEUTRINO MIXING
c
c*********************************************************************
      parameter (nbine=100)
      complex*16 R(3,3),T(3,3),VR(3,3),W(3),MR(3,3)
      complex*16 HV(3,3),VRT(3,3),HA(3,3),M(3,3)
      complex*16 mass11,mass22,mass33
      real*8 t12,t13,t23,d,pi,E,L
      real*8 tg12,tg13,tg23,dg,Eposc
      real*8 Amat,dmass12,dmass23,p
      real*8 po(3,3)
      integer j,ie
      real*8 nmP,amP,ne,am,ae,nm
      real*8 onm,oam,one,oae,mne,mam,mae,mnm
      real*8 de,signal,noise,aie

c Energy bin dimension
      de=2.d0/nbine

c Greek Pi
      pi=acos(-1.d0)

c Parameters:
c Mixing angles in degrees
```

```
      tg12=31.71d0
      tg13=2.87d0
      tg23=45.d0

c CP violating phase in degrees
      dg=0.d0

c Detector scale fluxes ar calculated with a 1kton detector 10x10 m^2
c In this analysis it has been used 40kton detector 34^34 m^2(1156m^2)
      rescale=(34.d0)*(34.d0)/(100.d0)

c Neutrino energy
      E=.250d0

c Decay tunnel - Detector distance
      L=130.d0

c Neutrino masses SQUARED (eV)
c Mezzetto
      mass33=(0.00330,0.d0)
      mass22=(0.00010d0,0.d0)
      mass11=(0.00005d0,0.d0)

c     dm21^2=5 10^-5
c     dm31^2=3.25 10^-3
c     dm32^2=3.2  10^-3

c Matter effect
      Amat=0.d0
c-----------------------------------------------------------------------

c Mixing angles in radiants
      t12=(tg12/180.d0)*pi
      t13=(tg13/180.d0)*pi
      t23=(tg23/180.d0)*pi

c CP violating phase in radiants
      d=(dg/180.d0)*pi
```

```
c Fill rotation matrix
      call UROT(t12,t13,t23,d,R)

c Fill Mass matrix
      call MASSA(mass11,mass22,mass33,M)

      call HCONJ(R, T)
      call PRODOTTO(M,R,MR)
      call PRODOTTO(T,MR,HV)
      call SOMMA(HV,Amat,HA)

c Eigenvalues Eigenvectors
      call VALVET(HA,W,VRT)

      call HCONJ(VRT,VR)


      open(UNIT=1,FILE='flux40130100+.20',STATUS='OLD')
      open(UNIT=2,FILE='fluxosc100+.20',STATUS='UNKNOWN')
      do 100 i=1,2000
         read(1,*)aie,E,nmP, amP, ne,  am,  ae,  nm
         E=E-(de/2.01d0)
         call POSC(R,T,W,L,E,po)

         nmP=nmP*rescale*(130.d0**2)/L**2
         amP=amP*rescale*(130.d0**2)/L**2
         ne =ne *rescale*(130.d0**2)/L**2
         am =am *rescale*(130.d0**2)/L**2
         ae =ae *rescale*(130.d0**2)/L**2
         nm =nm *rescale*(130.d0**2)/L**2

         onm=(nmP+nm)*po(2,2)+ne*po(1,2)
         signal=(nmP+nm)*po(2,1)
         noise=ne*po(1,1)
         one=ne*po(1,1)+(nmP+nm)*po(2,1)
         onm=(nm+nmP)*po(2,3)
         oam=(amP+am)*po(2,2)+ae*po(1,2)
```

```
         oae=ae*po(1,1)+(amP+am)*po(2,1)
         write(2,*)aie,E,nmP,amP,ne,am,ae,nm,signal,noise
 100  continue
      close(UNIT=2)
      close(UNIT=1)
 1234 end


c--------------------------------------------------------------------
c SUBROUTINES

c Hermitian conjugation of  (3 x 3) complex matrix
       SUBROUTINE HCONJ(A, AHC)
       complex*16 A(3,3),AHC(3,3)
       n=3
        do 20 j = 1, n
         do 30 k = 1, n
          AHC(j,k) = dconjg(A(k,j))
 30       continue
 20      continue
         return
         end


c Fill mass matrix
       SUBROUTINE MASSA(mass11,mass22,mass33,M)
       complex*16 M(3,3),mass11,mass22,mass33
       M(1,1)= mass11
       M(2,2)= mass22
       M(3,3)= mass33
       M(1,2) = (0.d0,0.d0)
       M(1,3) = (0.d0,0.d0)
       M(2,1) = (0.d0,0.d0)
       M(2,3) = (0.d0,0.d0)
       M(3,1) = (0.d0,0.d0)
       M(3,2) = (0.d0,0.d0)
       return
       end
```

```
c Oscillation probability
       SUBROUTINE POSC(VR,VRT,W,L,E,po)
       complex*16 VR(3,3),VRT(3,3),W(3),poc(3,3)
       real*8 E,L,po(3,3),wr(3)
       complex*16 E1,L1
       integer n,alpha,beta
       n = 3
       do 22 beta = 1, n
          do 33 alpha = 1, n
             po(alpha,beta)=0.d0
             poc(alpha,beta)=0.d0
             do 64 i = 1, n
                do 73 j = 1, n

        poc(alpha,beta)=VR(alpha,i)*VRT(i,beta)*VR(beta,j)*
     +     VRT(j,alpha)*exp(-(0.d0,1.d0)*2.d0*(W(i)-W(j))*1.27d0*L/E)
     +     +poc(alpha,beta)

 73             continue
 64          continue
             po(alpha,beta) = DREAL(poc(alpha,beta))
 33       continue
 22    continue
 1000 return
      end



c Product of complex matrixes
      SUBROUTINE PRODOTTO(A,B,P)
      complex*16 A(3,3),B(3,3),P(3,3)
      n = 3
      P(1,1) = 0.d0
      P(1,2) = 0.d0
      P(1,3) = 0.d0
      P(2,1) = 0.d0
```

```
      P(2,2) = 0.d0
      P(2,3) = 0.d0
      P(3,1) = 0.d0
      P(3,2) = 0.d0
      P(3,3) = 0.d0
      do 100 k = 1, n
         do 102 i = 1, n
            do 103 j = 1, n
               P(i,k) = DREAL(A(i,j))*DREAL(B(j,k))
     +              -  DIMAG(A(i,j))*DIMAG(B(j,k))
     +              + (0.d0,1.d0)*(DREAL(A(i,j))*DIMAG(B(j,k))
     +              + DIMAG(A(i,j))*DREAL(B(j,k))) + P(i,k)
 103        continue
 102     continue
 100  continue
      return
      end

      SUBROUTINE  SOMMA(d,Amat,S)
      complex*16 A(3,3),d(3,3),S(3,3)
      real*8 Amat
       A(1,1) = Amat*(1.d0,0.d0)
       A(1,2) = (0.d0,0.d0)
       A(1,3) = (0.d0,0.d0)
       A(2,1) = (0.d0,0.d0)
       A(2,2) = (0.d0,0.d0)
       A(2,3) = (0.d0,0.d0)
       A(3,1) = (0.d0,0.d0)
       A(3,2) = (0.d0,0.d0)
       A(3,3) = (0.d0,0.d0)
       n = 3
       do 20 k = 1, n
          do 30 j = 1, n
             S(k,j) = (1.d0,0.d0)*(DREAL(d(k,j)) + DREAL(A(k,j)))
     +       +(0.d0,1.d0)*DIMAG(D(k,j)) + DIMAG(A(k,j))
 30       continue
 20    continue
       return
```

```
       end


c Fill rotation complex matrix
      SUBROUTINE UROT(t12,t13,t23,d,R)
      real*8 t12,t13,t23,d
      real*8 theta12, theta13, theta23, delta
      real*8 ur(3,3),ui(3,3)
      complex*16 R(3,3)
      n = 3
      ur(1,1) = cos(t12)*cos(t13)
      ui(1,1) = 0.d0
      ur(1,2) = sin(t12)*cos(t13)
      ui(1,2) = 0.d0
      ur(1,3) = sin(t13)*cos(d)
      ui(1,3) = -sin(t13)*sin(d)
      ur(2,1) = -sin(t12)*cos(t23)-(cos(t12)*sin(t23)*sin(t13))*cos(d)
      ui(2,1) = -(cos(t12)*sin(t23)*sin(t13))*sin(d)
      ur(2,2) = cos(t12)*cos(t23)-(sin(t12)*sin(t23)*sin(t13))*cos(d)
      ui(2,2) = -(sin(t12)*sin(t23)*sin(t13))*sin(d)
      ur(2,3) = sin(t23)*cos(t13)
      ui(2,3) = 0.d0
      ur(3,1) = sin(t12)*sin(t23)-(cos(t12)*cos(t23)*sin(t13))*cos(d)
      ui(3,1) = -(cos(t12)*cos(t23)*sin(t13))*sin(d)
      ur(3,2) = -sin(t23)*cos(t12)-(sin(t12)*cos(t23)*sin(t13))*cos(d)
      ui(3,2) = -(sin(t12)*cos(t23)*sin(t13))*sin(d)
      ur(3,3) = cos(t23)*cos(t13)
      ui(3,3) = 0.d0

      do 3 l = 1, n
         do 4 m = 1, n
            R(l,m) = ur(l,m)+(0.d0,1.d0)*ui(l,m)
 4       continue
 3    continue

      return
      end
```

```
c W eigenvalues from the smallest to the biggest
c VR correspondig eigenvectors
      SUBROUTINE VALVET(HA,W,VR)
      complex*16 A(3,3), HA(3,3)
      complex*16 VL(3,3),VR(3,3),WORK(12),W(3),MR(3,3)
      complex*16 VRO(3,3),WO(3)
      real*8 RWORK(9),E,L,Wabs(3)
      real*8 costb, costa,y
      integer index(3), n
      character*1 JOBVL, JOBVR
      n = 3
      JOBVL = 'N'
      JOBVR = 'V'

      call ZGEEV(JOBVL,JOBVR,3,HA,3,W,VL,3,VR,3,WORK,12,RWORK,INFO)

 1000 return
      end
```

# Bibliography


[1] W. Pauli, Open letter to Radioactive Ladies and Gentlemen (1930); (translation into english) Physics Today **31**, 27 (1978).

[2] J. Chadwick, Nature **129**, 312 (1932).
Proc. Roy. Soc. **A 136**, 692 (1932).

[3] E. Fermi Z. Phys. **88**, 161 (1934).

[4] F. Reines and C. Cowan, Phys. Rev. **92**, 830 (1953).

[5] R.P. Feynman, M. Gell Mann, Phys. Rev. **109**, 1 (1958).

[6] M. Goldhaber, L. Grodzins, A. W. Sunyar, Phys. Rev. **109**, 1015 (1958).

[7] R. Davis, D.S. Harmer, Bull. Am. Phys. Soc. **4**, 217 (1959).

[8] B. Pontecorvo, JETP **10**, 1236 (1960).

[9] G. Dandy, J.M. Gaillard, K. Goulianos, L.M. Lederman, N. Mistry, M. Schwartz, H. Steinberger, Phys. Rev. Lett. **9**, 1 (1962).

[10] The ALEPH, DELPHI, L3, OPAL Collaborations, D. Decamo *et al.* Phys. Lett. **B276**, 247 (1991).

[11] DONUT Collaboration, Nucl. Phys. Proc. Suppl. **9**, (1999).

[12] Y.Fukuda *et al.*, Phys. Rev. Lett. **81**, 1562 (1998).

[13] Di Lella, CERN Academic Training Lectures 342 (1996).

[14] J.N. Bahcall Rev. Mod Phys. **50**, 881 (1978).
J.N. Bahcall and M. Pinsonneault, Phys. Rev. **D58**, 6016 (1998).

[15] R. Davis, Prog. Part. Nucl. Phys. **32**, 13 (1994).

[16] K. Lande, in Talk at Neutrino 98 Takayama, ed. (1998).

[17] GALLEX Coll., Phys. Lett. **B357** 237 (1995).

[18] J.N. Abdurashitov, Phys. Rev. Lett.**83** 23 (1999)

[19] W. Hampel *et al.*, Phys. Rev. Lett. **B447**, 127 (1999).

[20] R. Bernabei, Nucl. Phys. B - Proceedings Supplements **66**, 342-345 (1998).

[21] Experiment description available at:
http://www-sk.icrr.u-tokyo.ac.jp/doc/sk/

[22] J.N. Bahcall, M. Pinsonneault, S. Basu and J. Christensen-Dalsgaard, Phys. Rev. Lett. **78**, 171 (1997).

[23] L. Wolfenstein, Phys. Rev. **D17**, 2369 (1978).

[24] S.P. Mikheyev and A. Yu. Smirnov, Sov. J. Phys. **42**, 6 (1985).

[25] Science and Technology of BOREXINO: a real-time Detector for Low Energy Solar Neutrinos. hep-ex/0012030. Submitted to Astroparticle Physics (2000).

[26] E.D. Earle, W.F. Davidson and G.T. Ewan, Physics in Canada **44**, 49 (1988).

[27] A. Suzuki, in Proc VIII Int. Workshop on neutrino Telescopes, ed. Milla Baldo Ceolin, edizioni papergraph, Venezia, (1999).

[28] K.S. Hirata, Phys. Rev. Lett. **B205**, 416 (1988).

[29] D. Casper *et al.*, Phys. Rev. Lett. **66**, 2561 (1991).

[30] C. Berger *et al.*, Phys. Rev. Lett. **B227**, 489 (1989).

[31] M. Aglietta *et al.*, Eur. Lett. **8**, 611 (1989).

[32] W.W.M. Allison *et al.*, Phys. Rev. Lett. **B391**, 491 (1997).

[33] Y. Fukuda *et al.*, Phys. Rev. Lett. **B335**, 237 (1995).

[34] K. Scholberg *et al.*, in Proc VIII Int. Workshop on neutrino Telescopes, ed. Milla Baldo Ceolin, edizioni papergraph, Venezia, (1999).

[35] M. Messier, Doctoral Thesis, Evidence for Neutrino Mass from Observations of Atmospheric Neutrinos with Super Kamiokande, Boston University graduate school of arts and sciences (1999).

[36] M. Spinetti, in Proc VIII Int. Workshop on neutrino Telescopes, ed. Milla Baldo Ceolin, edizioni papergraph, Venezia, (1999).

[37] T. Toshito, at ElectroWeak Interactions and Unified Theories, Moriond, (2001).

[38] K.K. Gan, hep-ex 0103010, (2001).

[39] M. Apollonio *et al.*, Phys. Rev. Lett. **B240**, 397 (1998).

[40] F. Boehm, Reactor Neutrino Physics: An Update, in Proc VIII Int. Workshop on neutrino Telescopes, ed. Milla Baldo Ceolin, edizioni papergraph, Venezia, (1999).

[41] H.V. Klapdor-Kleingrothaus and A. Staudt, Non-accelerator particle physics, Bristol IOP, (1995).

[42] C. Athanassopoulos *et al.*, Nucl. Instrum. Meth. Phys. Res. **A388**, (1997).

[43] B. Zeitnitz, Prog. Part. Nucl. Phys. **32**, 351 (1994).

[44] E. Church *et al.*, A proposal for an experiment to measure $\nu_\mu \rightarrow \nu_e$ oscillations and $\nu_\mu$ disappearance at the Fermilab Booster: BooNE unpublished (1997).

[45] E. Eskut *et al.*, Nucl. Instr. Meth. Phys. Res. **A401**, (1997).

[46] C. Albright and R. Shock, Phys. Rev. Lett. **B84**, 123 (1979).

[47] Experiment description available at:
http://neutrino.kek.jp/

[48] Experiment description available at:
http://www.hep.anl.gov/ndk/hypertext/numi.html

[49] M. Buhler-Broglin *et al.*, General Description of the CERN project for a neutrino beam to Gran Sasso (CNGS), Ed. K. Elsener (2000).

[50] ICARUS Coll., Nucl. Instr. and Meth. **A455**, 378 (2000).

[51] A. Cervera *et al.*, Nucl. Phys. **B579** (2000).

[52] E, Fernandez, Santa Cruz de la Palma - a candidate detector site with 2810 km baseline, at Neutrino Factory Oscillation Working Group (20.02.2001).

[53] E. Lillestol, Svalbard - a 3000 km candidate detector site, at Neutrino Factory Oscillation Working Group (05.12.2000).

[54] N.V. Mokhov, "The MARS Code System User's Guide", Fermilab-FN-628 (1995)
N.V. Mokhov, "MARS Code Development, Benchmarking and Applications" Fermilab-Conf-00-066(2000)
O.E. Krivosheev and N.V. Mokhov, "A New MARS and its Applications", Fermilab-Conf-98/43 (1998)
N.V. Mokhov, S.I. Striganov, A. Van Ginneken, S.G. Mashnik, A.J. Sierk and J. Ranft, "MARS Code Developments", Fermilab-Conf-98/379 (1998)

[55] B. Autin *et al.*, Conceptual design of the SPL, a high-power superconductiong $H^-$ linac at CERN, Ed. M. Vretenar (2000).

[56] A.E. Ball *et al.*, NuFact Note 42 (2000). Available at: http://molat.home.cern.ch/molat/neutrino/nfnotes.html

[57] D.E. Groom et al, Eur. Phys. J. **C15**, (2000).

[58] R. Hagedorn, Relativistic kinematics, W.A. Benjamin Inc., (1963).

[59] T.K. Gaisser, Cosmic Rays and Particle Physics, Cambridge University Press, (1990).

[60] F. Combley, E. Picasso, Phys.Rept. **14**, (1974).

[61] E.B. Koffman, F.L. Friedman, FORTRAN, Reading, Mass. Addison-Wesley, (1997).

[62] E.G. Anassontzis et al. Nucl. Inst. Meth. **A349** 242 (1994).

[63] C. Racca,III International Workshop On New Worlds In Astroparticle Physics, Faro, Portugal (2000).

[64] C.H. Llewellyn Smith, Phys.Rept **261**, 261 (1972).

[65] G.F. Knoll, Radiation detection and measurement, New York Wiley, (2000).

[66] LSND Collaboration, Phys. Rev. Lett. **81**, 1774 (1998).

[67] HARP coll., Status report of the HARP experiment, (2000)
Available at: http://harp.web.cern.ch/harp/

[68] P.R. Bevington, D.K. Robinson, Data reduction and error analysis for the physical sciences, Boston, MA McGraw-Hill, (1992).
W.T. Eadie, Statistical methods in experimental physics, North Holland, (1971).